Tectonic evolution of the Betic-Rif orogen constrained by 3-D microstructural analysis and Sm-Nd dating of garnet porphyroblasts

Domingo Aerden[1,1], Thomas P Farrell[2], Ethan Baxter[3], Emily Stewart[4], and Mohamed L. Bouybaouene[5]

[1]Universidad de Granada, Spain
[2]Boise State University,
[3]Boston College
[4]Yale University
[5]Département de Géologie, Université de Rabat

November 30, 2022

Abstract

Microstructural analysis of porphyroblast inclusion trails in 44 micaschist samples has been combined with Sm-Nd garnet geochronology to investigate the tectonic history of the Betic-Rif orogen. Three sets of garnet porphyroblasts have been distinguished bsed on the specific orientations of their FIAs (micro-fold axes). Similar ages and trend distributions of FIAs in the Nevado-Filabride and Alpujarride-Sebtide complexes indicate a shared tectono-metamorphic evolution. The earliest FIA set (WNW-ESE trend) formed in the late Eocene according to a new 35Ma age for garnets in the Lower Nevado-Filabrides. This set is inferred to record perpendicular (NNE-SSW) crustal shortening due to Africa-Iberia convergence. A N-dipping subduction zones at this time is suggested by the dominant curvature sense of inclusion trails defining this FIA set. A subsequent FIA set with average NE-SW trend has been dated in the Oligocene (27 - 22Ma) in five samples of the Alpujarride-Sebtide Complex. It can be related to a NW-directed 'Appenninic' subduction of Africa-Adria below Iberia. The youngest FIAs in the Alpujarride-Sebtide Complex trends NNW-SSE and may be linked to westward drift of the Alboran Domain and development of the Gibraltar Arc in the early to middle Miocene. Four early to middle-Miocene garnet ages (21-13Ma) in the upper Nevado-Filabride Complex are consistent with heating from above during exhumation of this complex or reburial of the complex below an extending Alpujarride-Sebtide Complex. This was accompanied by the development two FIA sets whose suborthogonal NNW-SSE and WSW-ENE trends may reflect simultaneous NW drift of Africa and WSW motion of the Alboran Domain.

Refined tectonic evolution of the Betic-Rif orogen through integrated 3-D microstructural analysis and Sm-Nd dating of garnet porphyroblasts

Domingo G.A.M. Aerden[1,2], Thomas P. Farrell[3*], Ethan F. Baxter[3,4], Emily M. Stewart[4†], Alejandro Ruiz Fuentes[1] and Mohamed Bouybaouene[5]

[1]Depto. de Geodinámica, Universidad de Granada, Spain

[2]Instituto Andaluz de Ciencias de la Tierra (CSIC-UGR), Granada, Spain

[3]Boston College, Dept. Earth & Environm. Sci, Chestnut Hill, MA 02167 USA

[4]Boston University, Dept. Earth & Environm, 675 Commonwealth Ave, Boston, MA 02215 USA

[5]Département de Géologie, Université de Rabat, Rabat, Morocco.

Corresponding author: Domingo Aerden (aerden@ugr.es)

* Current address: Geoscience Dept, Boise State University

† Current address: Dept Earth, Ocean, & Atmospheric Sci, Florida State University, 1011 Academic Way, Tallahassee, FL 32306.

Key Points:

Micro-fold axes preserved within porphyroblasts of the Betic-Rif orogen record changes in plate motion

Sm-Nd dating of garnet porphyroblasts indicates Eocene tectonism in the Nevado-Filabride complex

Combining FIA and garnet geochronology shown powerful tool for plate motion reconstruction

Abstract

Microstructural analysis of porphyroblast inclusion trails in 44 micaschist samples has been combined with Sm-Nd garnet geochronology to investigate the tectonic history of the Betic-Rif orogen. Three sets of garnet porphyroblasts have been distinguished bsed on the specific orientations of their FIAs (micro-fold axes). Similar ages and trend distributions of FIAs in the Nevado-Filabride and Alpujarride-Sebtide complexes indicate a shared tectono-metamorphic evolution. The earliest FIA set (WNW-ESE trend) formed in the late Eocene according to a new 35Ma age for garnets in the Lower Nevado-Filabrides. This set is inferred to record perpendicular (NNE-SSW) crustal shortening due to Africa-Iberia convergence. A N-dipping subduction zones at this time is suggested by the dominant curvature sense of inclusion trails defining this FIA set. A subsequent FIA set with average NE-SW trend has been dated in the Oligocene (27 - 22Ma) in five samples of the Alpujarride-Sebtide Complex. It can be related to a NW-directed 'Appenninic' subduction of Africa-Adria below Iberia. The youngest FIAs in the Alpujarride-Sebtide Complex trends NNW-SSE and may be linked to westward drift of the Alboran Domain and development of the Gibraltar Arc in the early to middle Miocene. Four early to middle-Miocene garnet ages (21-13Ma) in the upper Nevado-Filabride Complex are consistent with heating from above during exhumation of this complex or reburial of the complex below an extending Alpujarride-Sebtide Complex. This was accompanied by the development two FIA sets whose suborthogonal NNW-SSE and WSW-ENE trends may reflect simultaneous NW drift of Africa and WSW motion of the Alboran Domain.

Plain Language Summary

3D microstructural analysis of tectonic foliations preserved within garnet porphyroblasts has been combined with radiometric dating of these crystals to reconstruct a complex tectonic evolution of the Betic-Rif orogen, one of the mostly strongly curved mountain belts on Earth (Gibraltar Arc). Different ages groups of garnets have been discovered preserving differently oriented microfolds in their interior. The timing and orientation of these microfolds can be

linked to several changes in the movement direction of Africa relative to Iberia from Eocene to Middle-Miocene times. Our data place new constraints on paleogeographic reconstructions of south-western Europe and illustrate a powerful new methods tool reconstructing past plate motions.

1. Introduction

The metamorphic core of the Betic-Rif orogen is characterized by multiple generations of tectonic fabrics, folds and ductile to brittle shear zones witnessing a complex tectonic evolution. The precise geometry and temporal relationships of these structures is uncertain and insufficiently constrain a range of proposed geodynamic models that differ on such fundamental points as the number, polarity and age of subduction zones or the role of crustal extension versus compression (e.g. Michard, 2002; Vergés & Fernandez, 2012; Vissers, 2012; Platt et al., 2013; Jabaloy-Sanchez et al., 2019). This paper contributes to resolving these questions by examining the kinematic and geochronological record provided by metamorphic porphyroblasts and their internal tectonic fabrics (inclusion trails). Forty-four oriented samples of porphyroblastic schists from the two metamorphic nappe complexes within the orogen (Nevado-Filabride and Alpujarride-Sebtide complex) have been studied in precisely oriented thin sections and X-ray computed microtomographies (XCT). This has been combined with Sm-Nd (TIMS) dating of garnet porphyroblasts in 10 selected samples as a well-established accurate and precise method to constrain the timing of tectonometamorphic processes (e.g. Baxter et al. 2017).

The kinematic significance of different types of porphyroblast inclusion-trails has been intensely debated particularly between 1990 and 2010 (e.g. Bell et al., 1992; Passchier et al., 1992; Fay et al., 2008, 2009; Bons et al., 2009). Since these microstructures play a central role in our study, it is appropriate to briefly outline how ideas about them have evolved. More than 100 years ago, Peach et al. already (1912) described spiral garnets from the Calledonides and perceived what seemed an obvious explanation when they wrote: "*The garnet was rotating under the impulses received from streams of material flowing with unequal velocities past its two sides. It was being rolled along, and was growing larger, like a snowball, during the process*". During much of the 20th century, the snowball model remained unquestioned and was further refined (Zwart, 1960; Spry, 1963; Rosenfeld, 1968 amongst others). The model predicts (i) that the curvature sense of inclusion-trails (from the porphyroblast center to the rim) is opposite to the shear sense, (ii) that the curvature axes lies normal to the shearing direction, and (c) that the amount of curvature is related to the amount of shear strain. McLachlan (1953) may have been the first to apply these principles to a regional tectonic problem. It was debated at the time whether a strong lineation in the Moine schists (Scottish Calledonides) oriented parallel to fold axes formed parallel or perpendicular to the direction of regional tectonic transport. By cutting thin sections parallel and perpendicular to the lineation in three samples containing spiral garnets, he determined that the spiral axes were subparallel to the lineation and from this he concluded tectonic transport (i.e. thrusting) normal to the lineation and fold axes. Significantly, a similar conclusion will be reached in this paper based on the general relationships between FIAs, fold axes and stretching lineations in the Betic-Rif orogen.

During the 1980s a radical reinterpretation of 'rotational' inclusion trails was proposed (Bell, 1985; Bell et al., 1986; Bell & Johnson, 1989; Bell & Hayward, 1991) emphasizing the control of deformation partitioning on foliation development and porphyroblast growth. Porphyroblasts were argued to preferentially nucleate within microlithon domains during early stages of crenulation cleavage development. Depending on the relative rates of porphyroblast growth and deformation, straight to sigmoidal inclusion trails would then develop by overgrowth of actively forming crenulations without porphyroblast rotation. More controversial was the claim that spiral-shaped inclusion-trails form by repetitions of this process during the development of several suborthogonal foliations created by alternating phases of crustal shortening and gravitational collapse. This model implied a powerful indicator of orogenetic movements (Bell et al., 1995) that was tested further via the collection of inclusion-trail orientation data in different mountain belts. This research abandoned the traditional use of thin sections cut normal to the foliation and parallel to the lineation in each sample, and changed it for new 3D methods based on multiple thin sections of samples cut with fixed orientations in a common (geographic) reference frame. Consistent orientations of inclusion trails revealed by this work in individual folds, shear zones (Steinhardt, 1989; Bell & Forde, 1995; Hickey & Bell, 1999; Jung et al., 1999; Timms, 2003; Aerden et al., 2010; Evins, 2005) and across large metamorphic regions (Aerden, 1994, 1998, 2004; Bell et al., 1998; Bell & Mares, 1999; Sayab, 2005; Rich, 2006; Yeh & Bell, 2004; Yeh, 2007; Kim & Ree, 2013; Ali, 2010; Shah et al., 2011; Sanislav, 2011; Skrzypek, 2011; Aerden et al., 2013; Ali et al., 2016; Sayab et al., 2016) provided compelling evidence for the 'non-rotational' interpretation. Several studies reported vertical and horizontal preferred orientations of inclusion trails directly witnessing shortening-collapse cycles in the northern Appalachians (Hayward, 1992), the Lachlan fold belt (Johnson, 1992), the Mount Isa inlier (Sayab, 2006), the Himalayas (Shah et al., 2011, Bell & Sapkota, 2012), the European Variscan belt (Aerden 1994, 1995, 1998, 2004) and the Betic Cordillera (Aerden & Sayab, 2008, Aerden et al., 2013; Ruiz-Fuentes, 2020). Considerable progress has also been made in recent years towards a better understanding of the micro-physical processes responsible for reducing or preventing porphyroblast rotation with new and more realistic modeling approaches (e.g. ten Grotenhuis et al., 2002; Fay et al. 2008; Griera et al., 2011; Gardner & Wheeler, 2021).

Microstructural data presented herein will be shown to further support limited porphyroblast rotation and to allow detailed reconstruction of the sequence of fabrics that developed in the studied metamorphic unit, the original orientations of these fabrics and their kinematics. The association of these fabrics with different porphyroblastic minerals that grew at different times along the P-T paths of tectonic units and new Sm-Nd garnet ages place important constraints on different periods of tectonism with different kinematics. Our research builds further on and refines that of Aerden (2013) and Aerden & Ruiz Fuentes (2020) in the Nevado-Filabride Complex by making extensive use of X-ray computed micro-tomography (XCT) to study the 3D microstructure of individual samples and porphyroblasts, and by including a large number of samples from the Alpujarride-Sebtide complex. In these two papers, four age groups of inclusion trails were distinguished, whose specific directions were tentatively correlated with those of Africa-Iberia relative plate motions during the Tertiary. This intriguing link is further explored and strengthened in this paper.

The gap in scale between microstructural data and regional tectonics is bridged by an analysis of mesoscale structures observed in selected outcrops and a comprehensive compilation of more than 15000 field data, which reveals the regional pattern defined by different generations of lineations and fold axes. This pattern is interpreted to witness a superposition of different folding directions that can be correlated with different FIA sets and constrained in time by Sm-Nd garnet ages for 4 Nevado-Filabride samples and 5 Alpujarride-Sebtide samples. The distribution of differently oriented fold and lineation sets is shown to be particularly relevant to the nature and kinematics of the Gibraltar Arc, one of the smallest and tightest oroclines on Earth surrounding the thinned continental crust of the Alboran Sea (Fig. 1).

2. Geological setting

2.1. The Betic-Rif orogen

The Betic-Rif orogen is a tightly curved mountain belt (Gibraltar Arc) situated at the westernmost end of the Alpine-Himalayan orogenic system. It features an external fold and thrust belt (External Zones) of Miocene age developed at the expense of Mesozoic and Cenozoic sediments of the Iberian and North-African forelands. The metamorphic hinterland or Internal Zone, also known as the Alboran Domain, records earlier Paleogene tectonism and includes several large subcontinental peridotite massifs. In the early to middle-Miocene, the orogen experienced a dramatic extensional collapse associated with the opening of the western Mediterranean basins and development of the Gibraltar and Calabrian Arcs. The synchronicity of this extension with contraction in the external thrust belt is attributed to some combination of back-arc spreading driven by roll-back of a northwest dipping subducting slab, (e.g. Royden, 1993; Lonergan & White, 1997, Jolivet & Faccenna, 2000), and gravitational spreading of a collisional orogen following the detachment and sinking of part of its mantle lithosphere (Platt & Vissers, 1989; Platt et al., 2013; Williams & Platt, 2018).

Prior to the Miocene extension event, the Iberian plate included the Baleares-Sardinia-Corsica block and another crustal segment located further south known as 'Alkapeca' (Bouillin, 1986; Lonergan & White, 1997; Carminati et al., 1998; Faccenna, 2001) from which the Alboran Domain and correlative metamorphic units in the Kabylias (North Algeria), Pelatorian Mountains (Sicily) and Calabria are thought to be derived. Late Cretaceous/Early Paleogene paleogeographic maps either show Alkapeca as an independent crustal fragment (the 'Mesomediterranean terrain' of Guerrera et al., 1993) separated from Iberia by a branch of the

Alpine Tethys (e.g. Handy et al. 2010; Michard et al., 2006; Leprêtre et al. 2018; van Hinsbergen et al., 2014), or forming an integral part of the Iberian plate (e.g. Jolivet & Faccenna, 2000; Stampfli & Hochard, 2009). This question depends on whether mafic and ultramafic lenses present in the upper levels of the Nevado-Filabride Complex represent a dismembered ophiolitic sequence (Puga et al., 2017 and references cited therein) or mafic intrusions in thinned continental crust (Gomez Pugnaire et al., 2019). The principle geodynamic models currently debated are: (a) Paleogene SE dipping subduction of the Iberian plate below Alkapeca followed by NW subduction of Africa-Adria below the opposite side of Alkapeca in the Oligocene (Michard et al., 2006; Handy et al., 2010; Leprêtre et al., 2018). (b) NW directed subduction in the Late Cretaceous and Paleogene, followed by Early Miocene opposite subduction of the Iberian margin below the Alboran Domain. (c) Simultaneous SE subduction of Iberia and NW subduction of Africa-Adria below Alkapeca separated by a transform fault (Verges & Fernandez, 2012). Note that these models only consider changes in subduction polarity, not in the direction of subduction as reconstructed in this paper.

Three main nappe complexes are traditionally distinguished in the Internal Zones known from bottom to top as the Nevado-Filabride complex, the Alpujarride Complex, which is called Sebtide Complex in the Rif, and the Malaguide Complex, which is called Ghomaride Complex in the Rif (Fig. 1). The two lower complexes record high to low-grade metamorphism whereas the upper complex is largely non-metamorphic. The three complexes have similar lithostratigraphic columns including a Variscan basement composed of Pre-Permian schists and quartzites, overlain by Permo-Triassic detrital sediments and Mesozoic carbonates, in the Malaguide-Ghomaride still followed by Paleogene carbonates and Oligocene to Early Miocene synorogenic clastics (e.g. Chalouan & Michard, 1990; Mazzoli and Martín-Algarra, 2011). The three complexes are thrusted over the 'Dorsale Calcaire' unit, a stack of steeply dipping to overturned thrust slices of Mesozoic carbonates cropping out mainly in the Western Betics and Rif (Mazzoli & Algarra, 2011; Vitale et al., 2014; Fig. 1, 2a, b). It is also counted to the Internal Zones (Alboran Domain) as it tectonically overlies the so called 'Flysch units': Upper-Cretaceous to Miocene deep to shallow marine sediments of the Alpine Tethys thrusted, in turn. over the External Zones. The Alpujarride - Nevado-Filabride contact is a brittle-ductile detachment delineated by brown-yellow carbonate breccias and mylonites traceable over more than 150 km distance in E-W direction. The contact locally places blueschist facies (carpholite-chloritoid-kyanite) Permo-Triassic phylites and Middle-Triassic dolomitic marbles over amphibolite facies micaschists and Mesozoic marbles of the Nevado-Filabride complex, thus combining a stratigraphic repetition with a metamorphic gap. This has been explained in terms of an extensional detachment cutting earlier thrusts (e.g. Martínez-Martínez, 2002), or extensional reactivation of a thrust (e.g. Vissers et al., 1995; Aerden & Sayab, 2008). Although shear-sense indicators associated with the contact vary considerably in detail, a major westward component is generally assumed. The Alpujarride-Sebtide/Malaguide-Ghomaride contact also produces a stratigraphic repetition with a metamorphic gap has a top- SE movement (Lonergan & Platt, 1995).

2.2. Nevado-Filabride complex

The Nevado-Filabride Complex is traditionally subdivided into a lower Veleta Nappe and an upper Mulhacen Nappe or sub-complex depending on further proposed tectonic subdivisions. The first mentioned complex mainly comprises a several km thick package of intensely deformed Devono-Carboniferous dark schists and quartzites. The second includes a larger portion of Permo-Triassic metapelites and quartzites (Tahal formation) overlain by Mesozoic marbles, and has been subdivided in two or three thrust slices. These are, from bottom to top, the Caldera Unit, Ophiolitic Unit and Sabinas Unit of Puga et al., (2002), or the Calar-Alto and Bedar-Macael units of García Dueñas et al. (1988). However, the boundaries between these units have proven difficult to identify in the field and this has giving rise to conflicting map interpretations to the extent that some authors have questioned the existence of internal tectonic contacts (Sanz-de-Galdeano & Santamaría-López, 2019). Confronted with this uncertainty, Aerden & Sayab (2008), Aerden et al. (2013) and Ruiz-Fuentes & Aerden (2018) focused on the sequence of deformation fabrics and associated folding phases within the complex. Their cross-sections show the Nevado-Filabride / Alpujarride contact sharply cutting across large upright folds (F_3) in the footwall that deform the main (S_2) foliation. These folds show the effects of a superposed vertical shortening in a several hundred meters wide zone located immediate below the Alpujarride contact characterized by a subhorizontal crenulation cleavage (S_4) and shear bands.

Ar-Ar dating of micas and amphiboles in the Nevado-Filabride Complex (Monié et al., 1991; Augier et al., 2005) initially supported an Early Cretaceous to Paleogene age of high pressure/low temperature (HP/LT) metamorphism similar as in the Alpujarride Complex (Platt et al., 2005; Lonergan & Platt, 1995). However, this interpretation was revised based on later U-Pb zircon ages of 15Ma (Sanchez-Vizcaino et al., 2001), Lu-Hf garnet ages of 13-18Ma (Platt et al., 2006) and Rb-Sr multimineral ages of 13-20Ma (Kirchner et al., 2016), which suggested that earlier Ar-Ar ages were significantly affected by excess Argon and geologically meaningless. Consequently, the tectono-metamorphic evolution of the Nevado-Filabrides was reinterpreted to be related to SE dipping subduction of the Iberian margin in the Miocene below an already partially exhumed and actively extending Alboran Domain (Platt et al., 2006; Behr & Plat, 2012).

Li & Massonne (2018), however, revived the possibility of a pre-Miocene metamorphic event based on U-Pb (EMPA) mean ages of 40Ma and 24Ma for two texturally distinct groups of monazite grains identified in two micaschist samples. The older population was linked to peak metamorphic conditions of about 17 kbar / 530°C, and would have been followed by followed by isothermal decompression and then reburial of the complex to 9 kbar / 650°. A similar polycyclic metamorphism was deduced by Puga et al. (2002) from mafic and ultramafic rocks of their Ophiolitic Unit and has been linked to dispersed Early Cretaceous to Miocene SHRIMP U-Pb zircon ages obtained in these rocks Puga et al. (2017). Santamaría-López et al. (2019) recently dated allanite grains (LA-ICPMS) that grew around 13Ma synchronous with garnet porphyroblast rims in two samples of the Mulhacen subcomplex. However, these garnet rims were shown to have formed at relatively low pressures of about 6 kbar, whereas undated garnet cores record pressures up to 22 kbar.

2.3. Alpujarride-Sebtide complex

A large number of thrust nappes were originally distinguished in the Alpujarride-Sebtide Complex where higher-grade rocks were observed to overly lower-grade ones, or Paleozoic rocks above their Permo-Triassic and Mesozoic cover. Following the recognition of crustal extension in the Alboran Domain, many of these thrusts were reinterpreted as inverted fold limbs, low-angle normal faults or thrusts. In the Western Betics and Rif, a twofold subdivision of the Alpujarride-Sebtide Complex into an upper Los Reales nappe and lower Blanca Unit (e.g. Mazzoli & Algarra, 2011) is widely accepted. The first includes a several km thick basal slab of subcontinental mantle rocks (Fig. 1) overlain by a strongly condensed crustal sequence of granulitic gneisses (15kbar/800°C), Paleozoic high to medium-grade schists, and lower-grade Permo-Triassic phylites. The lower-grade rocks preserve subduction-zone related high-pressure / low-temperature assemblages (Ctd-Ky-Car) of probable Eocene-Oligocene age (Platt et al., 2005; Esteban et al, 2011; Homonnay et al., 2018; Marrone et al., 2021), whereas the higher grade schists display a plurifacial metamorphism that evolved from low- to high-gradient conditions as recorded by relic Ctd-Grt-Ky, followed by Grt-St, followed by And, Sil, Plg, Bi. The high temperature / low-pressure event is well dated as Early Miocene (22-18Ma) and coincides broadly with the onset of crustal extension in the Alboran Domain (see Platt et al., (2014) for a comprehensive review of P-T-t paths proposed for the Alpujarride Complex). The Blanca-type units, including the Ojén, Yunqueras and Guadaiza sub-units of Tubía et al., (1994), record a similar metamorphic evolution as the Los Reales nappe, but near the contact with the overlying peridotites show extensive migmatization generally attributed to tectonic emplacement of hot peridotites along an Early-Miocene thrust (e.g. Tubía et al., 2013; Homonnay et al., 2018) or extensional detachment (e.g. Johanesen et al., 2014).

Correlation of the above mentioned Alpujarride units from the Western to Central and Eastern Betics is complicated by an intermediate large patch of Malaguide outcrop (Fig. 1), as well as late folding and faulting. Medium to high-grade rocks in the Central and Eastern Betics have been traditionally regarded a equivalent to the Los Reales Nappe and to tectonically overly lower-grade phylites and carbonates. However, Williams & Platt et al. (2018) recently interpreted all Alpujarride rocks exposed in this region as par of the Los Reales nappe, attributing local stratigraphic and metamorphic inversions to late- and post-metamorphic folding and normal faulting.

3. Samples and microstructural methods

3.1. Sampling strategy

A total of 44 oriented micaschist samples were studied containing garnet, staurolite, plagioclase, and/or andalusite porphyroblasts with well developed inclusion trails. A list of these samples can be found in the electronic supplement indicating sample locations, the type of lithology and index minerals identified. No mafic lithologies were investigated as these are generally fine grained granoblastic rocks lacking large porphyroblasts with inclusion trails. Thirty-six of the studied samples are dark schists and metapsamites from the Variscan basement of the Los Reales nappe, one (sample B13c) is a similar rock from the Variscan basement of the Veleta subcomplex, and seven are light schists from the post-Variscan cover of the Mulhacen nappe. These samples come from 15 areas indicated with roman numbers in Figs. 2a, b and 3. Areas I to V belong to the 'Filali schists overlying the Beni-Bousera peridotites in the Rif. Gueydan et al. (2015) studied three samples from Area V and deduced early Barrovian conditions (5.4-8 kbar/520-620°C) from mineral inclusions in garnet porphyroblasts (Ilm, Ru, Bi, Mu, Ky) followed by decompression and heating (4-7 kbar / 620-660°C) recorded by matrix minerals (Bi, St, Plg, And, Sil) dated in the Early Miocene.

Area VI (northwest of Ceuta) is a coastal outcrop of strongly folded Paleozoic schists of the Beni-Mzala subunit (Upper Sebtides) that structurally overlies the Filali schists (Lower Sebtides). Bouybaouene et al. (1999) estimated high-pressure - low-temperature conditions of 12 kbar / 500°C) in these rocks, which do not show the same signs of strong heating during decompression as the Filali schists. Homonnay et al. (2018) interpreted this difference in terms of a paired metamorphic belt, with the Beni-Mzala unit representing the lower plate, and the Filali schists (Los Reales nappe) the upper plate affected by high heat flow.

Areas VII and VIII (western Betics) belong to the Jubrique schists cropping out west of and structurally above the Bermeja peridotite massif. Balanya et al., (1997) and Massonne (2014) estimated pressures of 10-13 kbar 600-700°C here, followed by near-isothermal decompression in the early Miocene for the structurally lowest and highest-grade part of this unit. A similar metamorphic path was deduced by Azañón by et al. (1998) and García-Casco et al., (1999) in Areas IX, X and XI in the Central Alpujarrides (Fig. 3).

The eight newly studied samples from the Nevado-Filabride come from three areas in the Sierra Nevada (XII, XIII, XIV) and the western Sierra de los Filabres (Area XV). Two of these samples, B13c and 46.8.1, were already the object of highly detailed microstructural analysis focusing on the porphyroblast rotation / non-rotation question by Aerden et al., (2010; their 'sample B') and Aerden & Ruiz-Fuentes (2020), respectively.

3.2. Measuring strikes of inclusion trails on horizontal sections

The strikes of relatively straight inclusion-trails of individual porphyroblasts were measured in oriented horizontal thin sections and XCT slices. A total of 1760 measurements were made and plotted in moving-average rose diagrams made with the program 'MARD' of Munro & Blenkinsop (2012). As pointed out by these authors, such rose diagrams are more adequate for identifying modal maxima in a set of continuous directional data (0-360°) as the more traditional binned rose diagrams. The latter are significantly influenced by the choice of bin boundaries and bin widths. A counting window of 21° was used except where specified otherwise and non equal-area plotting was selected. These moving-average rose diagrams are shown in column A of Fig. 4 for garnet, plagioclase, staurolite and/or andalusite porphyroblasts.

3.3. Measuring average FIA trends using sets of radial thin sections

'FIA' is an acronym of Foliation Inflexion/Intersection Axis and refers to the axis of inclusion-trail curvature, or what was traditionally assumed to be the porphyroblast rotation axes. Complex inclusion trails typically exhibit internal discontinuities or truncations (e.g.

Hayward, 1992) where inclusion trails of more inward porphyroblast zones are intersected by those of more outward zones, hence the name Foliation Inflexion or Intersection Axes. According to the 'non-rotational' model, internal truncations represent the boundaries between superposed crenulation-cleavages that developed against the margins of porphyroblasts with episodic growth histories (Fig. 5a; see also Fig. 3 of Aerden & Sayab, 2008). Hayward's (1990) devised a method to determine the average orientation of FIAs in a sample by cutting multiple vertical thin sections with regular angular spacing around the compass. The method is based on the principle that sigmoidal or spiral-shaped inclusion trails exhibit either an S or Z-asymmetry in cross-section depending on the orientation of the section relative to their FIAs and the viewing direction of the observer. We applied this to 31 of our samples using six vertical thin sections striking N000, N030, N060, N090, N120 and N150, in principle allowing constraining average FIAs to within a 30° trend range. Once the FIA trend is known, the average plunge can also be measured but this was not done for this study because of the large number of extra thin sections needed.

Unfortunately, we only obtained unambiguous results for 10 samples that apparently contain a single set of FIAs with a normal distribution (i.e. 'von Mises' distribution) of their trends. Average FIAs for these samples are represented with bow-chart symbols in column B of Fig. 4. In other samples, no clear switch in dominant inclusion-trail asymmetry could be identified between different thin sections because, as it appeared later from XCT scans, these samples contain multiple FIA sub-sets with different mean trends, and in some cases FIAs with steep plunges that further complicate application of Hayward's (1990) method as discussed by Aerden & Sayab (2020).

3.4. Measuring internal foliation planes and individual FIAs using X-ray tomography

X-ray computed micro-tomography (XCT) was applied to thin-section sized blocks of 26 samples. The blocks were scanned at resolutions of 10 to 30 um with an Xradia 510 (Versa Zeiss) microtomographer at the University of Granada using 140kV voltage and 2500-3200 projections. Orientation arrows made of metal wire were previously stuck on the blocks to aid reorientation of the generated Tiff image-stacks such that East, North and the vertical coincide with the X, Y and Z axes of the image stacks, respectively. Image stacks were processed and analyzed with the open source software package Fiji (Schindelin et al., 2012). Orientations of relatively planar internal foliations present in 16 samples were determined by measuring their strike and pitch on XY, YZ and XZ slices of tomographic image stacks, and then fitting these angles to great circles on a stereonet. Results for individual sample can be found in stereoplots plotting all microstructural data placed in the electronic supplement. The data are also plotted collectively in Fig. 6a and c and will be interpreted in section 4.1.

FIAs of sigmoidal or spiral inclusion trails of individual porphyroblasts were measured analogous to Hayward's (1990) method, but counting with an unlimited number of virtual slices (Huddlestone-Holmes & Ketcham, 2010; Aerden & Ruiz-Fuentes, 2020). FIA trends were first constrained by interactively rotating a vertical slice through a porphyroblast about a vertical axes and recording where the asymmetry of inclusion-trails switches. Subsequently, a new slice was rotated about a horizontal axes oriented normal to the FIA trend and allows to measure the FIA plunge and plunge direction. Error ranges associated with this procedure are estimated as ±5° to ±15°depending on the size and definition of inclusion trails. Quartz-rich inclusion trails are ideal because of the high X-ray attenuation contrast with garnet, but many of our Alpujarride-Sebtide samples contain inclusion trails mainly composed of very fine-grained graphite that were is poorly or not visible in the scans, even at high scanning resolutions. A total of 346 garnet FIAs were measured, which are plotted in stereograms for separate samples in column B of Fig. 4. Some of them also contain great-circles that represent the average orientation of inclusion-trail planes. The same FIAs are also plotted collectively for all samples in (Fig. 6b) to be discussed and interpreted in section 4.1.

3.5. Measuring garnet porphyroblast shapes

Previous 3D studies of garnet porphyroblasts with spiral inclusion trails have found that they commonly have elongate shapes aligned either parallel or perpendicular to their FIAs due to anisotropic growth controlled by the overgrown foliation and/or the overprinting crenulation cleavage that caused porphyroblast growth (Robyr et al., 2007; Aerden & Ruiz-Fuentes, 2020; Sayab et al., 2021). Therefore, we analyzed the shape and shape orientation of all garnet porphyroblasts present in XCT scans in order to test these relationship and consider its implications for the formation mechanism and relative timing of FIAs. The 'BoneJ' plugin of Fiji (Doube et al., 2010) was used for this purpose, which can rapidly calculate best-fit ellipsoids for a large number of objects present in a binary image stacks. To implement this, image stacks were first thresholded (i.e. setting all voxel values outside the range of garnet to zero), then binarized (setting all remaining voxels to 1) and size-filtered to eliminate small particles. In some cases, the 'dilate' tool was still applied to re-join fragments of single garnets separated by fractures and associated alteration.

Well developed preferred shape orientations of garnet crystals were found in all samples with typical X/Z aspect ratios about 2.0. The complete data for X_{GRT}, Y_{GRT} and Z_{GRT} ellipsoid axes can be found in the stereoplots with microstructural data for each sample in the electronic supplement. Figure 6c plots garnet long axes (X_{GT}) and short-axes (Z_{GT}) collectively for all samples and highlights the preferred horizontal and vertical orientations of these elements, respectively, the significance of which is discussed further below. Figure 7 presents contour plots for garnet long axes (X_{GRT}) in individual samples and compares these with the main foliation and lineation in each sample. Figure 4 (column C) plots the trend distributions of X_{GRT} axes in moving-average rose diagrams showing that these commonly coincide with FIAs in the same sample or a particular subset of these (column B). In samples OK4, however, FIAs are aligned with Y_{Grt} axes and normal to X_{GRT} (see Electronic Supplement), and in samples OK4 and in A7 X_{Grt} axes are aligned with the matrix lineation.

3.6. Lineations and fold axes measurements

The precise microstructural characteristics of lineations cannot always be assured in the field. IN some outcrops lineations are clearly defined by crenulation axes or cleavage intersections, while at others they have the appearance of a fine mineral lineation, and still elsewhere lineations cannot be clearly seen. In thin sections and XCT scans, though, we could establish that all lineations more or less finely spaced crenulation or intersection lineations. In two of the Nevado-Filabride samples (53.10 and BET51A), shape analysis of abundant opaque mineral grains with the BoneJ plugin (Fig. 8b and d) demonstrates that crenulation lineations coincide with the mineral elongation direction. Thus, lineations appear to be generally defined jointly by crenulation lineations and mineral elongation. Indeed, stretching or mineral lineations in the Betics are frequently reported as being subparallel to fold axes. Lineations and fold axes are plotted in column D of Fig. 4. They were partially measured in the field or from the sample after reorienting it in the lab, and partially from XCT image stacks by following individual micro-folds through the scans and applying simple trigonometry to the spatial coordinates of different points located on the fold axes.

3.7. Recording the curvature sense of inclusion trails

Column E of Fig. 4 summarizes with straight bars the main microstructural trends defined by the data in columns A-D. Small arrowheads drawn perpendicular to these bars indicate the curvature sense of sigmoidal or spiral inclusion trails when viewed from above looking down on FIA axes. That is, an E-W bar with a north pointing arrowhead symbolizes inclusion trails that curve clockwise in a N-S sections being viewed in westward direction; a N-S trending bar with an east pointing arrowhead corresponds to inclusion trails curving clockwise when viewed northward in an E-W cross section. The sense of inclusion-trail curvature was found to be highly consistent within individual samples except in F9, which contains roughly equal proportions of opposite inclusion trails suggesting bulk-coaxial deformation.

4. Microstructural interpretation

4.1. Preferred orientations of porphyroblasts supporting limited rotation

Several earlier microstructural studies in the Betic Cordillera have concluded a lack of or limited porphyroblast rotation based on (i) constant inclusion-trail orientations unaffected by later folding or non-coaxial deformation in the same sample (Bell & Forde, 1995; Aerden et al., 2010), (ii) vertical and horizontal preferred orientations of inclusion trails in 37 Nevado-Filabride samples, and (c) regionally consistent FIA trends in 85 Nevado-Filabride samples (Aerden & Sayab, 2008; Aerden et al., 2010; Aerden et al., 2013; Aerden & Ruiz-Fuentes, 2020). This and similar evidence in other metamorphic belts cited in the Introduction has been interpreted mainly in terms of alternating crustal shortening and gravitational collapse as drawn conceptually in Fig. 5a and b. This model predicts that FIAs predominantly form with subhorizontal plunges (Fig. 5a, b) and this has been confirmed in 36 samples of the Alps (Bell & Wang, 1999) and 30 samples of NW-Iberia (Aerden, 2004). Aerden et al. (2021), however, recently showed that FIAs in Variscan blueschsists of southern Brittany mainly have moderate to steep plunges. These FIAs are caused by the intersection of differently oriented steeply dipping foliations, which presumably formed during crustal shortening perpendicular to their strikes (Fig. 5c, d). Note that the trends of subhorizontal or gently plunging FIAs and the strike of inclusion-trails both lie normal to the crustal shortening direction in the models of Fig. 5a-d. However, deviations of this ideal orthogonal relationship can be expected due to different factors. First, as a function of the exact timing of porphyroblasts growth during deformation, which determines how much reorientation pre-existing fabrics have undergone before being fixed in porphyroblasts. Secondly, preexisting folds can influence the plunges or trends of FIAs. In particular, where gravitational collapse triggers a first phase of porphyroblast growth in folds with plunging axes, FIAs will inherit the strike of the fold limbs rather being oriented normal to the shortening direction (Fig. 5e). FIAs for subsequent growth stages of porphyroblasts should be less affected by pre-existing or synchronous folding as these FIA form by overgrowth of cleavage planes that intensified against porphyroblast margins oriented normal to the bulk shortening direction (Fig. 5a). Finally, limited differential porphyroblast rotations associated with micro-fracturing and faulting have been demonstrated (Aerden, 1995; Johnson, 2009; Aerden et al., 2010; Aerden & Sayab, 2017; Aerden & Sayab, 2017) can contribute to scattering FIA orientations.

Well developed preferred orientations of porphyroblasts and their internal fabrics will now be described and discussed, that suggest that the above described processes scattering orientations were sufficiently limited to assume the models of Figs. 5a-d as a first-order conceptual framework.

(1) A total of 528 simple (planar) inclusion trails measured in 16 samples exhibit a distinct preference for very steep (70-80°) dip angles (Fig. 5a and d). This is consistent with the generally accepted contractional origin of these fabrics, and implies limited differential porphyroblast rotations thereafter.

(2) A total of 345 garnet FIAs measured in 24 samples exhibit a marked preference for subhorizontal plunges plus a weaker preference for 50-60°. Very similar bimodal plunges of FIAs were reported for 17 Nevado-Filabride samples by Aerden et al (2013, their Fig. 5c) who explained this assuming the FIA mechanisms sketched in Fig. 9b and 9c operating simultaneously at different locations due to deformation partitioning. Garnet long-axes and short-axes also show pronounced preference for subhorizontal and subvertical plunges, respectively, consistent with the common alignment of FIAs with garnet long axes (Fig. 7).

(3) No systematic relationship exists between FIAs versus matrix foliations and lineations in each sample (Fig. 10). This refutes a simple origin of FIAs by porphyroblast rotating in the foliation plane in directions marked by lineations. Instead, internal and external fabrics must have formed in different (superposed) kinematic frames, but this implies that younger matrix deformations did not erase the above described preferred orientations of internal foliations, FIAs and X_{GRT} axes. Nor is a systematic relationship observed between the preferred orientations of garnet long axes in our samples (X_{GRT}) and the macroscopic foliation and lineation in samples (Fig. 7).

(4) A total of 150 individual garnet FIAs measured by XCT in 5 new Nevado-Filabride samples exhibit a similar multimodal distribution of their trends as 87 average FIAs measured previously by Aerden et al. (2013) using radial thin sections. Moreover, a total of 196 FIAs measured in 19 Alpujarride-Sebtide samples show a sufficiently similar distribution of their trends to consider the possibility of a shared or partially shared tectono-metamorphic evolution (Fig. 9c). Three main sets of FIAs can be distinguished colored red, orange and green in Fig. 9 associated with modal maxima at approximately N120, N075 and N165. In the following sections relative and absolute timing evidence will be presented for these FIA sets and for ease

of discussion we will simply refer to 'red', 'orange' and 'green' FIAs without stating the corresponding trends.

4.2. Relative timing criteria for differently oriented FIA sets

Having justified a 'non-rotational' approach in the previous section, four relative-timing criteria can be defined for 'red' (N135-N090), 'orange' (N090-N030) and 'green' (N150-N180) FIAs and associated matrix fabrics.

Criterion 1: Paleogene burial metamorphism in the Alpujarride-Sebtide Complex was accompanied by chloritoid, garnet, and kyanite growth, followed by progressive increase in temperature and decrease in pressure that produced garnet, staurolite and plagioclase, and eventually plagioclase, andalusite and sillimanite (e.g. Gueydan et al., 2015; Balanya et al., 1997; Azañón et al., 1997; see section 3.1.). An example of an early garnet next to a younger andalusite is shown in Fig. 12e. Thus, inclusion trails in garnet porphyroblasts generally predate those of andalusite porphyroblasts, but they may overlap in time with those of staurolite and plagioclase porphyroblasts.

Criterion 2: FIAs oriented parallel to crenulation and fold axes in the matrix are considered to have formed by overgrowth of those crenulations as, for example in sample MT2 or F8 (Fig. 4). In contrast, FIAs oriented oblique or orthogonal to matrix crenulations represent older crenulation axes fixed in porphyroblasts (e.g. samples OK4 or F16).

Criterion 3: Some samples contain porphyroblasts with differently oriented inclusion trails in cores versus rims and thereby directly establish the relative timing of two trends as shown in Fig. 8.

Criterion 4: In most samples, FIA and X_{GRT} trends (columns B and C in Fig. 4) broadly align with the mean strike of inclusion trails (column A) as expected where FIAs have subhorizontal or gentle plunges. In samples containing a high proportion of steeply plunging FIAs, oblique or orthogonal relationships are observed (Fig. 4 - MT9, OK4, B3, A7, 27.2.1, B13c, 66.6.1). In these cases, the strikes corresponds to the overgrown foliation, and the FIAs and X_{GRT} trends to the overprinting crenulation cleavage (Fig. 5d).

4.3. FIA sequence in Alpujarride-Sebtide samples

Relative timing relationships between differently oriented microstructures in our samples are summarized in Fig. 4 (column E) with black arrows pointing from older to younger microstructures. Small numbers next to these arrows refer to the four criteria described in he previous section. We will now describe these relationships in detail starting with samples from the Alpujarride-Sebtide Complex. Note that we not all samples provide clear relative-timing evidence and some paradoxical evidence will be discussed.

Sample F12 (Area V) contains relatively large (2-3 mm) plagioclase porphyroblasts with weakly sigmoidal inclusion trails that yielded a 'green' average FIA (N165 ± 15) with the radial thin-section method. This FIA is parallel to the matrix lineation. Some plagioclase crystals include tiny garnets, which suggests that the FIAs of garnet porphyroblast of other samples from the area are older (criterion 1). This is confirmed by 'red' and 'orange' garnet FIAs in TA1, F5, and F20 surrounded by a younger 'green' matrix lineation (Criterion 2).

Samples OK5, F9 and A7 host garnet, plagioclase and/or staurolite porphyroblasts. Assuming earlier nucleation of garnet, the different inclusion-trail strikes in these minerals are consistent with 'red' FIAs having formed first, followed by 'orange' and then 'green' FIAs (criterion 1; Fig. 12a, d). This is corroborated by 'orange' X_{GRT} axes versus 'red' inclusion-trail strikes in A7 (criterion 4).

Samples B1, B5, B6 and A5 host garnets with 'red' FIAs and/or inclusion-trail strikes wrapped by a subvertical crenulation cleavage with 'orange' strike (criterion 2). Orange X_{GRT} axes in garnets of B3 postdate 'red' strikes of inclusion trails according to criterion 4. Although no FIAs were measured in J3 due to very small garnet sizes (<0.5 mm), X_{GRT} axes in this samples define a strong 'red' maximum whereas late- to post-kinematic andalusite porphyroblasts in the same sample have inclusion-trails with 'green' strikes parallel to the matrix lineation (Criterion 2). A similar relationship is observed between 'red' X_{GRT} axes of small garnets in samples F20 surrounded by 'green' crenulation axes in the matrix.

Samples OK2, OK3, OK4 and OK5 were collected within 150 m of each other along the northern river bank of Oued Kanar. OK5 contains plagioclase porphyroblasts with 'green' strikes and garnets with 'orange' strikes (criterion 1). Garnets in OK3 preserve inclusion trails with orange strikes in their cores versus 'green' inclusion trail strikes in rims continuous with the matrix foliation (Fig. 12c; criterion 3). Garnets in sample OK4 have 'green' X_{Grt} axes oblique to internal foliations with 'red' strikes (criterion 3).

Samples MT9, B3, F9, A7 contain garnets with 'orange' X_{Grt} maxima versus 'red' inclusion trail strikes indicating an older age of the 'red' trend (criterion 4). MT9 contains a 'green' matrix lineation versus 'orange' and 'red' internal fabrics (criterion 2). Sample 60.3.1 hosts garnets with 'red' X_{GRT} axes parallel to the mean strike of inclusion-trails, surrounded by an 'orange' crenulation lineation (criterion 2). Garnets with both 'orange' and 'red' FIAs in 47.4.1 are surrounded by a 'green' matrix lineation.

Eighteen garnet FIAs measured by XCT in sample F16 define two FIA subsets with 'red' and 'orange' trends surrounded by a 'green' matrix lineation (criterion 2). However, X_{Grt} axes of all garnets in the same rock only show a single 'orange' maximum, which suggests that the 'red' FIAs group is a minority and for some reason is over-represented in the 18 manually measured FIAs. This is probably due to the fact that we measured FIAs of the most strongly curved (spiral) inclusion trails as these are ideal for the asymmetry-switch method, whilst most garnets in the sample have straight or weakly curved trails and appear to be associated with the 'orange' FIA group. A similar selection bias may explain non-coincident FIA and X_{GRT} trends in samples OK4 and A7.

So far, all evidence coherently points at a succession of 'red', 'orange', and 'green' crenulation axes in Alpujarride-Sebtide samples whose inclusion in synkinematic porphyroblasts produced FIAs. However, in sample J2 small andalusite porphyroblasts host inclusion trails with bimodal 'red' and 'orange' inclusion-trail mimicking the X_{GRT} trend distribution in sample J3, which occupies a similar structural position in the Jubrique schist. In particular the 'red' strike is not expected for andalusite as this mineral grew much later as garnet and should be associated with the youngest 'green' FIA set. Since these andalusite probably grew during a gravitational collapse stages (e.g. Williams & Platt, 2018), we propose that the strike of their inclusion trails is inherited from pre-existing folds as sketched in Fig. 5e. Samples 47.1.1. and A2 contain garnets with 'green' internal fabrics surrounded by an 'orange' matrix lineation hence indicating an opposite relative timing of both trends as deduced in other samples (Fig. 12b). Evidence presented below for 'orange' and 'green' FIAs having formed broadly synchronous or in alternation in the Nevado-Filabride Complex during the Miocene, when porphyroblast growth had already ceased in the Alpujarride Complex, provides an explanation for these observations.

4.4. FIA sequence in Nevado-Filabride samples

Samples 27.1.2 and 46.8.1 were collected within meters distance from the same outcrop in the western Sierra de los Filabres (Fig. 3a, Area XV). Both are light-colored quartz-rich schists hosting numerous and variably sized garnets (2-12 mm) exhibiting well-developed spiral-shaped inclusion trails. An average FIA trend of N075 ± 15 ('orange') was initially determined for the larger garnets (>5mm) in sample 27.1.2 by studying inclusion trails with a hand lens on differently oriented slabs. Subsequent X-ray tomography in sample 46.8.1 (Aerden & Ruiz Sanchez, 2020) revealed the presence of two additional FIA sets with 'green' and 'red' trends exclusively associated within the fraction of smaller garnets (< 5mm). This mix of three FIA sets is also expressed in the multimodal strikes of inclusion-trails (Fig. 4). Relative timing evidence presented by Aerden & Ruiz Sanchez (2020) was, however, limited to a single porphyroblast apparently preserving an orange FIA in its core and a green FIA in the rim (Criterion 3).

Garnets in samples BET51A preserve inclusion-trails with 'orange' or 'red' strikes in their cores truncated by inclusion trails with 'green' strikes in narrow rims surrounded by an 'orange' matrix lineation (Fig. 8b, c). Garnets in samples 53.10 (Area XII; Fig. 8a, b) and sample 27.2.1 yielded ‘green’ average FIAs (N165 ± 15) in both cases surrounded by an 'orange' matrix lineation. Ruiz-Fuentes & Aerden (2018 - their Fig. 9b) showed that overgrowth of the same matrix lineation by late plagioclase porphyroblasts created a late set of 'orange' FIAs post-dating 'green' FIAs of garnets. Aerden et al. (2013 - their Fig. 3b) reported four samples from Areas XII and XIII that contain plagioclase porphyroblasts with 'orange' or 'green' FIAs versus garnet porphyroblasts with 'red' FIAs. All above described microstructural relationships are consistent with 'red' FIAs having formed first in the Nevado-Filabride complex, followed by an alternation of 'orange' and 'green' FIAs. However, samples B13c presents conflicting evidence for a 'red' FIA that post-dates steeply SE dipping inclusion trails with 'orange' strikes. This discrepancy will be further discussed at the end of section 7.2.

5. Relationships between FIAs and folds

5.1. Genetic relationships between FIA and outcrop-scale folds

The relationships between FIAs and macroscopic folds were studied in three outcrops of the Sebtide Complex. The first is a road outcrop near M'ter (Area 1) where sample MT2 was collected. Decameter-scale folds at this location have subhorizontal WNW-ESE trending axes which are conspicuously parallel to a main group of 'red' FIAs measured in MT2 hence suggesting a genetic link (Fig. 11). Some additional FIAs with different orientations were also detected and are probably related to crenulation cleavages with 'orange' and 'green' trends, which are also developed in the region (Fig. 11b), but not sufficiently intense at this outcrop to have significantly modified the earlier large-scale fold structure (Fig. 11a). Note that FIAs have been shown to develop during early stages of crenulation cleavage development and that they do not imply that the responsible deformation reached large strains (Bell & Hayward, 1991; Adshead-Bell & Bell, 1999). The detailed geometry of inclusion trails in the sample (Fig. 11d) is consistent with these microstructures representing the relics of a subvertical crenulation cleavage (Fig. 11d). Thus, the macroscopic folds can be interpreted to have formed in upright position during crustal shortening, and to have been later reoriented during gravitational spreading associated with thrusts and/or extensional detachments.

At the beach of Targha, well developed cm to m-scale folds developed in finely layered dark-grey schists were studied in two large outcrops from which samples F8, F9 and F20 were taken. The FIAs in these samples again show similar trends as fold axes and crenulation lineations measured in the outcrops and within 3km distance (Fig. 13a). The field data, however, show a larger spread including NW-SE to NNW-SSE trends that are absent in the FIA data. This difference can be interpreted to reflect variable degrees of clockwise reorientation of fold axes that were originally parallel to 'red' FIAs towards a younger 'green' (N165) folding direction. This is also consistent with the observed deflection towards a N-S strike of the matrix foliation against porphyroblast edges in sample F9 (Fig. 13a, b). Internal foliations in all three samples consistently dip steeply with E-W strikes and are continuous with a penetrative matrix schistosity that is tightly folded in the matrix (Fig. 13c) with gently SW dipping axial planes and an associated crenulation cleavage. Thus, the main schistosity formed subvertical due to N-S bulk shortening, and was later folded and rotated to flat lying positions by deformations that involved a component of vertical shortening and created the gently dipping crenulation cleavage.

About 4 km northwest of Ceuta at the beach of Benzú, cm to m-scale folds with steeply south-plunging axes are outlined by thin quartz veins in finely laminated Paleozoic black schists (Fig. 14). Garnets in four samples from the outcrop (B1, B3, B5, B6) preserve a steeply south-west dipping internal foliation that is continuous with the principle matrix schistosity. The latter is tightly folded with vertical axial planes with NE-SW ('orange') strike. Aerden et al. (2010) already studied a thin-section scale fold from the same outcrop hosting numerous small garnets that were shown to have grown during early folding/crenulation stages and to not have experienced significant rotation during further development of folds. This is consistent with 'orange' X_{GRT} axes in sample B3 parallel to the axial planes of the folds (sample B3; Fig. 4). Thus, the outcrop is a good example of the model for steeply plunging FIA drawn in Fig. 5c.

5.2. Relationships between FIAs and regional fold axes and lineation patterns

The relationships between FIAs, fold axes and lineations were further examined by compiling more than 15,000 field data from the 45 works listed in Table I. This data is plotted in 45 moving-average rose diagrams (Figs. 2a, b and 3) and an equal number of interactive stereoplots given as supplementary data made with the 'Stereonet' program of R. Allmedinger. The stereoplots allow inspection of data sub-sets for different structural elements that were distinguished by the original authors. The rose diagrams, in contrast, plot lineations and fold axes together as is justified by the fact that both elements are generally stated to be subparallel by the original authors and as is also evident from the data itself. A single trend maximum can be shared by two or more generations of homo-axial folds that produce type-3 fold interference patterns (Ramsay classification). For example, Simancas (2018) and Rossetti et al. (2005) distinguished two fold generations with similar NE-SW trends and Platt & Behrman (1986) three. Rose diagrams with two or more trend maxima in most cases correspond to different structural generations recognized by the original workers, but some authors simply did not interpret the significance of such variations in their study areas For example, Orozco (1971) interpreted differently oriented sets of fold axes as different generations, but Orozco et al. (1998) ignored the significance of a similar pattern in an adjacent area. Figure 15 highlights remarkably coincident trends of three main sets of linear structures measured in the field versus and FIAs and allows to generalize the direct genetic relationships between both elements described for selected outcrops in the previous section.

The relative timing of field structures with different trends interpreted by the original authors (indicated with black arrows in Figs. 2a, b and 3b, c) also appears to be mostly consistent with that deduced in section 4.3 and 4.4. for FIAs with 'red', 'orange' and 'green' trends. Mazzoli et al. (2013; Fig. 2a - Area 11) and Tubía et al. (1994; Fig. 2 - Area 16) distinguished an early 'red' lineation overprinted by 'orange' lineations or folds. Kornprobst (1974; Areas 1 and 8) distinguished an early 'orange' fold set overprinted by a 'green' fold set. Balanya et al. (1997) deduced the same relative timing for two sets of 'orange' and 'green' lineations in Area 10 (Jubrique Unit), but Argles (1999) interpreted an opposite relative timing of two similar sets of lineation in the Caratraca massif (Area 18).

Sanz-de-Galdeano & Andreo (1995; Area 14b) interpreted a broadly synchronous timing of E-W and N-S trending folds in the Sierra Blanca during development of the Gibraltar Arc involving synchronous westward motion of the Alboran Domain and northward drift of Africa. In the Dorsale Calcaire, Vitale et al. (2014, 2015; Areas 2 and 3) deduced an alternation of 'orange' and 'green' contractional folds and thrust during the Miocene based on stratigraphic criteria and also attributed this to the interference of NW-SE directed Iberia-Africa convergence and perpendicular west or southwestward migration of the Alboran Domain. Orozco (1971) and

Orozco et al. (2004) interpreted N-S trending folds in Areas 25 and 29, respectively, to have overprinted ENE-WSW ('orange') or NW-SE ('red') trending ones. Williams & Platt (2018) proposed two main sets of suborthogonal lineations with 'orange' and 'green' trends in the entire Alpujarride Complex. These would have formed synchronously in deeper and shallower crustal levels, respectively, so that rocks crossing the transition between these domains during their exhumation would record earlier 'orange' lineations and younger 'green' ones. Thus, the relative timing of structures deduced by earlier workers are consistent with an earliest set of linear structures with 'red' trends, followed by 'orange' and 'green' structures that may have formed partially synchronous or in alternation. It is further noteworthy that lineations and fold-axes trends in the Malaguide-Ghomaride Complex (Chalouan & 1Michard, 1990 - Areas 4; Cuevas et al., 2001 - Area 20) exhibit remarkably similar orientation patterns and relative timing relationships as adjacent Alpujarride-Sebtide areas, particularly in the Rif. This suggest that the main deformation phases in this complex are also Alpine.

In the Nevado-Filabride Complex different sets of linear structures (Fig. 3b) show similar directions and relative timing as in surrounding Alpujarride areas (Fig. 3a) although the 'green' maxima of rose-diagram in some areas are more NW-SE oriented. De Jong (1991; Area 41) and Langenberg (1972; Area 42) described an early WNW-ESE trending L_1 lineations ('red') overprinted by more abundant E-W to ENE-WSW trending L_2 lineations and folds ('orange'), which were still followed by weak NNE-SSW ('green') folding. Martínez-Martínez (1986a, 1986b; Area 39) described an earlier 'orange' lineation (N080 trend; L_2) and younger 'green' one (N150; 'L_3' and 'L_m'). Lozano-Rodriguez (2019) mapped detailed fold-interference structures in the western Sierra de los Filabres involving N-S (green) and ENE-WSW (orange) trending folds but did not establish their relative timing.

6. Sm-Nd dating of garnet porphyroblasts

6.1. Dating method

Bulk Sm-Nd garnet geochronology (that is, work on a bulk garnet separate from a single hand specimen) follows the general approach reviewed in Baxter & Scherer (2013) and Baxter et al. (2017). The samples chosen for bulk Sm-Nd garnet geochronology were crushed to a fine gravel using a large tungsten-carbide mortar and pestle. Approximately 20-25%, representing a homogeneous whole rock fraction was set aside for isotopic analysis with care taken not to fractionate based on grain-size. This whole rock separate was powdered in an agate mortar and pestle and sieved to a ≤ 75 µm grain-size. The remaining sample material (approximately 75-80%) was processed to obtain a representative bulk garnet separate. The extraction of garnets from the surrounding matrix was accomplished through an iterative combination of crushing, sieving, magnetic Franz separation, and hand-picking. Once approximately 100 mg of visibly clean garnet was obtained, it was crushed using a small tungsten-carbide mortar and pestle and sieved to a grain size between 75 and 150 µm; anything finer than 75 µm was collected as a "garnet powder" separate. The 75 – 150 µm grain-size was determined by Pollington and Baxter (2011) to be the ideal grain-size to maximize exposure of inclusion phases while minimizing sample loss during the partial dissolution step. To further cleanse the garnet of its contaminating mineral inclusions, both garnet and garnet powder separates were put through a rigorous partial dissolution procedure described below.

Failure to remove contaminating mineral inclusions within garnet can lead to imprecise ages or – if the inclusions are inherited - inaccurate ages. Generally, pure garnet will yield $^{147}Sm/^{144}Nd$ above 1.0 (e.g. Baxter et al. 2017). In the clean lab, the separates were put through a partial dissolution procedure consisting of alternating 7 normal (N) nitric (HNO3) and dilute hydrofluoric (HF) acid steps in an enclosed 7 mL TeflonTM beaker for 2 hours at 120 ˚C for each step. The separates were first put in 2 mL of 7 N nitric to dissolve any exposed non-silicate inclusions. Next, separates were put in anywhere from 10 - 100 µL of concentrated HF and 1 mL Milli-Q H2O partially dissolving the sample to further access inclusions, and to dissolve any silicate inclusions present. The separates were then put back in 7 N HNO3 to remove any secondary fluorides that accumulated during the HF step. These alternating steps were continued until there had been approximately 75 – 95% mass of sample loss. Following partial dissolution, each separate was fully dissolved. All whole rock separates were fully dissolved using the same procedure as garnet and garnet powder separates. After full dissolution samples were stored in an 8:1 aqua regia solution. Prior to column chromatography, sample aliquots were spiked with a mixed ^{150}Nd/^{147}Sm spike for isotope dilution thermal ionization mass spectrometry (ID-TIMS) analysis.

For many of the garnet and garnet powder separates, a ‘leachate’, representing a single combined HF + nitric step was collected during the partial dissolution process. Each leachate collected represents a different stage of sample loss during partial dissolution, and thus represents an intermediate step between the cleaned and uncleaned separate. If the garnet and inclusion phases grew in isotopic equilibrium the leachates should lie along the isochron between pure garnet and whole rock, however if the inclusions have an inherited isotopic signature then the leachate will lie off the isochron.

The isolation of Sm and Nd was accomplished using the three-column procedure described in Harvey and Baxter (2009). The procedure consists of an iron clean-up column using AG50w-X4 resin, rinsed with 1.5 N HCl to remove iron and sample eluted with 6 N HCl, a TRU-spec resin column, rinsed with 2N HNO3 to remove major cations and REEs eluted with 0.05 N HNO3, and a 2-methyl-lactic acid (MLA) column using AG50w-X4 resin conditioned with 10 mL of 0.2 M MLA. This final column was used to separate Sm from Nd and remove isobaric interferences, predominately Pr on Nd and Gd on Sm.

For the majority of samples, Sm and Nd isotopic ratios were analyzed on an Isotopx Phoenix Thermal Ionization Mass Spectrometer at Boston College following the loading methods of Harvey & Baxter (2009). Nd isotopes were loaded with 2µL of 2N nitric onto Re filaments with 2µL of tantalum oxide (Ta2O5) activator slurry added to facilitate greater sample ionization. Samples were run in multi-dynamic mode as the oxide species (NdO+). Instrumentational inducted mass fractionation was normalized to ^{146}Nd/^{144}Nd = 0.7219 using an exponential correction factor. Sm isotopes were loaded with 2µL of 2N nitric onto Ta filaments and run in static mode as metal species (Sm+). Instrumentational inducted mass fractionation was normalized to 149Sm/152Sm = 0.516860 using an exponential correction factor. Both Sm and Nd samples, as well as standards were loaded using parafilmTM dams to decrease sample spread across the filament. Two 4ng loads of an in-house Ames NdO standards were run with every barrel to track the external reproducibility. Over the period of analysis, the $^{143}Nd/^{144}Nd$ long-term value from the Boston College Phoenix was 0.512152 ± 13.25 ppm 2σ (n=32) and $^{147}Sm/^{144}Nd$ external reproducibility is 0.054% based on repeat analysis of a gravimetrically calibrated mixed Sm–Nd solution. One sample (B13c) was analyzed on the Boston University Thermo Triton TIMS also following Harvey & Baxter (2009); these analyses were performed in static mode with amplifier rotation. The Sm run on the Triton was loaded on zone-refined Re filaments. The $^{143}Nd/^{144}Nd$ long-term value from the Boston University Triton during the period of analysis was 0.512120 ± 17.9 ppm 2σ (n=67) and $^{147}Sm/^{144}Nd$ external reproducibility is 0.023%. In isochron error propagation, the larger (poorer) of the external precision or internal analytical precision (in Table II) was used.

6.2. Age results and links with different FIA sets

All samples yielded one or more garnet analysis with $^{147}Sm/^{144}Nd$ above 1.0 (Table II). This is a strong indication that efforts to cleanse garnets of contaminant inclusions were successful, thus producing accurate garnet growth ages. Isochron diagrams and resulting age interpretations are shown in Figure 16 and discussed for each sample below.

Sample B5 (Benzú schists), F16 and MT8 (Filali schists) produced very similar bulk garnet ages of 26.2 ± 2.5 Ma, 24.95 ± 0.61 Ma and 26.9 ± 1.5 Ma, respectively, which agree well with monazite and xenotime ages in the range 21-28 Ma obtained in higher-grade metapelite and orthogneisses near Ceuta (Homonnay et al., 2018) and Ar-Ar ages on micas from lower-grade Sebtide rocks (Michard et al., 1983, 2006; Marrone et al., 2021). Since samples F16 and MT8 have well defined 'orange' X_{GRT} maxima, which are representative of the bulk garnet content, we interpret their isochrons as dating the 'orange' FIA-forming event. In sample B5, however, a 'red' average FIA was determined using 6 vertical thin sections despite a similar isochron age as samples F16 and MT8. This average FIA is based on only few garnets showing spiral inclusion trails, whereas the majority have simple trails with E-W trends and these were already shown to have grown during development of a subvertical crenulation cleavage in the outcrop with an 'orange' strike that deformed an earlier E-W striking subvertical foliation preserved by garnets (see section 5.1. and Fig. 14).

Sample F8 exhibits potential age zonation with a 4-point isochron corresponding to a low-magnetic garnet fraction giving an age of 26.1 ± 1.4 Ma, and a 2-point age of 35.6 ± 2.8 Ma for a high-magnetic garnet fraction presumably richer in Fe-rich inclusions such as magnetite, rutile or ilmenite. Since the presence of two FIA sets with older 'red' and younger 'orange' trends was already interpreted in samples F8, F9 and F20 (Fig. 13), the two ages can be tentatively correlated with to these two FIA sets.

The age of 21.98 ± 0.86 Ma obtained for A7 corresponds to garnets that overgrew a subvertical foliation with ‘red’ strike during the development of an ‘orange’ cleavage (Fig. 12a). Note that the 'red' average FIA trend determined for this sample corresponds to a steeply plunging FIA determined by the intersection of both foliations and hence is consistent with growth during development of the younger one.

Sm-Nd garnet ages obtained in the four Nevado-Filabride samples are all Miocene (22-13Ma; Fig. 16). The youngest age of 12.9 ± 1.6 Ma corresponds to garnets in 27.2.1 from the Mulhacen Complex (Area XV) with ‘green’ FIAs. Sample 27.1.2 collected 300m further south produced an age of 13.62 ± 0.69 Ma for three large garnets with 'orange' FIAs extracted by micro-drilling from a thick section and dated by Farrell et al. (2021, in press). A six-point isochron containing all analyses for sample 53.10 (south-western Sierra Nevada) gives an imprecise age of 16.3 ± 8.4 Ma for garnets with sigmoidal to spiral-shaped inclusion trails defining 'green' FIAs. Considering the high scatter in the data it may be meaningful to consider the possibility of (at least) two age domains. This results in an older 4-point isochron age of 21.8 ± 2.4 Ma (MSWD = 0.49) and a younger 3-point isochron age of 16.5 ± 2.5 Ma (MSWD = 2.29). Both ages include garnet points with relatively high $^{147}Sm/^{144}Nd$ ratios of 0.923 and 1.193 respectively. Therefore, we expect that both age are reliable and not significantly affected by contamination of inherited inclusions.

A 3-point isochron age of 35.5 ± 2.0 Ma was obtained in sample B13c of the Veleta subcomplex for numerous small (1-2 mm) garnets in a matrix composed of quartz, chlorite and phengite. A detailed microstructural description and strain analysis of the sample can be found in Aerden et al. (2010; their 'sample B') who showed that the sample was non-coaxially deformed with the wrong shear sense for porphyroblast rotation.

Figure 17 presents an overview of the range of garnet ages obtained linked to the relative timing of each FIA set (red, orange, green) and compared with earlier published geochronological results that will be discussed further below.

7. Tectonic implications

7.1. Kinematic significance of lineations, foliations and shear bands

Structural sequences deduced by different authors in the Nevado-Filabride Complex over the years vary dramatically as do tectonic interpretations based on these sequences (see Aerden & Sayab, 2008 for a review). Vissers (1981) interpreted four deformation phases related these to southward and northward thrusting normal to fold axes. Platt & Behrman (1986) distinguished five structural generations and attributed these to top-NNE thrusting. Bakker et al. (1989) and De Jong (1993) also recognized five phases but interpreted top-NW thrusting, followed by top-SE extension, followed by top-NNE and -SSW thrusting. Jabaloy-Sanchez et al. (1993) described four foliations and interpreted all except the first one in terms of progressive top-W extensional shearing. Booth et al. (2015) distinguished two foliations and attributed these to top-W thrusting. Aerden et al. (2013) and Ruiz-Fuentes & Aerden (2018) differentiated four foliations in the field (S_2-S_3-S_4-S_5) but concluded a large number based on analysis of internal foliations of porphyroblasts and inferred an alternation of crustal shortening in different directions with transient phases of gravitational collapse.

In the Alpujarride-Sebtide Complex a similar variety of tectonic models are still debated including NE-SW extension in lower crustal levels synchronous with N-S extension at higher levels (Williams & Platt, 2018), NE-SW transpression in lower crustal levels synchronous with N-S gravitational spreading at higher levels (Tubía et al., 1997, 2013), NE-SW extension followed by N-S contraction (Balanya et al., 1997; Azañón et al, 1997; Rossetti et al., 2005) or top-NE thrusting followed by crustal extension (Homonnay et al., 2018). All four models assume a principle foliation (S_2) overprinted by a crenulation cleavage (S_3), but more complex structural succession were deduced by Orozco (1971; 4 folding phases), Platt & Behrman (1986; 3 phases), and are implied by the microstructural evidence resented herein and will be further shown in a forthcoming paper by Ruiz-Fuentes (2022) with new field data and FIAs from the Western and Central Alpujarride Complex.

The difficulty to integrate data sets from different workers in a single tectonic model reflects major uncertainties, not only regarding the number and original orientation of fabrics and structures, but also regarding their kinematic significance. Whereas early workers in the Betics concluded tectonic transport normal to fold axes in directions indicated by the dominant vergence of folds, more recent authors have generally interpreted tectonic transport parallel to stretching lineations supported by shear-sense criteria. Remember that McLachlan (1953) already investigated this question in the Moine schists and concluded tectonic transport normal to the lineation. A closely related question is why mineral lineations are generally subparallel to fold axes in the metamorphic complexes of the Betic-Rif belt, and indeed in most medium to high-grade rocks. This appear to have been rationalized mainly in terms of intense shearing causing reorientation of fold axes and locally producing sheath-folds. However, this model faces two major challenges. First, sheath folds are only rarely observed in outcrop and can be alternatively explained as fold-interference structures. A pluri-kilometric sheath fold proposed by Orozco (2004) and Orozco et al. (2017) in the Sierra de Lujar was reinterpreted as a fold-interference structure by Simancas (2018) after showing the limited curvature of its axes, ubiquitous evidence for meso-scale fold interference and relatively low strains. Major sheath-folds interpreted in the Sierra Blanca and Sierra de la Contraviesa (Alonso-Chaves, 2012; Orozco et al. 2017) can possibly also be reinterpreted in this sense given evidence for two major folding phases in these regions (F_2 and F_3). Eye-shaped outcrop patterns on a mountain slope in the central Betics interpreted from a distance as a possible sheath folds by Williams & Platt (2018 their Fig. 3a), on closer inspection in Google Earth (Lat. 36.897°, Long. -4.02°) are more likely to be a topographic cut effect where an E-W trending anticline is transected by perpendicular mountain valleys.

A second problem is that quantitative strain analysis has only yielded moderate strains (Vissers, 1981: 70% strain; Jabaloy & Lodeiro, 1988: 72% strain; Aerden et al., 2010: 115% strain; Borrodaile, 1976: 150% (minimum); Soto, 1991: 150% strain), which are an order of magnitude smaller as required to rotate fold axes subparallel to the shearing direction (Cobbold & Quinquis, 1980). Recognizing this problem, Soto (1991) suggested that sheath-fold like structures in the eastern Nevado-Filabride Complex formed by vertical shortening and/or shearing of pre-existing folds, whose axes happened to be already parallel to the future stretching direction, and Galindo-Zaldivar (1993) drew an analogy with an elastic plate undergoing folding while being stretched. Note the kinematic similarities of these models with the conceptual FIA models of Fig. 5e and 5b, respectively.

We interpret fold axes-parallel stretching being a consequence of the original orientation of foliations before becoming folded at a low angle with the XZ plane of a superposed deformation. This is expected where crustal shortening alternating with gravitational collapse is associated with tectonic escape or lateral extrusion (Fig. 5b and d). Strongly non-cylindrical folds can locally form, for example, where gravitational collapse is superposed on folds with subvertical axial planes but gently to steeply dipping fold axes shown in Fig. 5d and in Fig. 12 of Aerden et al. (2021). Large coaxial components of deformation implied by these models have been independently concluded from ambiguous or inconsistent shear-sense indicators in the Betics (Platt & Behrman, 1986; Balanya et al., 1997; Précigout et al., 2013) and the Beni-Bousera massif (e.g. Reuber et al. 1982). In contrast, simple-shear dominated deformation is commonly based on observation of shear bands cutting the main foliation at a low angle (e.g. Tubía & Cuevas, 1986; Marrone et al. 2021) and their interpretation analogous to classic S-C-C' fabrics found in shear zones in granites. This completely ignores a potentially complex history through which the main foliation was created, repeatedly folded and reactivated prior to development of the shear bands. Thus, shear bands are only relevant to the latest stages of deformation and possible reactivation of the main cleavage.

7.2. Crustal shortening directions indicated by FIAs and their absolute timing

Following up from the above discussion, we interpret the WNW-ESE trend of 'red' FIAs to witness a NNE-SSW crustal shortening. An Eocene to early Oligocene timing of this tectonism is indicated by our new garnet ages of 35.5 ± 2 Ma for sample B13c (Veleta nappe), and 35.6 Ma ± 2.8 for the high-magnetic garnet fraction of sample F8 (Sebtide complex), and further supported by average U-Pb monazite ages of 40Ma in the Nevado-Filabride Complex (Li & Massonne et al., 2018), 34 ± 7 Ma U-Pb in the Jubrique schists (Massonne, 2017), and a 32.4 ± 3.3 Ma U-Pb age of rutile inclusions in garnets from high-pressure rocks in the Edough Massif in the Kabylias of NE Algeria (Bruguiera et al., 2017). The latter experienced a similar tectonometamorphic evolution as the Alboran Domain as it is also derived from Alkapeca.

Oligocene to early Miocene (27-22Ma) garnet ages for ‘orange’ FIAs in the Alpujarride-Sebtide Complex suggests a change to NW-SE directed compression, whereas 'green' FIAs began to form around 22Ma in the same complex followed by rapid exhumation and heating. In the Nevado-Filabride Complex garnet ages around 13Ma for both 'orange' FIAs (sample 27.1.2) and suborthogonal 'green' FIAs (sample 27.2.1) suggest alternate development or synchronous at different locations due to the partitioning of deformation (Fig. 17). Gueydan et al. (2015) favored a Variscan age of garnet porphyroblasts studied in 3 Filali schists samples without excluding an Alpine age, which is now demonstrated by our garnet geochronology. This implies that the Barrovian metamorphism (see section 3.1.) deduced by these authors from the composition of inclusion trails and host garnets is early-Alpine instead of Variscan, and that the principle internal and external foliations in the Beni-Bousera massif are also Alpine. Monazite inclusions within garnet porphyroblasts dated as Variscan in the granulitic envelope of the Beni-Bousera peridotites and associated leucosomes (Montel et al., 2000) are therefore not related to the principle deformation structures and fabrics in these rocks.

A puzzling question that still needs to be answered is why samples from the Mulhacen subcomplex have so far only yielded Miocene garnet ages between 21 and 12.5 Ma. Yet, Li & Massonne (2018) concluded that garnet growth in a sample from this complex must have commenced in the Eocene based on textural relationships with and monazite grains yielding average ages of 24Ma and 40Ma. Moreover, Santamaría-López et al. (2019) deduced similar peak pressures of about 20 kbar in both complexes so if Eocene garnets are present in the Veleta complex they should also occur in the Mulhacen Complex. A possible reason why this has not been confirmed by dating garnet has to do with the fact that the Mulhacen Complex experienced stronger heating up to about 600°C during its exhumation or re-burial but in any event accompanied by extensive garnet growth (Santamaría-López et al., 2019). In contrast, the lower part of the Veleta nappe from where sample B13c was collected only reached peak temperatures of ca. 525°C (Aerden et al., 2013) and small Eocene garnets in this sample could only be dated thanks to the absence of younger (Miocene) garnet growth stages. Indeed, all garnet ages obtained so far except one (see below) are averages for the bulk garnet content of samples. A bulk garnet age for a samples containing multiple generations of garnet growth can be expected to be strongly skewed towards the particular growth stage that produced the largest volume of garnet. In case of the Mulhacen Complex, this could well be the youngest growth stage around peak temperature conditions. This is supported by the generally much larger garnet size of garnets in the Mulhacen complex as in the Veleta Complex. Significantly, Aerden & Ruiz-Fuentes (2020) demonstrated a mixture of small garnets (< 5mm) with 'red' and 'green' FIAs plus much larger garnets (5-12mm) with 'orange' FIAs in sample 46.8. The large garnets were dated as 13.6 Ma by Farrell et al. (2022). A bulk garnet age for this sample would probably be only slightly older as that of the large garnets and would not reflect the age of the potentially much older small garnets.

A Late Eocene age of garnets in B13c implies that inclusion trails with 'orange' strikes in this sample cannot be correlated with 'orange' FIAs dated as Oligocene and Miocene in other samples and may correspond to the original pre-Alpine (i.e. Variscan) cleavage in these rocks reactivated during the Alpine cycle.

7.3. FIAs compared with plate motions

Fig. 18 shows a series of paleogeographic sketches modified after Faccenna et al. (2014) with plate-motion vectors for Africa and Adria relative to Eurasia and Iberia added based on Rosenbaum et al. (2002), De Mets et al. (2015) and Handy et al. (2015). The Late Eocene motion of Africa in NNE direction is consistent with the development of 'red' FIAs in this period (Fig. 17) but is difficult to reconcile with a NE-SW trending subduction zone as envisaged by, amongst others, Stampfli & Hochard (2009), Frizon Delamotte et al. (2011), or Faccenna et al. (2014), unless the orogen was dominated by strike-slip tectonics at this time. A NNE-SSW shortening direction causing crustal thickening suggests a more E-W running and N-dipping subduction zone as interpreted by Dercourt (1985), Bouillin (1986), Stampfli et al., (1998), Jolivet & Faccenna, (2000), Michard et al., (2006) or Guerrera et al. (2012). Depending on the exact orientation, this boundary may have accommodated shortening with a sinistral strike-slip component as interpreted by Tubía et al., (2013). Note that NNE compression implies tectonics dominated by sinistral transpression in the eastern Pyrenees, Southern France, Sardinia and Corsica as interpreted by Lacombe & Jolivet (2004) and Marroni et al. (2019).

The E-W to NE-SW trend of 'orange FIAs may be related to a NW directed 'Apenninic' subduction superposed on an earlier E-W trending precursor orogen so that Oligocene back-arc basins formed oblique to the previous Betic orogenic front (Doglioni et al. (1997). The NNW-SSE trend of our 'green' FIA cannot be related to the motion of Africa or Adria, but to independent westward motion of the Alboran Domain driven by some combination of subduction roll-back and lateral extrusion between the Iberian and African converging plates.

Interestingly, similar shifts in tectonic directions are recorded in the Iberian Chain, a zone of intraplate deformation in Central-Eastern Spain. Liesa & Simón (2009) reconstructed a sequence of compression directions here based on a large paleostress database. This sequence includes a Middle- Eocene to Late Oligocene NE–SW 'Iberian' compression, followed by a Late Oligocene to Early Miocene NW–SE 'Betic' compression, followed by Miocene 'Guadarrama'- and 'Pyrenean' compression directions oriented NNW–SSE and NNE-SSW, respectively. The 'Iberian' and 'Betic' events can be related to our ‘red’ and ‘orange’ FIA sets, respectively, separated by an anticlockwise swing of the direction of Africa-Iberia convergence from NNE to NW (DeMets, 2015; Jolivet & Faccenna, 2000). The 'Guadarrama' compression is possibly related to 'orange' FIAs trending ENE-WSW in the Nevado-Filabride Complex.

7.4. Polarity of subduction indicated by inclusion trails

Bell & Johnson (1989, their Fig. 25) argued that the dominant curvature sense of sigmoidal or spiral-shaped inclusion trails observed in a region should reflect the vergence of large-thrusts and the polarity (in opposite sense) of subduction. Our 'red' FIA set is defined by inclusion trails that curve anticlockwise in 12 samples (8 Alpujarride-Sebtides, 4 Nevado-Filabrides), clockwise in three samples (2 Alpujarride-Sebtides; 1 Nevado-Filabride sample), and show inconsistent asymmetries in 1 sample (F9; Sebtides) when viewed in westward direction. The clear predominance of anticlockwise curvature implies southward thrusting or northward subduction consistent with Dercourt et al. (1986), Stampfli et al. 1998), Lacombe & Jolivet (2005), Jolivet & Faccenna (2000) or Platt et al. (2013). Note that assuming the orthodox 'snowball' interpretation, an opposite (south-dipping) subduction is implied, favored by Michard et al. (2006) or Leprêtre et al. (2018). Orange FIAs dated as Oligocene in our Alpujarride-Sebtide samples curve anticlockwise in five samples (viewing towards the SW) and clockwise in two samples. This is consistent with unanimously accepted NW directed subduction of Adria below Iberia in this period, but obviously data from mores samples are needed to further test this and we are currently working in that direction. Interestingly, 'orange' FIA in our Nevado-Filabride samples curve predominantly anticlockwise (4 vs. 1) suggesting an opposite (top the SE) subduction direction as proposed by Platt et al. (2006). Study of a larger set of samples is underway to further evaluate this based on a statistically more significant set of data.

7.5. Implications for the mechanism of the Gibraltar Arc

Kornprobst (1974) found that two sets of lineations and fold axes in the Beni-Bousera peridotite massif, in Ceuta and in the southwestern part o the Bermeja Massif have similar orientations and concluded from this that the Gibraltar Arc is not a true orocline in the sense of having formed by bending of an originally straight belt. Our data extend this conclusion to the entire Alboran Domain. The regional consistency of FIA trends and fold trends (Fig. 15) argues against major rigid-body rotations in the Internal Zones during formation of the Gibraltar Arc.

We therefore suggest that remnant magnetization directions interpreted to reflect major rigid-body rotations (e.g. Berndt et al., 2015 and references cite therein) are significantly affected by strain and foliation development. Although paleomagnetic data for the External Zones indicate predominantly clockwise rotations in southern Spain and anticlockwise in the Rif, consistent with westward motion of the Alboran domain (Platt et al., 2013), the data are highly problematic in detail (van Hinsbergen et al. 2020) suggesting they are also strongly influenced by deformation. We envisage the Gibraltar Arc as formed by the superposition of two folding directions with N-S trending 'green' folds developed more intensely in the frontal part of the Arc and 'orange' ones dominating more to the east reflecting Iberia-Africa convergence. Evidence for radial thrusting direction in the External Zones (Platt et al., 2003; Balanya et al., 2007) and coeval stretching parallel to fold-axes in the internal zones, approximately orthogonal to Africa-Iberia convergence, is suggestive of the channeled extrusion models of Gilbert & Merle (1987) and Cruden et al. (2006; their Fig. 10). These models reconcile lateral extrusion normal to plate convergence and synchronous gravitational collapse of the Alboran Domain.

8. Acknowledgments and data availability statement

We thank Ángel Perandrés-Villegas for having made most of the numerous thin sections used for this study and Fátima Linares Ordóñez for X-ray scanning samples at the University of Granada. EFB gratefully acknowledges support from NSF grants EAR-1250497 and PIRE-1545903 as well as start up funds from Boston College. We thank Mike Tappa for assistance with TIMS analysis. DA and ARF gratefully acknowledge financial support through Spanish government project CGL2016-80687-R AEI/FEDER, and project RNM148 of the Andalusian Autonomous government, and specially thank principle investigator Jesús Galindo Zaldivar. ARF acknowledges a PhD grant (FPU) from the Spanish government. We are very grateful to Whitney Behr, Sean Mulcahy and Federico Rossetti for thoughtful reviews that helped improve an earlier manuscript version and to editor Laurent Jolivet for additional suggestions.

FIGURE AND TABLE CAPTIONS

Table I. List of authors whose field data are represented by rose diagrams in Figs. 2a, b and 3. The total numbers of data are indicated.

Table II. Principle Sm-Nd geochronological data

Fig. 1. Geological map and cross section of the principle tectonic units in the Betic-Rif orogen. Peridotite outcrops are labeled BB: Beni-Bousera massif, B: Bermeja massif, C: Caratraca massif, G: Guadaiza massif. TAFS: Trans Alboran Fault.

Fig. 2. Internal Zones of the Western Betics (a) and Rif (b) with sample areas, field areas of previous workers (Table I), and Sm-Nd garnet ages. The locations of the maps are shown in Fig. 1. (c and d) Rose diagrams for lineation- and fold-axes from authors listed in Table I. Numbers refer to field areas in the maps. Black arrow point from older structural trends to younger ones as determined by the original workers.

Fig. 3. (a) Internal Zones of the Central and Eastern Betics with sample areas, field areas of previous workers (Table I), and new Sm-Nd garnet ages indicated. The map location is shown in Fig. 1. (b and c) Rose diagrams for lineation- and fold-axes from authors listed in Table I. Numbers refer to field areas in the maps. Black arrow point from older structural trends to younger ones as determined by the original workers.

Fig. 4. (a) Chart showing the principle collected microstructural data. (Column A) Strike of inclusion trails in staurolite, andalusite, plagioclase (left) and garnet porphyroblasts (right). (Column B) Bow-tie symbols: average FIA trends. Black dots with colored trend lines: individual porphyroblast FIAs. Great circles: representative orientation of internal foliation planes. (Column C) Moving-average rose diagrams for garnet long-axes (X_{GRT}). (Column D): Black dots: matrix lineations. Large white dots: fold axes. (Column E) Trend bars summarizing the main

microstructural trends apparent in columns A to D. Black arrows point from older to younger microstructural trends based on criteria 1 to 4 described in section 4.2. Small arrowheads drawn orthogonal to trend bars indicate the dominant sense of inclusion trail curvature as explained in section 3.7.).

Fig. 5. (a) Conceptual sketch showing how sigmoidal and spiral-shape inclusion trails form by according to the non-rotational model and two real examples, one of which is from a Figure in Platt & Williams (2017). They interpreted clockwise rotation of the porphyroblast, but note that this is contradicted by open internal crenulations whose axial planes are parallel to those of external more tight crenulations. (b) Conceptual diagram for FIA formed by contraction followed by gravitational collapse with constant stretching direction. (c) Superposition of two crustal shortening directions causing a vertical FIA. Note that inclusion trails strike orthogonal to the first shortening direction, whereas porphyroblasts grew elongate normal to the second contraction direction. (d) Similar as (c) but with a pre-existing anticline causing variable FIA plunges with the same trend. (e) Similar as (b) with a pre-existing fold causing FIAs with variable trends.

Fig. 6. (a) Poles of all internal foliation planes measured for this study. (b) All measured FIAs. (c) All garnet porphyroblast long axes (X_{GRT}) and short axes (Z_{GRT}). (d) Histogram for dip angles of internal foliation planes showing a preference for very steep. (e) Histogram for the plunge of all FIAs showing a preference for horizontal with a weaker maximum at 60°. (f) Schematic representation of the measured microstructural elements not showing a systematic relationships with the external foliation and lineation (see Fig. 10).

Fig. 7. (a) Equal-area stereograms for garnet long axes (X_{GRT}) in 20 samples with X-ray tomography. The main cleavage in each sample is represented by black great circles. Note the general preference of X_{GRT} for subhorizontal plunges (see also Fig. 5d) and its independence of the dip or dip direction of the main cleavage suggesting a lack of or limited porphyroblast rotation.

Fig. 8. (a) Microphotograph and line diagram of garnets in sample 53.10.1 preserving NE-SW striking inclusion trails deflected in outer porphyroblast zones towards a subvertical NNW-SSE striking planes. (b) Orientation data with matching colors for microstructures shown in (a). (c) Tomographic slices of sample BET51A showing N-S striking inclusion trails in porphyroblast rims (green) truncating subvertical inclusion trails with NE-SW strike (orange) or NW-SE strike (red) in porphyroblast cores. (d) Orientation data with matching colors for microstructures shown in (c). Note the similar orientations of FIAs and X_{GRT} axes, and the parallelism of opaque mineral grain elongation, crenulation axes and fold axes.

Fig. 9. (a) FIAs of individual garnet porphyroblasts measured in Nevado-Filabride samples and (b) corresponding moving-average rose diagram.(c) Average FIAs determined by Aerden et al. (2013) in 82 samples. (d) FIAs of individual garnet porphyroblasts measured in Alpujarride-Sebtide samples and (e) corresponding moving-average rose diagram. (f) Rose diagrams for all microstructural trends summarized in column E of Fig 3. Red, orange and green colors show the suggested correlation of this data.

Fig. 10. Orientation of FIAs, versus matrix lineation and foliation in 32 of the studied samples. Note the lack a systematic relationship between internal and external fabrics as would be expected if FIA had developed by shearing parallel to the main lineation and foliation. Also note predominantly gentle to subhorizontal plunges of FIAs regardless of the dips or plunges of matrix fabrics.

Fig. 11. (a) Decameter-scale folds in a road outcrop 100m west of the sample location of MT2 (Beni-Bousera massif). The fold axes there are parallel to the main group of ‘red’ FIAs measured in the sample (b) and crenulation axes (c) measured within 3 km distance. (d) Line drawings of representative inclusion trails in MT2 viewed in a vertical N-S thin section interpreted as the relics of a subvertical crenulation cleavage that corresponds to the original orientation of the axial planes of macroscopic folds, before the latter were rotated to a north-dipping position.

Fig. 12. (a) Sketch of garnet and staurolite porphyroblasts in sample A7 with differently striking inclusion-trails consistent with earlier growth of garnet. (b) NNW-SSE striking internal foliation (green) in garnets of sample 47.1.1 surrounded by a ENE-WSW trending (orange) matrix foliation. (c) Horizontal and vertical tomographic slices and corresponding line drawings of garnets in sample OK3. Note the steep dips of internal foliations and steep FIA plunges (black squares) caused by their intersections. (d) Several small staurolite crystals with remarkably constant Si despite variable shapes and shape orientations of the crystals. (e) Vertical thin section striking N150-N330 strike showing a garnet that grew during incipient crenulation cleavage development, and a andalusite porphyroblast that grew after the crenulation cleavage.

Fig. 13. (a) Orientations of FIA, crenulation axes, fold axes and internal foliation planes measured in samples F8, F9 and F20 which all taken at Targha beach within 500m from each other. (b) Horizontal thin section of F9 showing consistently E-W striking inclusion trails in garnets despite complex folding in the matrix. Early isoclinal microfolds (small red arrows) are overprinted by weaker NW-SW trending crenulations (orange). Cleavage is deflected into a N-S direction against porphyroblast margins. (c) Vertical thin section striking N030 containing steeply dipping inclusion trails showing relatively minor variation despite intense folding in the matrix.

Fig. 14. Observations ate different scales for the outcrop of Benzú beach (Ceuta). (a) Line drawing of a horizontal thin section studied by Aerden et al., (2010) showing inclusion trail in small garnets with consistent WNW-ESE strike, despite intense later folding in the matrix. (b) Outcrop-scale folds with steeply SW plunging axis where sample B3 was taken. (c) Plane polarized microscope image of two garnets (highlighted in red) in a horizontal thin section of sample B3 preserving E-W striking inclusion trails ('red') surrounded by the crenulation cleavage shown with orange lines in (a). (d) Orientation data from sample B3 showing inclusion trail striking oblique to garnet elongation trends (X_{GRT}) as explained in section 4.2.

Fig. 15. Overview of the microstructural trends represented in column E of Fig. 4 (white background) and of rose-diagram maxima defined by over 15000 linear field structures measured in different parts of the metamorphic hinterland of the Betic-Rif orogen (black background). The large rose diagram is for 82 average FIAs measured by Aerden et al (2103) in the Nevado-Filabride Complex. The similar multimodal distributions of microstructures and regional-scale fold patterns strongly suggest a direct genetic link.

Fig. 16. Isochron diagrams discussed in section 6.2. of main text.

Fig. 17. Summary of geochronological evidence relevant to this study.

Fig. 18. Paleogeographic sketches modified after Faccenna et al. (2014) with plate motion vectors relative to Eurasia are from Rosenbaum et al. (2002), Handy et al. (2010) and DeMets et al. (2015). See section 7.3. for explanation. The central inset shows the plate motion path followed by Africa relative to Iberia showing a change from NNE to NW directed the exact timing of which is not known. Small colored trend bars below the maps summarize the FIA trends and corresponding Sm-Nd ages. Note that these FIA lie approximately normal to plate convergence vectors for the same ages.

REFERENCES

Adshead-Bell, N.S. and Bell T.H. (1999) The progressive development of a macroscopic upright fold pair during five near-orthogonal foliation-producing events: complex microstructures versus a simple macrostructure. Tectonophysics 306 (1999) 121–147.

Aerden, D. G. A. M. (1994). Kinematics of orogenic collapse in the Variscan Pyrenees deduced from microstructures in porphyroblastic rocks from the Lys-Caillaouas massif. Tectonophysics, 238(1–4). doi:10.1016/0040-1951(94)90053-1

Aerden, D. G. A. M. (1995). Porphyroblast non-rotation during crustal extension in the Variscan Lys-Caillaouas Massif, Pyrenees. Journal of Structural Geology, 17(5). doi:10.1016/0191-8141(94)00090-M

Aerden, D. G. A. M. (1998). Tectonic evolution of the Montagne Noire and a possible orogenic model for syncollisional exhumation of deep rocks, Variscan belt, France. Tectonics, 17(1).

Aerden, D. G. A. M. (2004). Correlating deformation in Variscan NW-Iberia using porphyroblasts; implications for the Ibero-Armorican Arc. Journal of Structural Geology, 26(1). doi:10.1016/S0191-8141(03)00070-1

Aerden, D. G. A. M., Bell, T. H., Puga, E., Sayab, M., Lozano, J. A., & Diaz de Federico, A. (2013). Multi-stage mountain building vs. relative plate motions in the Betic Cordillera deduced from integrated microstructural and petrological analysis of porphyroblast inclusion trails. Tectonophysics, 587. doi:10.1016/j.tecto.2012.11.025

Aerden, D. G. A. M. and Ruiz-Fuentes, A.(2020) X-ray computed microtomography of spiral garnets: A new test of how they form, J. Struct. Geol., 136, 104054, doi:10.1016/j.jsg.2020.104054.

Aerden, D. G. A. M., Ruiz-Fuentes, A., Sayab, M., and Forde, a. (2021). Kinematics of subduction in the Ibero-Armorican arc constrained by 3D microstructural analysis of garnet and pseudomorphed lawsonite porphyroblasts from Île de Groix (Variscan belt), Solid Earth, 12, 971–992. doi:10.5194/se-12-971-2021

Aerden, D., & Sayab, M. (2008). From Adria- to Africa-driven orogenesis: Evidence from porphyroblasts in the Betic Cordillera, Spain. Journal of Structural Geology, 30(10). doi:10.1016/j.jsg.2008.06.009

Aerden, D. G. A. M., Sayab, M., & Bouybaouene, M. L. (2010). Conjugate-shear folding: A model for the relationships between foliations, folds and shear zones. Journal of Structural Geology, 32(8). doi:10.1016/j.jsg.2010.06.010

Aerden, D. G. A. M., & Sayab, M. (2017). Probing the prodigious strain fringes from Lourdes. Journal of Structural Geology, 105. doi:10.1016/j.jsg.2017.11.001

Afiri, A., Gueydan, F., Pitra, P., Essaifi, A., & Precigout, J. (2011). Oligo-Miocene exhumation of the Beni-Bousera peridotite through a lithosphere-scale extensional shear zone. Geodinamica Acta, 24(1), 49–60. doi:10.3166/ga.24.49-60

Ali, A. (2010). The tectono-metamorphic evolution of the Balcooma Metamorphic Group, north-eastern Australia: a multidisciplinary approach. Journal of Metamorphic Geology, 28(4), 397–422. doi:10.1111/j.1525-1314.2010.00871.x

Ali, A., Yar, M., Khan, M.A., Faisal, S. (2016) Interrelationships between deformation and metamorphic events across the western hinterland zone, NW Pakistan. Journal of Earth Science volume 27, pages 584–598.

Alonso Chaves, F.M., Orozco, M., 2012. El Complejo Alpujárride de La Axarquía: Zonas de cizalla dúctiles a escala cortical y pliegues recumbentes asociados. Geogaceta 52, 5-8.

Argles, T. W., Platt, J. P., & Waters, D. J. (1999). Attenuation and excision of a crustal section during extensional exhumation: The Carratraca Massif, Betic Cordillera, southern Spain. Journal of the Geological Society, 156(1), 149–162. doi:10.1144/gsjgs.156.1.0149

Augier, R., Agard, P., Monie, P., Jolivet, L., Robin, C., & Booth-Rea, G. (2005). Exhumation, doming and slab retreat in the Betic Cordillera (SE Spain): in situ Ar-40/Ar-39 ages and P-T-d-t paths for the Nevado-Filabride complex. Journal of Metamorphic Geology, 23(5), 357–381. doi:10.1111/j.1525-1314.2005.00581.x

Azañon, J.M., Crespo-Blanc, A., García-Dueñas, V. (1997) Continental collision crustal thinning and nappe forming during the pre-Miocene evolution of the Alpujarride Complex (Alboran Domain, Betics). J. Struct GeoL, 19, 1055-1071.

Balanya, J. C., GarciaDuenas, V., Azanon, J. M., & Sanchez-Gomez, M. (1997). Alternating contractional and extensional events in the Alpujarride Nappes of the Alboran domain (Betics, Gibraltar arc). Tectonics, 16(2), 226–238. doi:10.1029/96TC03871

Balanya, J.C. , Crespo-Blanc,A., Díaz Azpiroz, M., Expósito,, I. Luján, M. (2007) Structural trend line pattern and strain partitioning around the Gibraltar Arc accretionary wedge: Insights as to the mode of orogenic arc building

Baxter E.F., and Scherer E.E. 2013. Garnet: Timekeeper of Tectonometamorphic Evolution. Elements, 9, 433-438

Baxter, E.F., Caddick, M.J., Dragovic, B. (2017). Book Series Reviews in Mineralogy & Geochemistry, 83, 469. 10.2138/rmg.2017.83.15

Behr, W.M., Platt, J.P., 2012. Kinematic and thermal evolution during two-stage exhumation of a Mediterranean subduction complex. Tectonics 31, doi:10.1029/2012TC003121

Bell, T. H. (1985) Deformation partitioning and porphyroblast rotation in metamorphic rocks: A radical reinterpretation, J. Metamorph. Geol., 3, 109–118.

Bell, T.H. (1986) Foliation development and refraction in metamorphic rocks, reactivation of earlier foliations and decrenulations due to shifting patterns of deformation partitioning: Journal of Metamorphic Geology 4, 421-444.

Bell T.H., Bruce M.D. (2006) The internal inclusion trail geometries preserved within a first phase of porphyroblast growth. Journal of Structural Geology 28, 236-252.

Bell, T.H., Forde, A., 1995. On the significance of foliation patterns preserved around folds by mineral overgrowth. Tectonophysics 246, 171-181.

Bell, T.H., Hayward, N., 1991. Episodic metamorphic reactions during orogenesis: the control of deformation partitioning on reaction sites and reaction duration. J. Metamorphic Geol. 9, 619-640.

Bell, T. H., Johnson, S. E. (1989) Porphyroblast inclusion trails: the key to orogenesis, J. Metamorph. Geol., 7, 279–310.

Bell, T. H., & Hayward, N. (1991). Episodic metamorphic reactions during orogenesis - the control of deformation partitioning on reaction sites and reaction duration. Journal of Metamorphic Geology, 9(5), 619–640. doi:10.1111/j.1525-1314.1991.tb00552.x

Bell, T.H., Mares, V.M. (1999) Correlating deformation and metamorphism around arcs in orogens. The American Mineralogist 84, 1727e1740.

Bell, T.H., Rubenach, M.J. and Fleming, P.D., 1986. Porphyroblast nucleation, growth and dissolution in regional metamorphic rocks as a function of deformation partitioning during foliation development. Journal of Metamorphic Geology 4, 37-67.

Bell, T. H., & Sanislav, I. V. (2011). A deformation partitioning approach to resolving the sequence of fold events and the orientations in which they formed across multiply deformed large-scale regions. Journal of Structural Geology, 33(7), 1206–1217. doi:10.1016/j.jsg.2011.03.014

Bell, T. H. and Sapkota, J. (2012) Episodic gravitational collapse and migration of the mountain chain during orogenic roll-on in the Himalayas, J. Metamorph. Geol., 30, 651–666.Bell, T.H., Forde, A., Wang, J., 1995. A new indicator of movement direction during orogenesis - measurement technique and application to the Alps. Terra Nova 7, 500-508.

Bell, T.H., Wang, J., (1999). Linear indicators of movement direction versus foliation intersection axes in porphyroblasts (FIAs) and their relationship to directions of relative plate motion. Earth Science Frontiers 6, 31–46.

Berndt, T; Ruiz-Martinez, VC and Chalouan, A. (2015). New constraints on the evolution of the Gibraltar Arc from palaeomagnetic data of the Ceuta and Beni Bousera peridotites (Rif, northern Africa). J. of Geodynamics 84, 19-39.

Bons, P.D., Jessell, M.W., Griera, A., 2009. Porphyroblast rotation versus nonrotation: conflict resolution! (Comment). Geology 37, e188.

Booth-Rea, G; Azanon, JM; (...); Garcia-Duenas, V., Vidal, O. (2005) Contrasting structural and P-T evolution of tectonic units in the southeastern Betics: Key for understanding the exhumation of the Alboran Domain HP/LT crustal rocks (western Mediterranean). Journal of Metamorphic Geology 23, 357-381. 10.1029/2004TC001640

Borradaile, G. J. (1976). A strain study of a granite-granite gneiss transition and accompanying schistosity formation in the Betic orogenic zone, SE. Spain. J. geol. Soc. Lond. 132, 417-428.

Bouillin, J.P. (1986). Le bassin Maghrébin: une ancienne limite entre l'Europe et l'Afrique à l'ouest des Alpes. B. Soc. Geol. Fr. 8, 547–558.

BouybaoJene, M.L., Alami, R., Azañon-Hernandez, J.M.., Goffe, B. (1999) HP-LT metamorphism of the Filali-Benzou schists (Sebtides, Morocco). Chlortoid-garnet-phengite therrnobarometry. Geogaceta 26.

Brouwer, H.A. (1926) Zur Tektonik der Betischen Kordilleren, Geol. Rundsch., 17, 332-336, 1926.

Bruguiera, O., Bosch, D., Caby, R., Vitale-Brovarone, A., Fernandez, L., Hammorc, D., Laouar, R., Ouabadi, A., Abdallah, N., Mechati, M. (2017) Age of UHP metamorphism in the Western Mediterranean: Insight from rutile and minute zircon inclusions in a diamond-bearing garnet megacryst (Edough Massif, NE Algeria). Earth and Planetary Science Letters 474 (2017) 215–225.

Carminati, E., Lustrino, M., & Doglioni, C. (2012). Geodynamic evolution of the central and western Mediterranean: Tectonics vs. igneous petrology constraints. Tectonophysics, 579(SI), 173–192. doi:10.1016/j.tecto.2012.01.026

Carminati, E., Wortel, M. J. R., Spakman, W., & Sabadini, R. (1998). The role of slab detachment processes in the opening of the western-central Mediterranean basins: Some geological and geophysical evidence. Earth and Planetary Science Letters. doi:10.1016/S0012-821X(98)00118-6

Chalouan, A., & Michard, A. (1990). The Ghomarides nappes, Rif coastal range, Morocco - a Variscan chip in the Alpine belt. Tectonics, 9(6), 1565–1583. doi:10.1029/TC009i006p01565

Cobbold, P.R., Quinquis, H., 1980. Development of sheath folds in shear regimes. Journal of Structural Geology 2, 119e126.

Cruden, A. R., Nasseri, M. H. B., & Pysklywec, R. (2006). Surface topography and internal strain variation in wide hot orogens from three-dimensional analogue and two-dimensional numerical vice models. In Buiter, SJH and Schreurs, G (Ed.), Analogue and numerical modelling of crustal-scale processes (vol. 253, pp. 79–104). Geological Soc. Publishing House. doi:10.1144/gsl.sp.2006.253.01.04

Cuevas, J., Navarro-Vilá, F. Tubía, J.M. 2001. Evolución estructural poliorogénica del Complejo Maláguide (Cordilleras Béticas). Boletín Geológico y Minero 112 (3): 47-58.

De Jong, K., 1991. Tectonometamorphic studies and radiometric dating in the Betic Zone (SE Spain) with implications for the dynamics of extension and compression in the western Mediterranean area. PhD Thesis, Vrije UNiversiteit, Amsetrdam, 204pp.

De Jong, K., (1993). Redefinition of the deformation scheme of the Mulhacen Complex and implications for the relative timing of the overthrusting of the Alpujarride Complex in the Betic Zone (SE Spain). Geologie en Mijnbouw 71, 317-326.

Dercourt, J., Zonenshain, L. P., Ricou, L. E., Kazmin, V. G., Lepichon, X., Knipper, A. L., et al. (1986). Geological evolution of the tethys belt from the atlantic to the pamirs since the lias. Tectonophysics, 123(1–4, 1), 241–315. doi:10.1016/0040-1951(86)90199-X

Doglioni, C., Gueguen, E., Sabat, F., & Fernandez, M. (1997). The Western Mediterranean extensional basins and the Alpine orogen. Terra Nova, 9(3), 109–112. doi:10.1046/j.1365-3121.1997.d01-18.x

Doube M, Kłosowski MM, Arganda-Carreras I, Cordeliéres F, Dougherty RP, Jackson J, Schmid B, Hutchinson JR, Shefelbine SJ. (2010) BoneJ: free and extensible bone image analysis in ImageJ. Bone 47:1076-9. doi: 10.1016/j.bone.2010.08.023

Esteban, J. J., Cuevas, J., Tubía, J. M., Sergeev, S., & Larionov, A. (2011). A revised Aquitanian age for the emplacement of the Ronda peridotites (Betic Cordilleras, southern Spain). Geological Magazine, 148(1), 183–187. doi:10.1017/S0016756810000737

Evins, P.M., 2005. A 3D study of aligned porphyroblast inclusion trails across shear zones and folds. Journal of Structural Geology 27, 1300–1314.

Faccenna, C; Becker, TW; Lucente, FP et al. 2001. History of subduction and back-arc extension in the Central Mediterranean. Geophysical Journal International 145, 809-820.

Faccenna, C., Becker, T. W., Auer, L., Billi, A., Boschi, L., Brun, J. P., et al. (2014). Mantle dynamics in the Mediterranean. Reviews of Geophysics, 52(3), 283–332. doi:10.1002/2013RG000444

Fay, C., Bell, T. H., & Hobbs, B. E. (2008). Porphyroblast rotation versus nonrotation: Conflict resolution! GEOLOGY, 36(4), 307–310. doi:10.1130/G24499A.1

Fay, C., Bell, T. H., & Hobbs, B. E. (2009). Porphyroblast rotation versus nonrotation: Conflict resolution! : Reply. Geology, 37(2), E188. doi:10.1130/G25630Y.1

Frizon de Lamotte, D., Raulin, C., Mouchot, N., Wrobel-Daveau, J.-C., Blanpied, C.,Ringenbach, J.-C., 2011. The southernmost margin of the Tethys realm during the Mesozoic and Cenozoic: initial geometry and timing of the inversion processes.Tectonics 30. doi:10.1029/2010TC002691, 2011

Galindo-Zaldivar, J., 1993. Geometría de las deformaciones Neógenas en Sierra Nevada (Cordilleras Beticas). PhD Thesis, Universidad de Granada, 249pp.

Garcia-Casco, A., & Torres-Roldan, R. L. (1999). Natural metastable reactions involving garnet, staurolite and cordierite: implications for petrogenetic grids and the extensional collapse of the Betic-Rif Belt. Contributions to Mineralogy and Petrology, 136(1–2), 131–153. doi:10.1007/s004100050528

García-Dueñas, V., Martínez-Martínez, J.M., Orozco, M., Soto, J.I. (1988) Plis nappes, cisaillements syn- à post-métamorphiques et cisaillements ductiles-fragiles en distension dans les Névado-Filabrides (Cordillères bétiques, Espagne). C. R. Acad. Sci., Série 2, 307, 1389-1395.

Gardner, J., Wheeler, J. (2021) The influence of large second phase grains on microstructural evolution during diffusion creep. Journal of Structural Geology 148. doi:10.1016/j.jsg.2021.104371

Gilbert, E., & Merle, O. (1987). Extrusion and radial spreading beyond a closing channel. Journal of Structural Geology, 9(4), 481–490. doi:10.1016/0191-8141(87)90123-4

Gómez-Pugnaire, M.T., López Sánchez-Vizcaíno,V., Fernández-Soler, J.M. & Acosta-Vigil, A. (2019). Mesozoic and Cenozoic Magmatism in the Betics. In C. Quesada and J. T. Oliveira (eds.), The Geology of Iberia: A Geodynamic Approach, Regional Geology Reviews, doi:10.1007/978-3-030-11295-0_14l

Guerrera, F., Martín-Algarra, A., & Martín-Martín, M. (2012). Tectono-sedimentary evolution of the "Numidian Formation" and Lateral Facies (southern branch of the western Tethys): Constraints for central-western Mediterranean geodynamics. Terra Nova. doi:10.1111/j.1365-3121.2011.01034.x

Gueydan, F., Pitra, P., Afiri, A., Poujol, M., Essaifi, A., & Paquette, J.-L. (2015). Oligo-Miocene thinning of the Beni Bousera peridotites and their Variscan crustal host rocks, Internal Rif, Morocco. Tectonics, 34(6), 1244–1268. doi:10.1002/2014TC003769

Handy, M. R., Schmid, S. M., Bousquet, R., Kissling, E., & Bernoulli, D. (2010). Reconciling plate-tectonic reconstructions of Alpine Tethys with the geological-geophysical record of spreading and subduction in the Alps. Earth-Science Reviews, 102(3–4), 121–158. doi:10.1016/j.earscirev.2010.06.002

Handy, M.R., Ustaszewski, K., Kissling, E., 2015. Reconstructing the AlpseCarpathianseDinarides as a key to understanding switches in subduction polarity, slab gaps and surface motion. Int. J. Earth Sci. 104, 1e26.

Harvey J. and Baxter E.F., 2009. An improved method for TIMS high precision neodymium isotope analysis of very small aliquots (1 – 10 ng). Chemical Geology, 258, p. 251-257.

Hayward, n. (1990). Determination of early fold axis orientations in multiply deformed rocks using porphyroblast inclusion trails. Tectonophysics, 179(3–4), 353–369. doi:10.1016/0040-1951(90)90301-N

Hayward, N. (1992). Microstructural analysis of the classical spiral garnet porphyroblasts of south-east Vermont - evidence for non-rotation. Journal of metamorphic geology, 10(4), 567–587. doi:10.1111/j.1525-1314.1992.tb00106.x

Hickey, K. A., & Bell, T. H. (1999). Behaviour of rigid objects during deformation and metamorphism: a test using schists from the Bolton syncline, Connecticut, USA. Journal of Metamorphic Geology, 17(2), 211–228.

Homonnay, E., Corsini, M., Lardeaux, J.-M., Romagny, A., Munch, P., Bosch, D., et al. (2018). Miocene crustal extension following thrust tectonic in the Lower Sebtides units (internal Rif, Ceuta Peninsula, Spain): Implication for the geodynamic evolution of the Alboran domain. Tectonophysics, 722, 507–535. doi:10.1016/j.tecto.2017.11.028

Huddlestone-Holmes, C. R., & Ketcham, R. A. (2010). An X-ray computed tomography study of inclusion trail orientations in multiple porphyroblasts from a single sample. Tectonophysics, 480(1–4), 305–320. doi:10.1016/j.tecto.2009.10.021

Jabaloy Sánchez, A. 1993. La estructura de la region occidental de la Sierra de los Filabres (Cordilleras Béticas). PhD Thesis, Universidad de Granada, Monografías del Sur, 199 pp.

Jabaloy, A., Galindo-Zaldivar, J., Conzález-Lodeiro, F. (1993). The Alpujarride-Nevado-Filabride extensional shear zone, Betic Cordillera, SE Spain. Journal of Structural Geology 15, 552–569.

Jabaloy, A. and González Lodeiro, F. (1988) La deformacion en los bloques de techo y muro de los cabalgamientos de las unidades inferiores Nevado-filabrides (Cordilleras Beticas, SE. España). Estudios geol., 44: 253-261.

Jabaloy Sánchez, A., Padrón-Navarta, J.A., Gómez-Pugnaire, M.T., López Sánchez-Vizcaíno, V., Garrido, C.J., 2019. Alpine Orogeny: Deformation and Structure in the Southern Iberian Margin (Betics s.l.). In: C. Quesada and J. T. Oliveira (eds.), The Geology of Iberia: A Geodynamic Approach. Regional Geology Reviews, doi:10.1007/978-3-030-11295-0_10

Johanesen, K., Platt, J.P., Kaplan, M.S., Ianno, A.J. (2014). A revised thermal history of the Ronda peridotite, S. Spain: New evidence for excision during exhumation 393, 187-199. 10.1016/j.epsl.2014.01.024

Johnson, S.E. (1992) Sequential porhyroblast growth during progressive deformation and low-P high-T (**LPHT)** metamorphism, Cooma Complex, Australia. Tectanophysics, 214 (1992) 311-339.

Johnson, S.E. (2009) Porphyroblast rotation and strain localization: Debate settled! Geology 37;663-666 doi: 10.1130/G25729A.1

Jolivet, L., & Faccenna, C. (2000). Meditterranean extension and the Africa-Eurasia collision. Tectonics. doi:10.1029/2000TC900018

Jung, W. S., Ree, J. H., & Park, Y. (1999). Non-rotation of garnet porphyroblasts and 3-D inclusion trail data: an example from the Imjingang belt, South Korea. Tectonophysics, 307(3–4), 381–395. doi:10.1016/S0040-1951(99)00105-5

Kim, H. S., & Ree, J.-H. (2013). Permo-Triassic changes in bulk crustal shortening direction during deformation and metamorphism of the Taebaeksan Basin, South Korea using foliation intersection/inflection axes: Implications for tectonic movement at the eastern margin of Eurasia during the Songrim (Indosinian) orogeny. Tectonophysics, 587(SI), 133–145. doi:10.1016/j.tecto.2012.08.033

Kirchner, K.L., Behr, W.M., Loewy, S., and Stockli, D.F. (2016) Early Miocene subduction in the western Mediterranean: Constraints from Rb-Sr multimineral isochron geochronology. Geochem. Geophys. Geosyst., 17, 1842–1860, doi:10.1002/2015GC006208.

Kornprobst. J. Le socle ancien polymétamorphique dans les zones internes de la partie occidentale des chaînes bético-rifaines : similitudes pétrographiques et constance des directions tectoniques anté-alpine. C. R. Acad. Sc. Paris, 272 (D), 1204-1207.

Kornprobst. J. (1974). Contribution à L'étude Pétrographique et Structurale de la Zone Interne du Rif (Published Doctorate Thesis). Notes et Mémoirs du Service Géol. 251. Editions du Services Géologiques du Maroc, Rabat.

Lacombe, O., & Jolivet, L. (2005). Structural and kinematic relationships between Corsica and the Pyrenees-Provence domain at the time of the Pyrenean orogeny. Tectonics, 24(1). doi:10.1029/2004TC001673

Langenberg, C.W., 1972. Polyphase deformation in the eastern Sierra de los Filabres, N of Lubrin, SE Spain. GUA papers of Geology, Series 1, no. 2, 1972, 81pp.

Leprêtre, R., de lamotte, D. F., Combier, V., Gimeno-Vives, O., Mohn, G., & Eschard, R. (2018). The Tell-Rif orogenic system (Morocco, Algeria, Tunisia) and the structural heritage of the southern Tethys margin. BSGF-Earth Sciences Bulletin, 189(2). doi:10.1051/bsgf/2018009

Li, B., & Massonne, H.-J. (2018). Two Tertiary metamorphic events recognized in high-pressure metapelites of the Nevado-Filabride Complex (Betic Cordillera, S Spain). Journal of Metamorphic Geology, 36(5, SI), 603–630. doi:10.1111/jmg.12312

Liesa, C.L. and Simón, J.L. (2009) Evolution of intraplate stress fields under multiple remote compressions: The case of the Iberian Chain (NE Spain). Tectonophysics 474, 144-159. doi:10.1016/j.tecto.2009.02.002

Lonergan, L., and J. P. Platt (1995), The Malaguide-Alpujarride boundary: A major extensional contact in the Internal Zone of the eastern Betic Cordillera, SE Spain, J. Struct. Geol., 17, 1655–1671.

Lonergan, L., & White, N. (1997). Origin of the Betic-Rif mountain belt. Tectonics. doi:10.1029/96TC03937

Lozano-Rodríguez, J.A. (2019) Estudio petrológico, geoquímico y geocronológico comparado de las Ofiolitas Béticas de Sierra de Baza con otras Ofiolitas Béticas. Ph.D. Thesis Universidad de Granada, 383 pp. https://digibug.ugr.es/handle/10481/54877

Marchant, R.H. and Stampfli, G.M. (1997) Subduction of continental crust in the Western Alps. Tectonophysics 269, 217-235

Marrone. S., Monié, P., Rossetti, F., Lucci, F., Theye. T. Bouybaouene, M.L., Najib Zaghloul, M. (2021) The pressure–temperature–time–deformation history of the Beni Mzala unit (Upper Sebtides, Rif belt, Morocco): Refining the Alpine tectono-metamorphic evolution of the Alboran Domain of the western Mediterranean. J Metam Geol. doi:10.1111/jmg.12587.

Marroni, M., Meneghini, F., Pandolfi, L., Hobbs, N., & Luvisi, E. (2019). The Ottone-Levanto Line of Eastern Liguria (Italy) uncovered: a Late Eocene-Early Oligocene snapshot of Northern Apennine geodynamics at the Alps/Apennines Junction. Episodes, 42(2), 107–118. doi:10.18814/epiiugs/2019/019009

Martínez Martínez, J.M., 1986a. Fabricas y texturas miloniticas. Cinematica de las traslaciones en el complejo Nevado-Filabride (Cordilleras Beticas, España). Estudios Geológicos 42, 291-300.

Martínez Martínez, J.M., 1986b. Evolución tectonometamorpfica del complejo Nevado-Filabride en el sector de unión entre Sierra Nevada y Sierra de los Filabres (Cordilleras Beticas), Published Ph.D. Thesis, Cuad. Geol. Univ. Gran,. 13, 1-194.

Massonne, H.-J. (2014). Wealth of P-T-t information in medium-high grade metapelites: Example from the Jubrique Unit of the Betic Cordillera, S Spain. Lithos, 208, 137–157. doi:10.1016/j.lithos.2014.08.027

Mazzoli, S., & Martin Algarra, A. (2011). Deformation partitioning during transpressional emplacement of a `mantle extrusion wedge': the Ronda peridotites, western Betic Cordillera, Spain. Journal of the Geological Society, 168(2), 373–382. doi:10.1144/0016-76492010-126

Mazzoli, S., Martín-Algarra, A., Reddy, S.M., López Sánchez-Vizcaíno, V., Fedele, L., Noviello, A., (2013). The evolution of the footwall to the Ronda subcontinental mantle peridotites: insights from the Nieves Unit (western Betic Cordillera). J. Geol. Soc. 170, 385e402. doi:10.1144/jgs2012-105.

Mclachlan, G. R. (1953) Bearing of roiied garnets on the concept of 6-lineation in Moine rocks. Geol. Mag. 90(3), 172-6.

Michard, A., Chalouan, A., Feinberg, H., Goffe, B., & Montigny, R. (2002). How does the Alpine belt end between Spain and Morocco? Bulletin de la Societe Geologique De France, 173(1), 3–15. doi:10.2113/173.1.3

Michard, A., Negro, F., Saddiqi, O., Bouybaouene, M. L., Chalouan, A., Montigny, R., & Goffe, B. (2006). Pressure-temperature-time constraints on the Maghrebide mountain building: evidence from the Rif-Betic transect (Morocco, Spain), Algerian correlations, and geodynamic implications. Comptes Rendus Geoscience, 338(1–2), 92–114. doi:10.1016/j.crte.2005.11.011

Monié, P., Galindo-Zaldivar, J., Lodeiro, F. G., Goffe, B., & Jabaloy, A. (1991). Ar-40/Ar-39 geochronology of alpine tectonism in the betic cordilleras (southern Spain). Journal of the geological society, 148(2), 289–297. doi:10.1144/gsjgs.148.2.0289

Montel, J.M., Kornprobst, J., Vielzeuf, D. (2000) Preservation of old U–Th–Pb ages in shielded monazite: example from the Beni Bousera Hercynian kinzigites (Morocco). J.Metamorph. Geol. 18, 335–342.

Munro, M. A., & Blenkinsop, T. G. (2012). MARD-A moving average rose diagram application for the geosciences. Computers & Geosciences, 49, 112–120. doi:10.1016/j.cageo.2012.07.012

Orozco, M. (1971) Los alpujarrides en sierra de gador oriental. Ph.D. tesis, Universidad de Granada, 379 pp. https://digibug.ugr.es/handle/10481/28618

Orozco, M., Álvarez-Valero, A.M., Alonso-Chaves, F.M., Platt, J.P. (2004). Internal structure of a collapsed terrain. The Lújar syncline and its significance for the fold- and sheetstructure of the Alborán Domain (Betic Cordilleras, Spain). Tectonophysics, 385, 85-104.

Orozco, M., Alonso-Chaves, F.M. (2012). Kilometre-scale sheath folds in the western Betics (south of Spain). International Journal of Earth Sciences (Geologische Rundschau), 101, 505-519.

Orozco, M., Alonso-Chaves, F.M. & Platt, J.P. (2017) Late extensional shear zones and associated recumbent folds in the Alpujarride subduction complex, Betic Cordillera, Southern Spain. Geologica Acta, 15, 51–66.

Peach B.N. (1912) The geology of Ben Wyvis, Carn Chuinneag, Inchbae and the surrounding country. Memoirs of the Gological Survey of Scotland 93, 189pp. Morrison & Gibb Limited, Edinburgh.

Platt, J. P., & Behrmann, J. H. (1986). Structures and fabrics in a crustal-scale shear zone, betic cordillera, SE Spain. Journal of structural geology, 8(1), 15-. doi:10.1016/0191-8141(86)90014-3

Platt, J. P., & Vissers, R. L. M. (1989). Extensional collapse of thickened continental lithosphere: a working hypothesis for the Alboran Sea and Gibraltar arc. Geology. doi:10.1130/0091-7613(1989)017<0540:ECOTCL>2.3.CO;2

Platt, J.P., Kelley, S.P., Carter, A., Orozco, M. (2005) Timing of tectonic events in the Alpujárride Complex, Betic Cordillera, S. Spain. Journal of the Geological Society,London 162, 451–462.

Platt, J. P., Anczkiewicz, R., Soto, J.-I., Kelley, S. P., & Thirlwall, M. (2006). Early Miocene continental subduction and rapid exhumation in the western Mediterranean. Geology, 34(11), 981–984. doi:10.1130/G22801A.1

Platt, J. P., Behr, W. M., Johanesen, K., & Williams, J. R. (2013). The Betic-Rif Arc and Its Orogenic Hinterland: A Review. Annual Review of Earth and Planetary Sciences. doi:10.1146/annurev-earth-050212-123951

Platt, J. P., Vandeneeckhout, B., Janzen, E., Konert, G., Simon, O. J., & Weijermars, R. (1983). The structure and tectonic evolution of the aguilon fold-nappe, sierra alhamilla, betic cordilleras, se spain. Journal of structural Geology, 5(5), 519-. doi:10.1016/0191-8141(83)90057-3

Pollington, A.D., & Baxter E.F., 2001. High precision microsampling and preparation of zoned garnet porphyroblasts for Sm-Nd geochronology. Chemical Geology 281, 270-282. DOI: 10.1016/j.chemgeo.2010.12.014

Poulaki E.M., Stockli, D.F. (2019). Unraveling the tectono-metamorphic evolution of the Nevado Filabride Unit using zircon LA-ICP-MS U-Pb depth profiling and 2-D mapping geochronology (Abstract). In: Workshop Alboran domain and Gibraltar Arc: geological research and natural hazards. Granada, October 16th-18th, 2019, p21-22.

Precigout, J., Gueydan, F., Garrido, C. J., Cogne, N., & Booth-Rea, G. (2013). Deformation and exhumation of the Ronda peridotite (Spain). Tectonics, 32(4), 1011–1025. doi:10.1002/tect.20062

Puga, E., Díaz de Federico, A., Nieto, J.M. (2002) Tectonostratigraphic subdivision and petrological characterisation of the deepest complexes of the Betic zone: a review. Geodinamica Acta 15, 23– 43.

Puga, E., Díaz de Federico, A., Fanning, M., Nieto, J.M., Rodríguez Martínez-Conde, J.A., Díaz Puga, M.A:, Lozano, J.A., Bianchini, G., Natali, C., Beccaluva, L. (2017) The Betic Ophiolites and the Mesozoic Evolution of the Western Tethys. Geosciences 2017, 7, 31; doi:10.3390/geosciences7020031

Reuber, I., Michard, A., Chalouan, A., Juteau, T., & Jermoumi, B. (1982). Structure and emplacement of the alpine-type peridotites from beni bousera, rif, morocco - a polyphase tectonic interpretation. Tectonophysics, 82(3–4), 231–251. doi:10.1016/0040-1951(82)90047-6

Rich, B.H. (2006) Permian bulk shortening in the Narragansett Basin of southeastern New England, USA. J. Struct. Geol. 28, 682-694.

Robyr, M., Vonlanthen, P., Baumgartner, L. P., & GrobetY, B. (2007). Growth mechanism of snowball garnets from the Lukmanier Pass area (Central Alps, Switzerland): a combined mu CT/EPMA/EBSD study. Terra Nova, 19(4), 240–244. doi:10.1111/j.1365-3121.2007.00741.x

Romagny, A., (2014). Evolution des mouvements verticaux n_eog_enes de la cha^_ne du Rif (Nord-Maroc) : apports d'une analyse structurale et thermochronologique. PhD Thesis. Université Nice Sophia Antipolis, 2014.

Rosenbaum, G., Lister, G. S., & Duboz, C. (2002). Relative motions of Africa, Iberia and Europe during Alpine orogeny. Tectonophysics, 359(1–2), 117–129. doi:10.1016/S0040-1951(02)00442-0

Rosenfeld, J.L. (1968). Garnet rotations due to major Palaeozoic deformations in Southeast Vermont. In: Zen, E-An, et al. (Ed.), Studies of Appalachian Geology. Wiley. New York, N.Y., pp. 185–202.

Rossetti, F., Faccenna, C., & Crespo-Blanc, A. (2005). Structural and kinematic constraints to the exhumation of the Alpujarride Complex (Central Betic Cordillera, Spain). Journal of Structural Geology. doi:10.1016/j.jsg.2004.10.008

Royden, L.H., (1993) Evo1ution of retreating subduction boundaries formed during continental colli· sion, Tectonics, 12, 629·638.

Ruiz-Fuentes, A., & Aerden, D. G. A. M. (2018). Transposition of foliations and superposition of lineations during polyphase deformation in the Nevado-Filabride complex: tectonic implications. International Journal of Earth Sciences, 107(6), 1975–1988. doi:10.1007/s00531-017-1582-6

Sanislav, I. V. (2011). A long-lived metamorphic history in the contact aureole of the Mooselookmeguntic pluton revealed by in situ dating of monazite grains preserved as inclusions in staurolite porphyroblasts. Journal of Metamorphic Geology, 29(2), 251–273. doi:10.1111/j.1525-1314.2010.00916.x

Santamaría-López, A., Lanari, P., Sanz-de-Galdeano , C. (2019) . Deciphering the tectono-metamorphic evolution of the Nevado-Filábride Complex (Betic Cordillera, Spain) – A petrochronological study. Tectonophysics 767. doi: 10.1016/j.tecto.2019.06.028

Sanz-de-Galdeano , C. and Andreo, B. (1995). Structure of Sierra Blanca (Alpujarride Complex). Estudios Geologicos, 51: 43-55.

Sanz-de-Galdeano , C., Santamaría-López, A. (2019.) The lithological sequence of the Nevado-Filábride. Complex (Betic Internal Zone) in the sierras Nevada and Filabres. Revista de la Sociedad Geológica de España, 32 (1): 113-126.

Sanz-de-Galdeano , C. (2017) Implication of the geology of the Guadaiza and Verde valleys (Malaga Province, Betic Cordillera) on the position of the Ronda peridotites and the structure of the Alpujarride Complex. Boletin Geologico Y Minero, 128(4), 989–1006. doi:10.21701/bolgeomin.128.4.006

Sayab, M. (2005). Microstructural evidence for N-S shortening in the Mount Isa Inlier (NW Queensland, Australia): the preservation of early W-E-trending foliations in porphyroblasts revealed by independent 3D measurement techniques. Journal of Structural Geology, 27(8), 1445–1468. doi:10.1016/j.jsg.2005.01.013

Sayab, M., Shah, S. Z., & Aerden, D. (2016). Metamorphic record of the NW Himalayan orogeny between the Indian plate-Kohistan Ladakh Arc and Asia: Revelations from foliation intersection axis (FIA) controlled P-T-t-d paths. Tectonophysics, 671. doi:10.1016/j.tecto.2015.12.032

Sayab, M., Suuronen, J.-P., Hölttä, P., Aerden, D., Lahtinen, R., & Kallonen, A. P. (2015). High-resolution X-ray computed microtomography: A holistic approach to metamorphic fabric analyses. Geology, 43(1). doi:10.1130/G36250.1

Schindelin, J.; Arganda-Carreras, I. & Frise, E. et al. (2012), "Fiji: an open-source platform for biological-image analysis", Nature methods 9(7): 676-682, PMID 22743772, doi:10.1038/nmeth.2019

Shah, S. Z., Sayab, M., Aerden, D., & Khan, M. A. (2011). Foliation intersection axes preserved in garnet porphyroblasts from the Swat area, NW Himalaya: A record of successive crustal shortening directions between the Indian plate and Kohistan-Ladakh Island Arc. Tectonophysics, 509(1–2). doi:10.1016/j.tecto.2011.05.010

Skrzypek, E., Schulmann, K., Stipska, P., Chopin, F., Lehmann, J., Lexa, O., Haloda, J. (2011). Tectono-metamorphic history recorded in garnet porphyroblasts: insights from thermodynamic modeling and electron backscatter diffraction analysis of inclusion trails. Journal of metamorphic Geology, 29, 473-496.

Simancas, J.F. (2018) A reappraisal of the Alpine structure of the Alpujarride Complex in the Betic Cordillera: Interplay of shortening and extension in the westernmost Mediterranean. J. Structural Geol. 115 , 231-242. 10.1016/j.jsg.2018.08.001

Soto, J. I., 1991. Estructura y evolución metamórfica del Complejo Nevado-Filábride en la terminación oriental de la Sierra de los Filabres (Cordilleras Béticas). Ph.D. thesis, Universidad de Granada, 205 pp.

Stampfli, G.M., Hochard, C. (2009). Plate tectonics of the Alpine realm. Geol. Soc.,Lond., Spec. Publ. 327, 89e111.

Stampfli,G.M., Mosar, J., Marquer, D, Marchant , R., Baudin, T. Borel, G. (1998) Subduction and obduction processes in the Swiss Alps. Tectonophysics 296, 159–204.

Spry, A. (1963) The origin and sigdicance of snowball structure in garnet, J. of Petrology, 4, 211–222.

Steinhardt, C.K., 1989. Lack of porphyroblast rotation in non-coaxially deformed schists from Petrel-Cove, South Australia and its implications. Tectonophysics, 158, 127-140.

ten Grotenhuis, S.M., Passchier, C.W., Bons, P.D. (2002) The influence of strain localisation on the rotation behaviour of rigid objects in experimental shear zones. Journal of Structural Geology 24, 485-499. doi:10.1016/S0191-8141(01)00072-4

Timms, N. E., 2003. Garnet porphyroblast timing and behaviour during fold evolution: implications from a 3-D geometric analysis of a hand-sample scale fold in a schist. Journal of Metamorphic Geology 21, 853-873.

Tubía, J. M. (1994). The ronda peridotites (Los-Reales-nappe) - an example of the relationship between lithospheric thickening by oblique tectonics and late extensional deformation within the betic-cordillera (Spain). Tectonophysics, 238(1–4), 381–398. doi:10.1016/0040-1951(94)90065-5

Tubía, J. M., Cuevas, J., Navarro-Vila, F., Alvarez, F., & Aldaya, F. (1992). Tectonic evolution of the alpujarride Complex (betic cordillera, southern spain). Journal of structural geology, 14(2), 193–203. doi:10.1016/0191-8141(92)90056-3

Tubía, J. M., Cuevas, J., & Ibarguchi, J. I. G. (1997). Sequential development of the metamorphic aureole beneath the Ronda peridotites and its bearing on the tectonic evolution of the Betic Cordillera. Tectonophysics, 279(1–4), 227–252. doi:10.1016/S0040-1951(97)00124-8

Tubía, J. M., Cuevas, J., & Esteban, J. J. (2004). Tectonic evidence in the Ronda peridotites, Spain, for mantle diapirism related to delamination. Geology, 32(11), 941–944. doi:10.1130/G20869.1

Tubía, J. M., Cuevas, J., & Esteban, J. J. (2013). Localization of deformation and kinematic shift during the hot emplacement of the Ronda peridotites (Betic Cordilleras, southern Spain). Journal Of Structural Geology, 50(SI), 148–160. doi:10.1016/j.jsg.2012.06.010

van Hinsbergen, D. J. J., Torsvik, T. H., Schmid, S. M., Matenco, L. C., Maffione, M., Vissers, R. L. M., et al. (2020). Orogenic architecture of the Mediterranean region and kinematic reconstruction of its tectonic evolution since the Triassic. Gondwana Research, 81, 79–229. doi:10.1016/j.gr.2019.07.009

Vergés, J., & Fernàndez, M. (2012). Tethys-Atlantic interaction along the Iberia-Africa plate boundary: The Betic-Rif orogenic system. Tectonophysics. doi:10.1016/j.tecto.2012.08.032

Vissers, R. L. M., & Meijer, P. T. (2012). Iberian plate kinematics and Alpine collision in the Pyrenees. Earth-Science Reviews, 114(1–2), 61–83. doi:10.1016/j.earscirev.2012.05.001

Vissers, R.L.M., 1981. A structural study of the central Sierra de los Filabres (Betic Zone, SE SPain) with emphasis on deformational processes and their relation to the Alpine metamorphism. (published Ph.D. thesis). GUA papers on Geology, 1, 15, 154 pp.

Vissers, R.L.M., Platt, J.P., Van der Wal, D., 1995. Late orogenic extension of the betic cordillera and the alboran domaind; a lithospheric view. Tectonics 14, 786–803.

Vitale, S., Zaghloul, M. N., Tramparulo, F. D., & El Ouaragli, B. (2014). Deformation characterization of a regional thrust zone in the northern Rif (Chefchaouen, Morocco). Journal of Geodynamics, 77, 22–38. doi:10.1016/j.jog.2013.09.006

Vitale, S., Zaghloul, M. N., El Ouaragli, B., Tramparulo, F. D., & Ciarcia, S. (2015). Polyphase deformation of the Dorsale Calcaire Complex and the Maghrebian Flysch Basin Units in the Jebha area (Central Rif, Morocco): New insights into the Miocene tectonic evolution of the Central Rif belt. Journal of Geodynamics, 90, 14–31. doi:10.1016/j.jog.2015.07.002

Williams, J. R., & Platt, J. P. (2017). Superposed and refolded metamorphic isograds and superposed directions of shear during late orogenic extension in the Alboran Domain, southern Spain. Tectonics, 36(5), 756–786. doi:10.1002/2016TC004358

Williams, J. R., & Platt, J. P. (2018). A new structural and kinematic framework for the Alboran domain (Betic–Rif arc, western Mediterranean orogenic system). Journal of the Geological Society. doi:10.1144/jgs2017-086

Yeh, M. W., & Bell, T. H. (2004). Significance of dextral reactivation of an E-W transfer fault in the formation of the Pennsylvania orocline, central Appalachians. Tectonics, 23(5). doi:10.1029/2003TC001593

Yeh, M.W. (2007). Deformation sequence of Baltimore gneiss domes, USA, assessed from porphyroblast Foliation Intersection Axes. Journal of Structural Geology 29, 881-897.

Zwart, H. J. (1960). The chronological succession of folding and metamorphism in the Central Pyrenees. Geologische Rundschau, 50, 203–218.

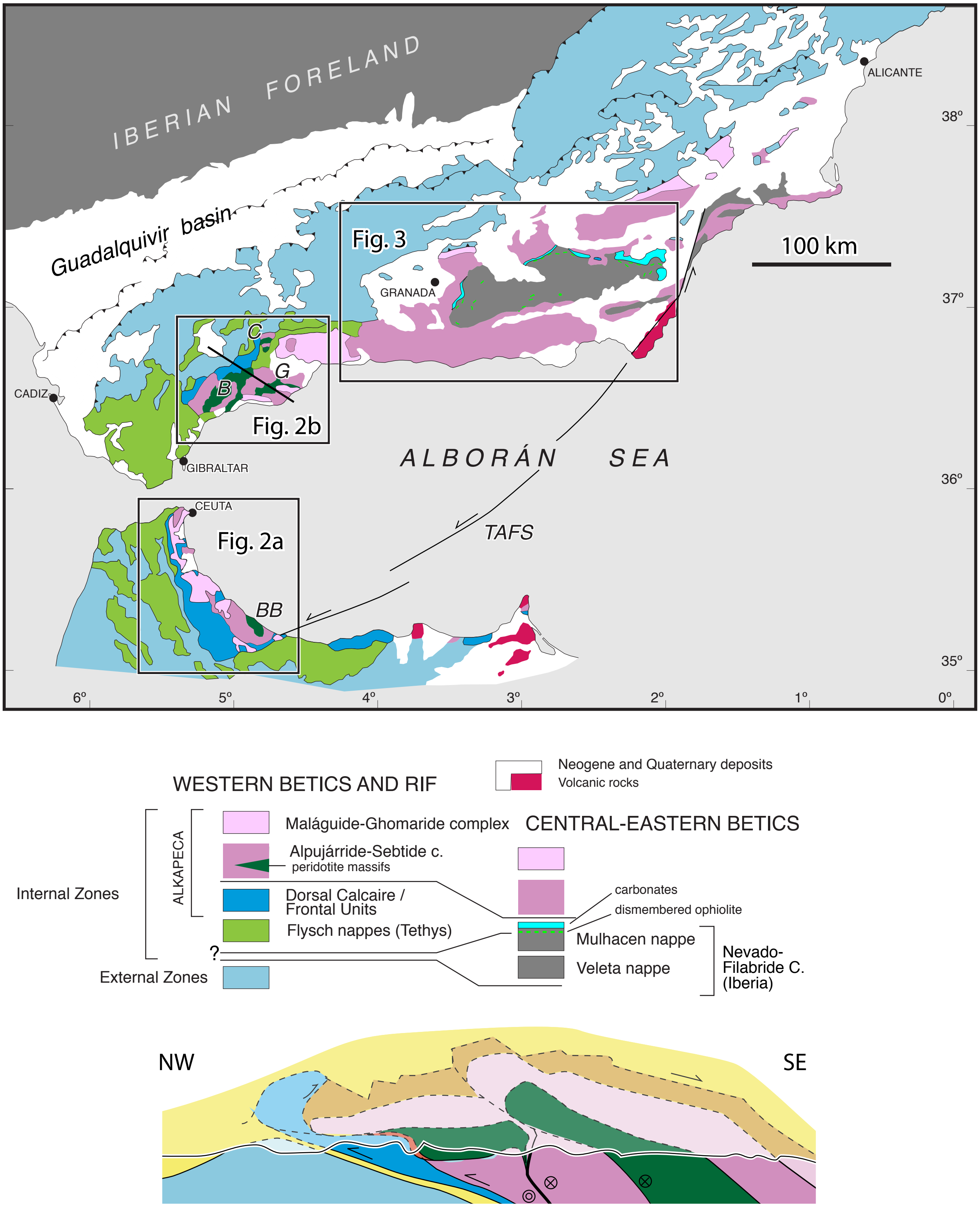
IBERIAN FORELAND
Guadalquivir basin
ALICANTE
38º
37º
36º
35º
Fig. 3
GRANADA
100 km
C
G
B
Fig. 2b
CADIZ
GIBRALTAR
ALBORÁN SEA
CEUTA
Fig. 2a
TAFS
BB
6º
5º
4º
3º
2º
1º
0º
Neogene and Quaternary deposits
Volcanic rocks
WESTERN BETICS AND RIF
CENTRAL-EASTERN BETICS
Internal Zones
ALKAPECA
Maláguide-Ghomaride complex
Alpujárride-Sebtide c.
peridotite massifs
Dorsal Calcaire / Frontal Units
Flysch nappes (Tethys)
External Zones
?
carbonates
dismembered ophiolite
Mulhacen nappe
Veleta nappe
Nevado-Filabride C. (Iberia)
NW
SE

Fig. 1

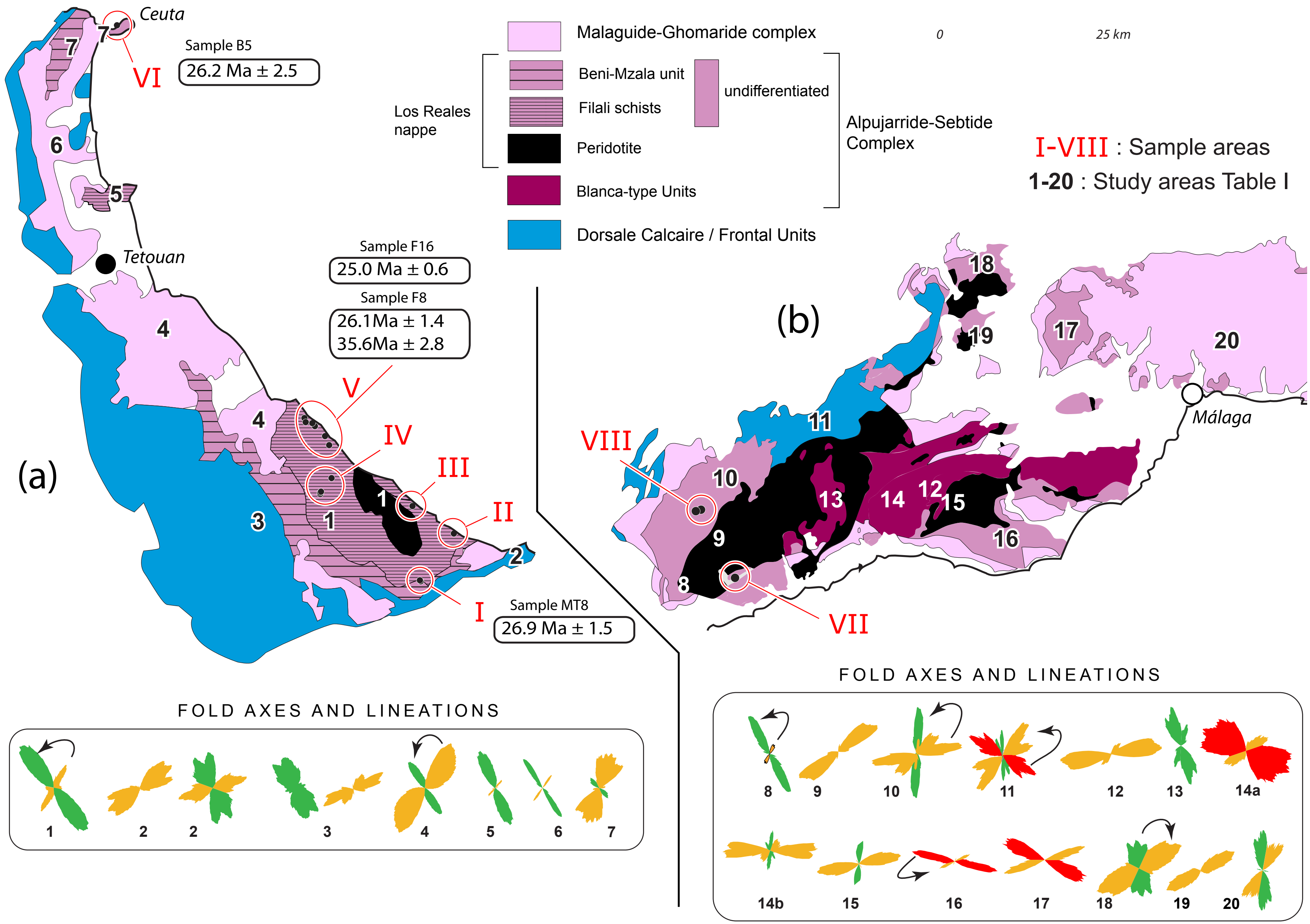

Ceuta
Sample B5
26.2 Ma ± 2.5
VI
Tetouan
Sample F16
25.0 Ma ± 0.6
Sample F8
26.1Ma ± 1.4
35.6Ma ± 2.8
V
IV
III
II
I
Sample MT8
26.9 Ma ± 1.5
(a)
Malaguide-Ghomaride complex
Beni-Mzala unit
Filali schists
undifferentiated
Los Reales nappe
Peridotite
Blanca-type Units
Alpujarride-Sebtide Complex
Dorsale Calcaire / Frontal Units
0
25 km
I-VIII : Sample areas
1-20 : Study areas Table I
(b)
Málaga
VIII
VII
FOLD AXES AND LINEATIONS
FOLD AXES AND LINEATIONS

FIGURE 2

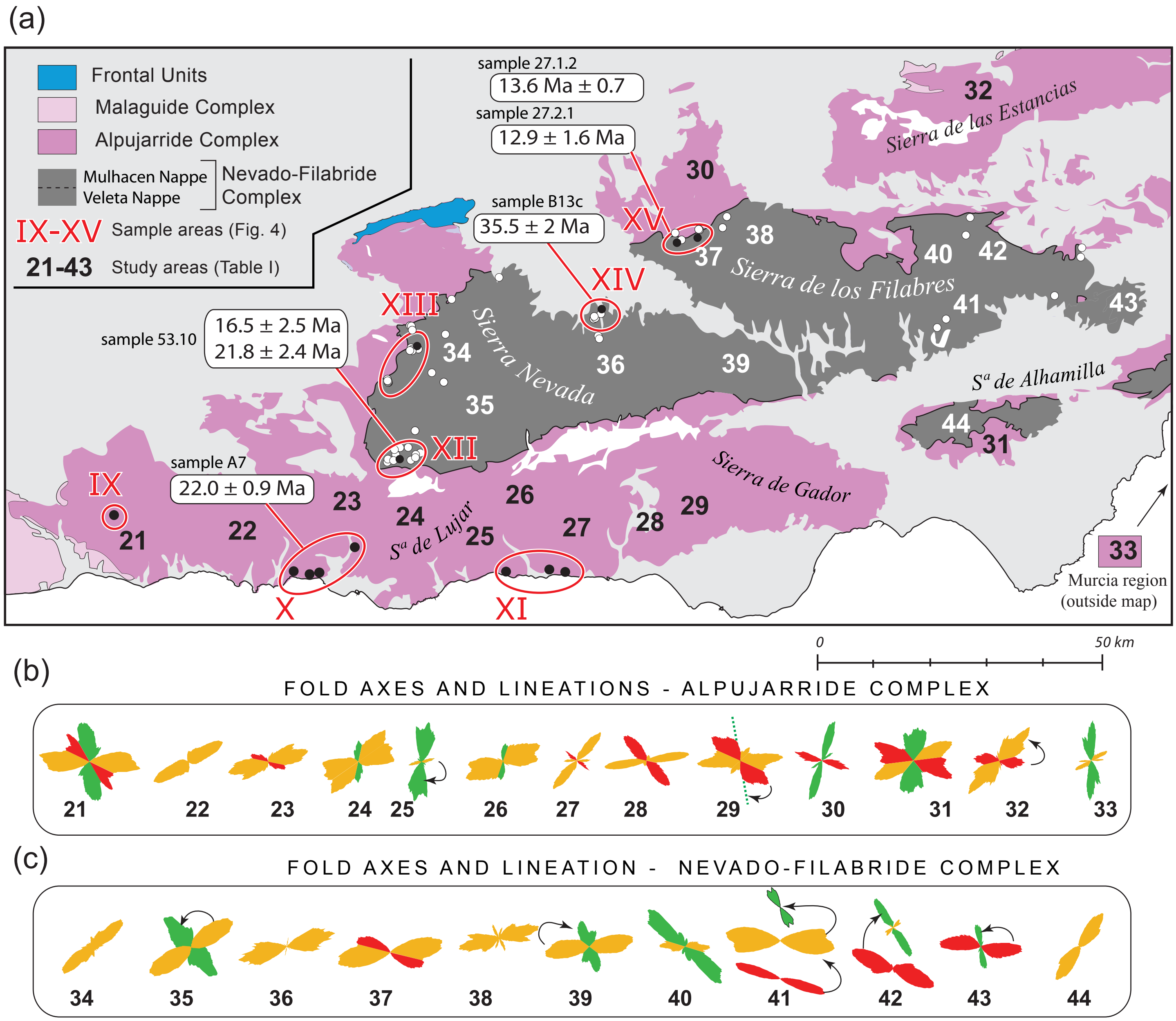

(a)
Frontal Units
Malaguide Complex
Alpujarride Complex
Mulhacen Nappe
Veleta Nappe
Nevado-Filabride Complex
IX-XV Sample areas (Fig. 4)
21-43 Study areas (Table I)
sample 27.1.2
13.6 Ma ± 0.7
sample 27.2.1
12.9 ± 1.6 Ma
sample B13c
35.5 ± 2 Ma
sample 53.10
16.5 ± 2.5 Ma
21.8 ± 2.4 Ma
sample A7
22.0 ± 0.9 Ma
Sierra de las Estancias
Sierra de los Filabres
Sierra Nevada
Sa de Alhamilla
Sierra de Gador
Sa de Lujar
Murcia region (outside map)
0
50 km
(b)
FOLD AXES AND LINEATIONS - ALPUJARRIDE COMPLEX
(c)
FOLD AXES AND LINEATION - NEVADO-FILABRIDE COMPLEX

Fig. 3

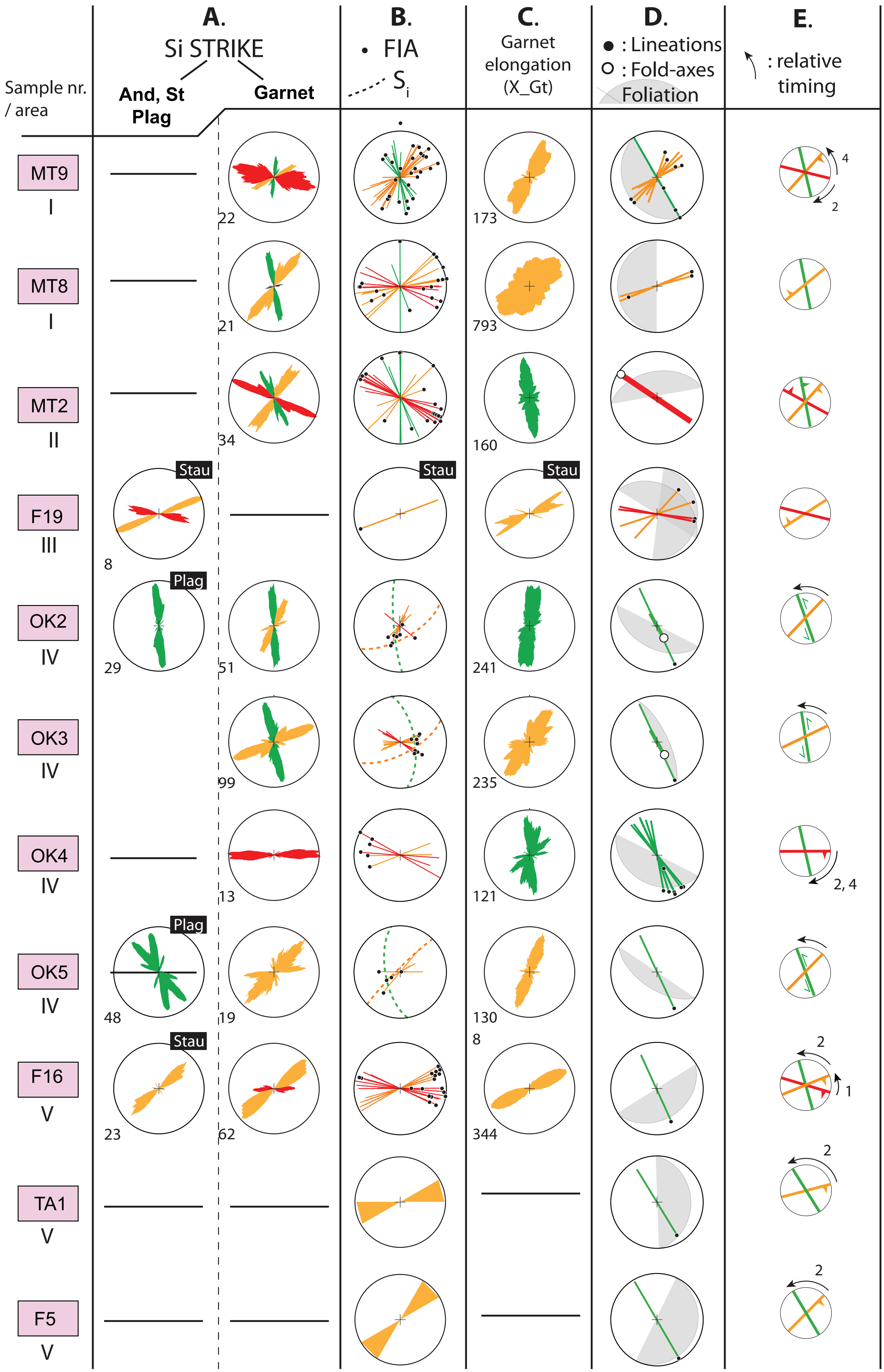
A.
Si STRIKE
And, St
Plag
Garnet
B.
FIA
S_i
C.
Garnet
elongation
(X_Gt)
D.
: Lineations
: Fold-axes
Foliation
E.
: relative
timing
Sample nr.
/ area
MT9
I
MT8
I
MT2
II
F19
III
OK2
IV
OK3
IV
OK4
IV
OK5
IV
F16
V
TA1
V
F5
V
Stau
Plag
22
21
34
8
29
51
99
13
48
19
23
62
173
793
160
241
235
121
130
8
344
4
2
2, 4
1

Fig. 4

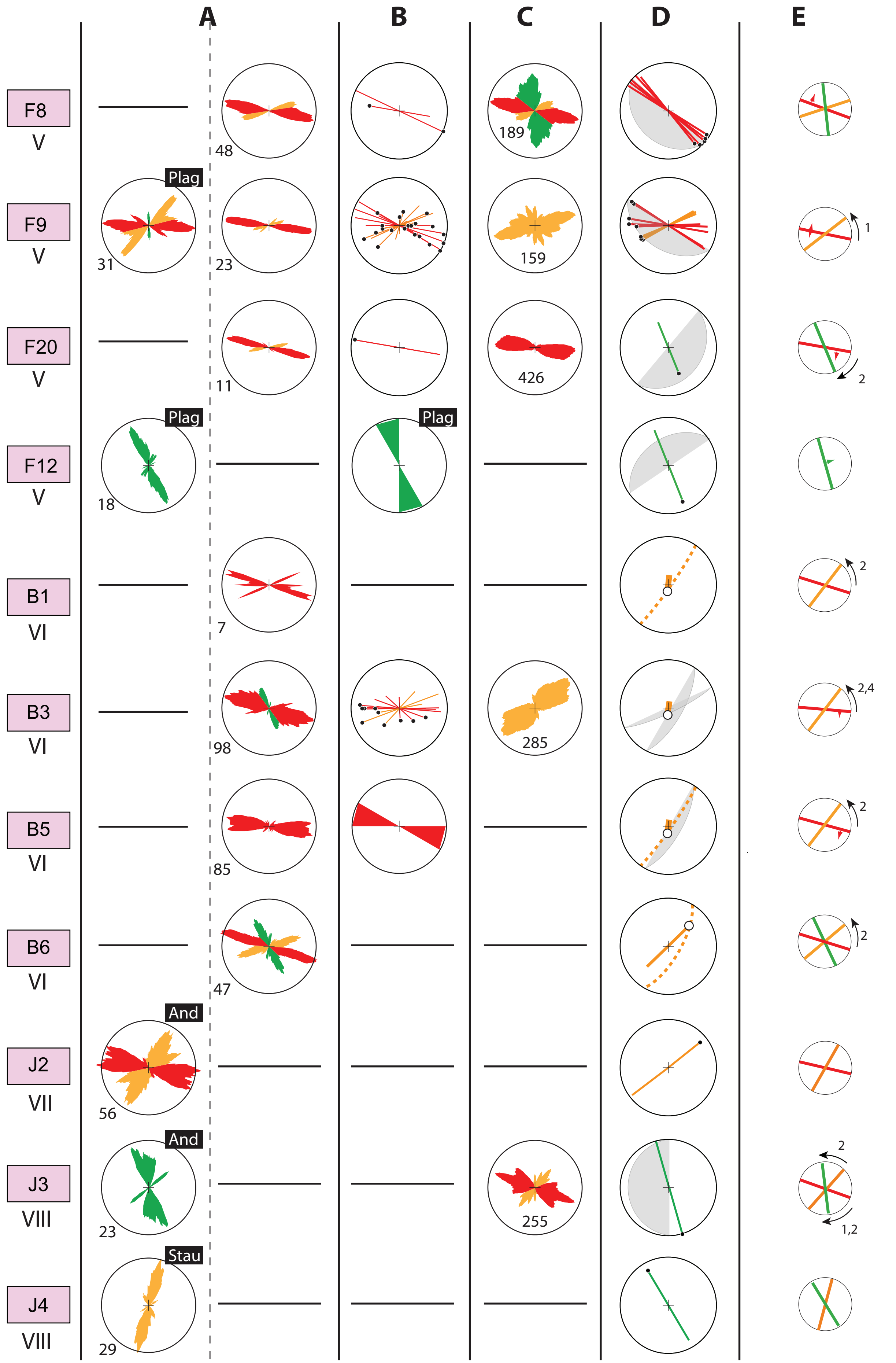

Fig. 4 continued

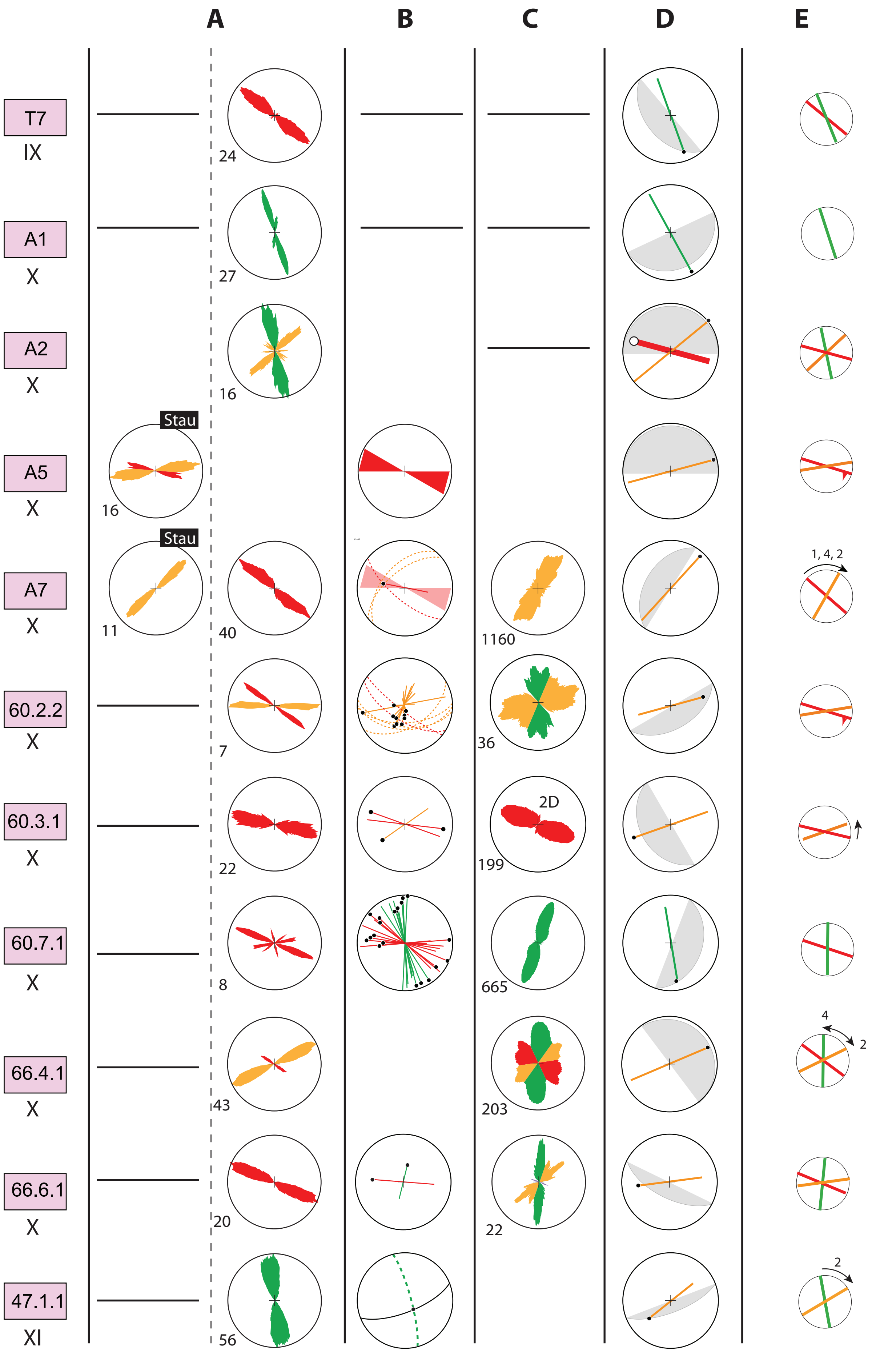

Fig. 4 continued

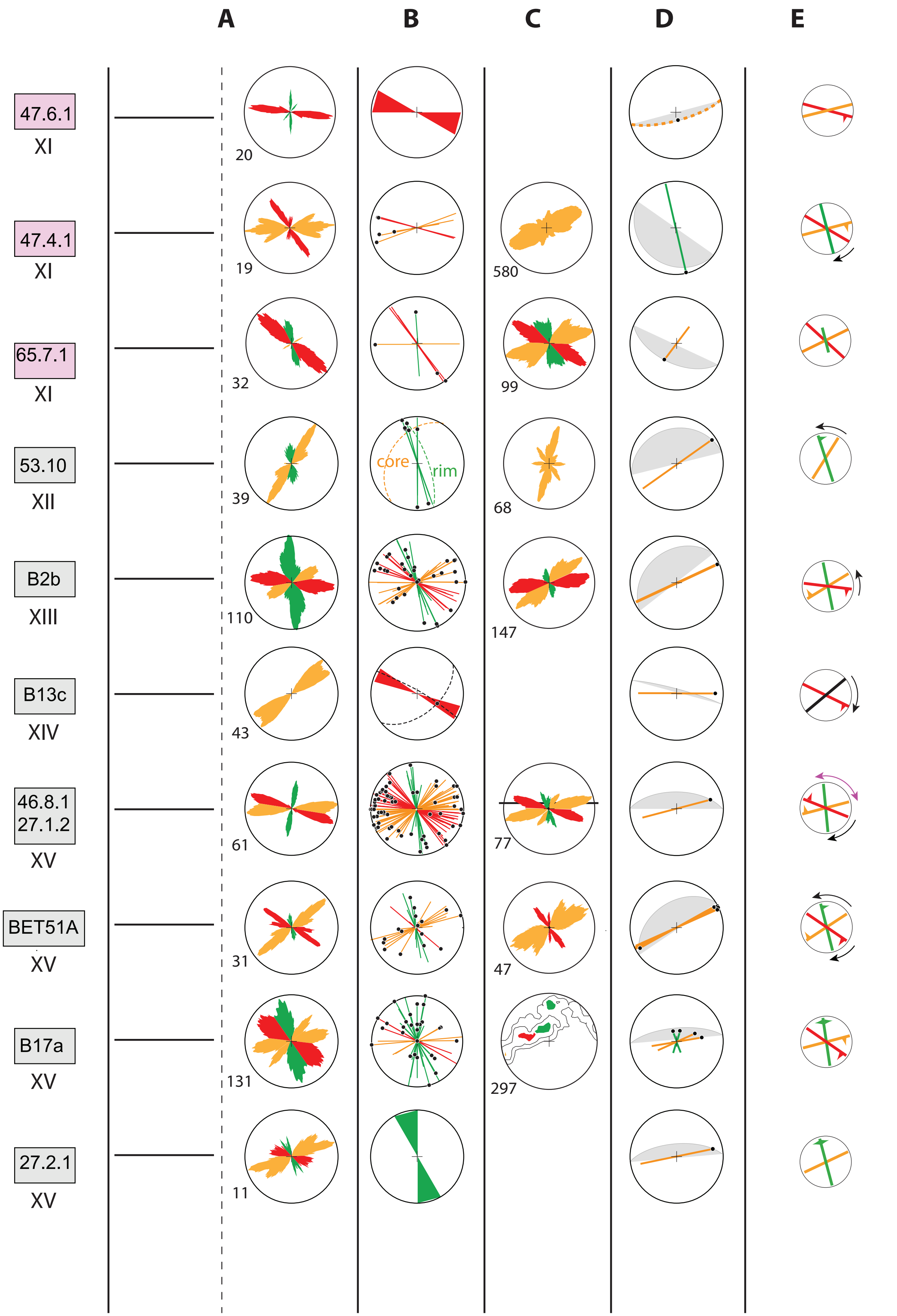

Fig. 4 continued

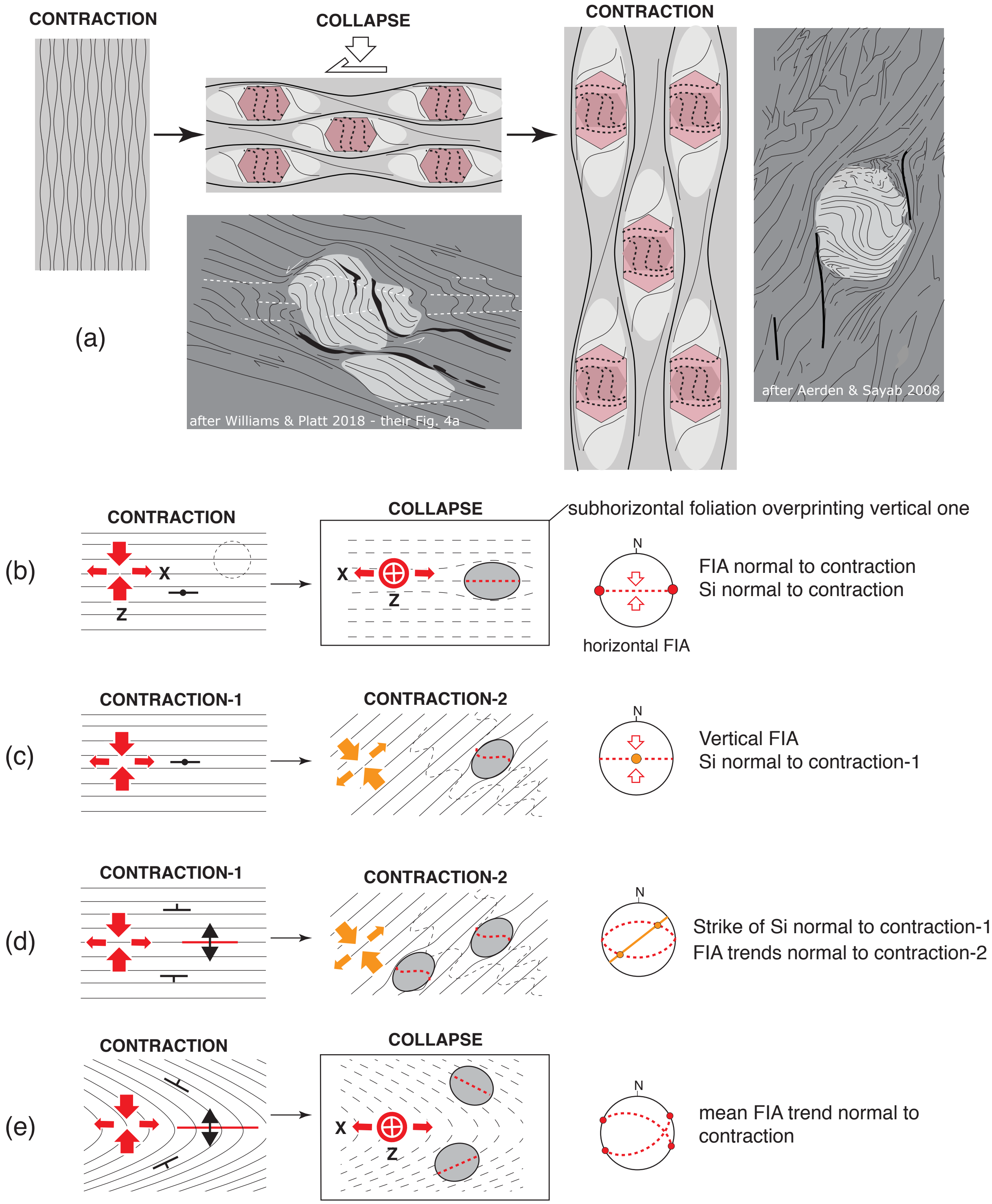
CONTRACTION
COLLAPSE
CONTRACTION
(a)
after Williams & Platt 2018 - their Fig. 4a
after Aerden & Sayab 2008
CONTRACTION
COLLAPSE
subhorizontal foliation overprinting vertical one
(b)
X
Z
N
FIA normal to contraction
Si normal to contraction
horizontal FIA
CONTRACTION-1
CONTRACTION-2
(c)
Vertical FIA
Si normal to contraction-1
CONTRACTION-1
CONTRACTION-2
(d)
Strike of Si normal to contraction-1
FIA trends normal to contraction-2
CONTRACTION
COLLAPSE
(e)
mean FIA trend normal to
contraction

Figure 5

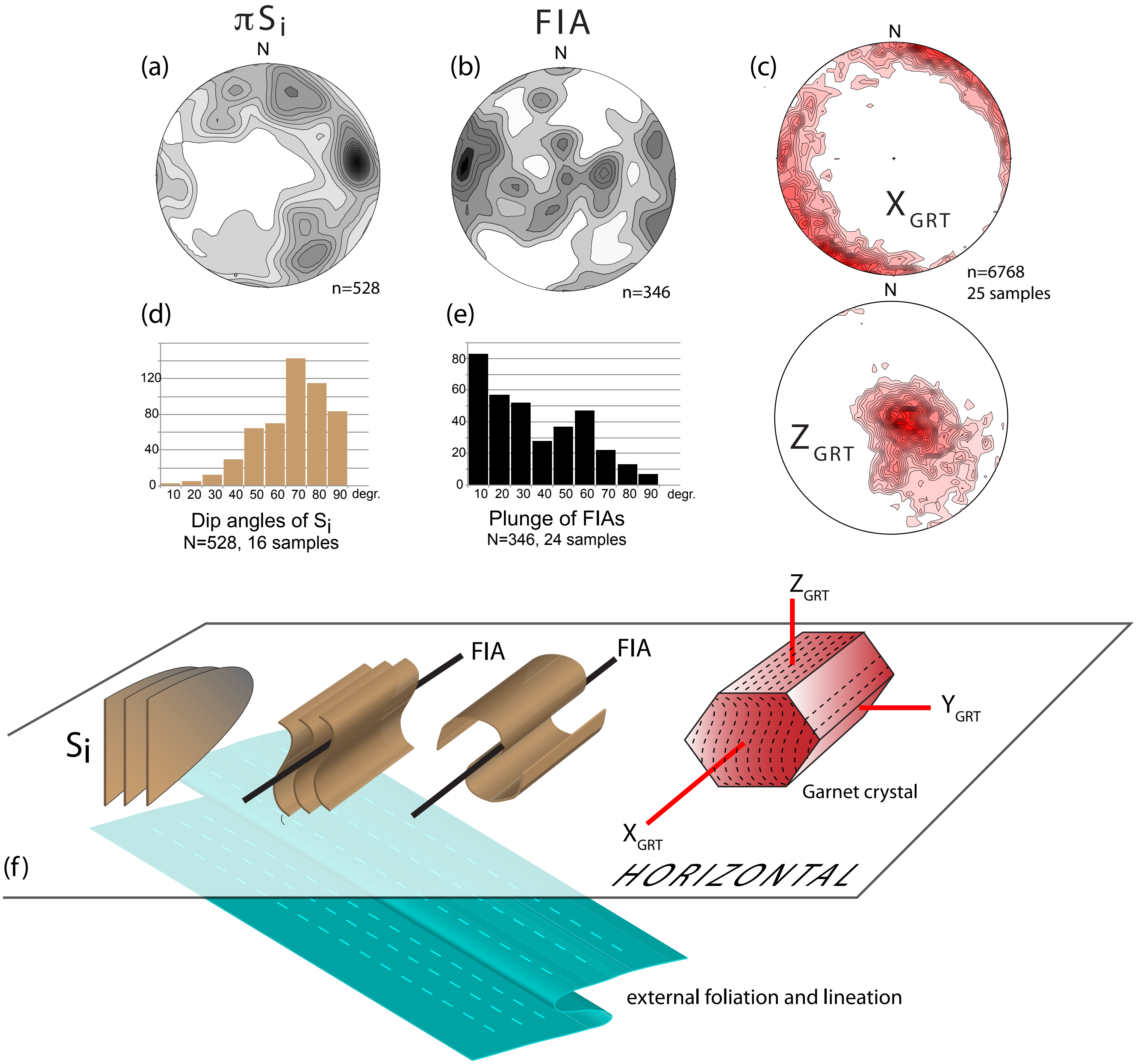

πSi
FIA
(a)
N
n=528
(b)
N
n=346
(c)
N
X GRT
n=6768
25 samples
N
Z GRT
(d)
120
80
40
0
10 20 30 40 50 60 70 80 90 degr.
Dip angles of Si
N=528, 16 samples
(e)
80
60
40
20
0
10 20 30 40 50 60 70 80 90 degr.
Plunge of FIAs
N=346, 24 samples
Z GRT
FIA
FIA
Y GRT
Si
Garnet crystal
X GRT
(f)
HORIZONTAL
external foliation and lineation

FIGURE 6

Garnet long axes (XGt)

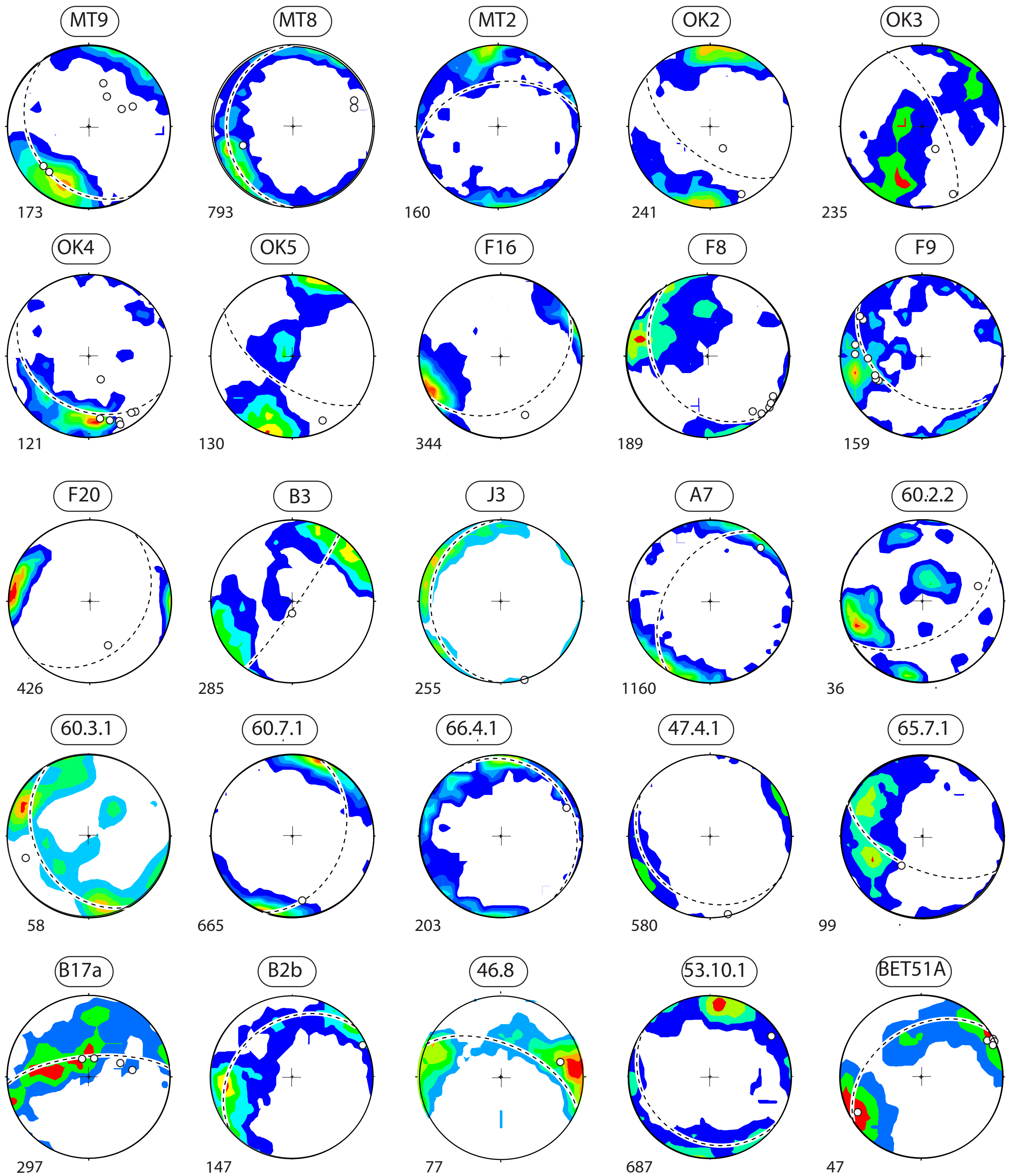

Figure 7

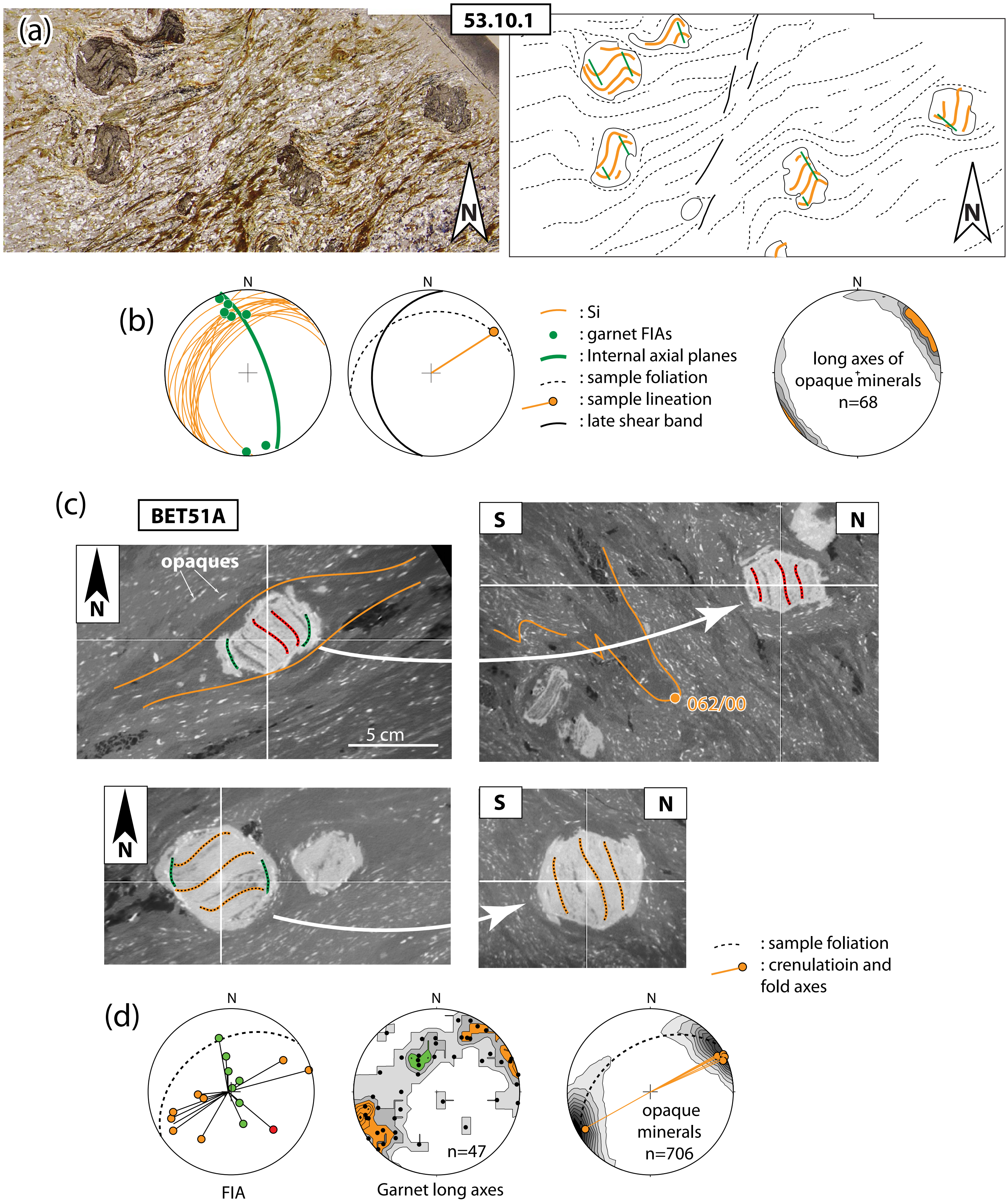

(a)
53.10.1
N
N
(b)
N
N
: Si
: garnet FIAs
: Internal axial planes
: sample foliation
: sample lineation
: late shear band
N
long axes of
opaque minerals
n=68
(c)
BET51A
N
opaques
5 cm
S
N
062/00
N
S
N
: sample foliation
: crenulatioin and
fold axes
(d)
N
N
N
n=47
opaque
minerals
n=706
FIA
Garnet long axes

Figure 8

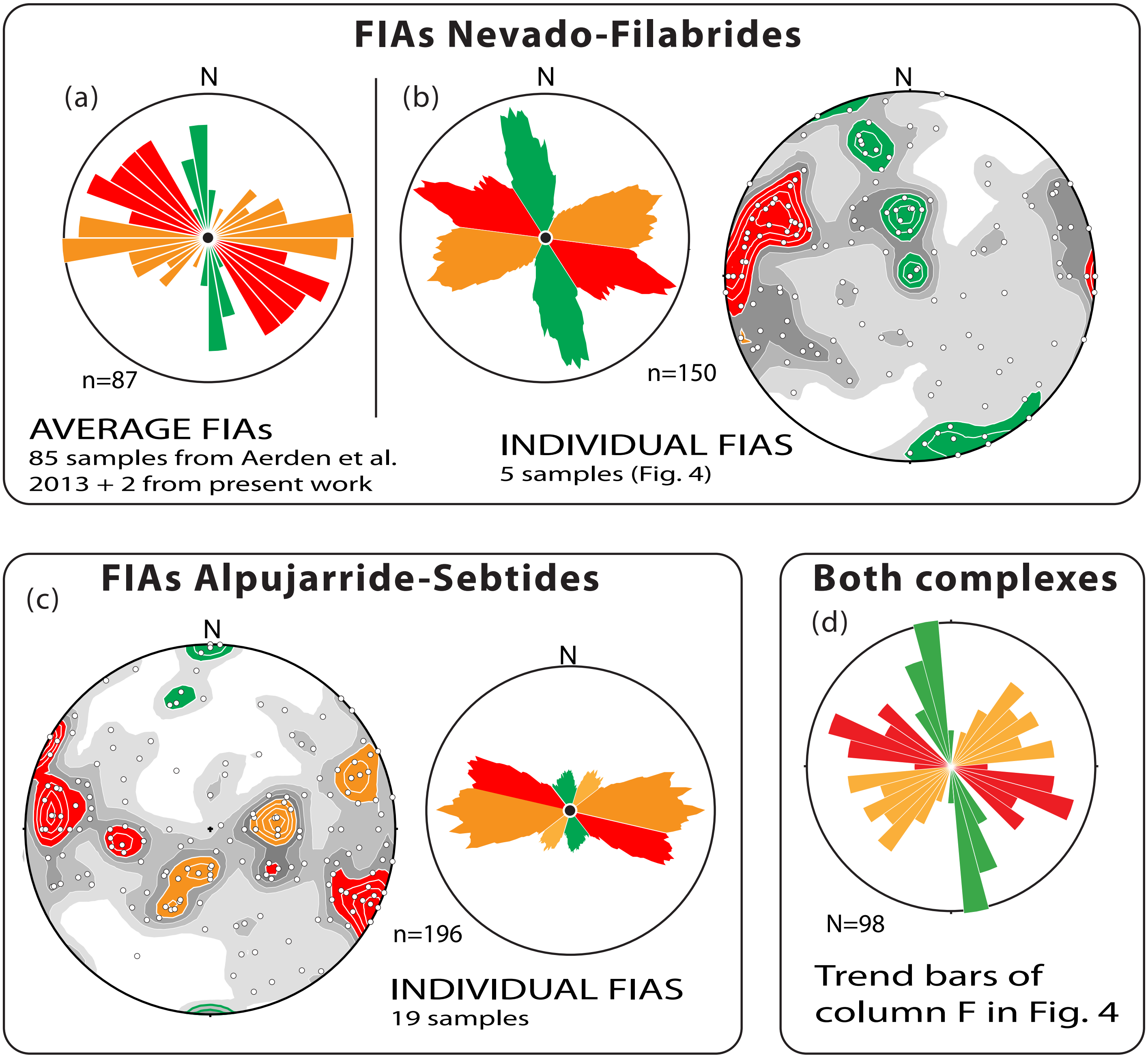

FIAs Nevado-Filabrides
(a)
N
n=87
AVERAGE FIAs
85 samples from Aerden et al.
2013 + 2 from present work
(b)
N
n=150
N
INDIVIDUAL FIAS
5 samples (Fig. 4)
FIAs Alpujarride-Sebtides
(c)
N
N
n=196
INDIVIDUAL FIAS
19 samples
Both complexes
(d)
N=98
Trend bars of
column F in Fig. 4

FIGURE 9

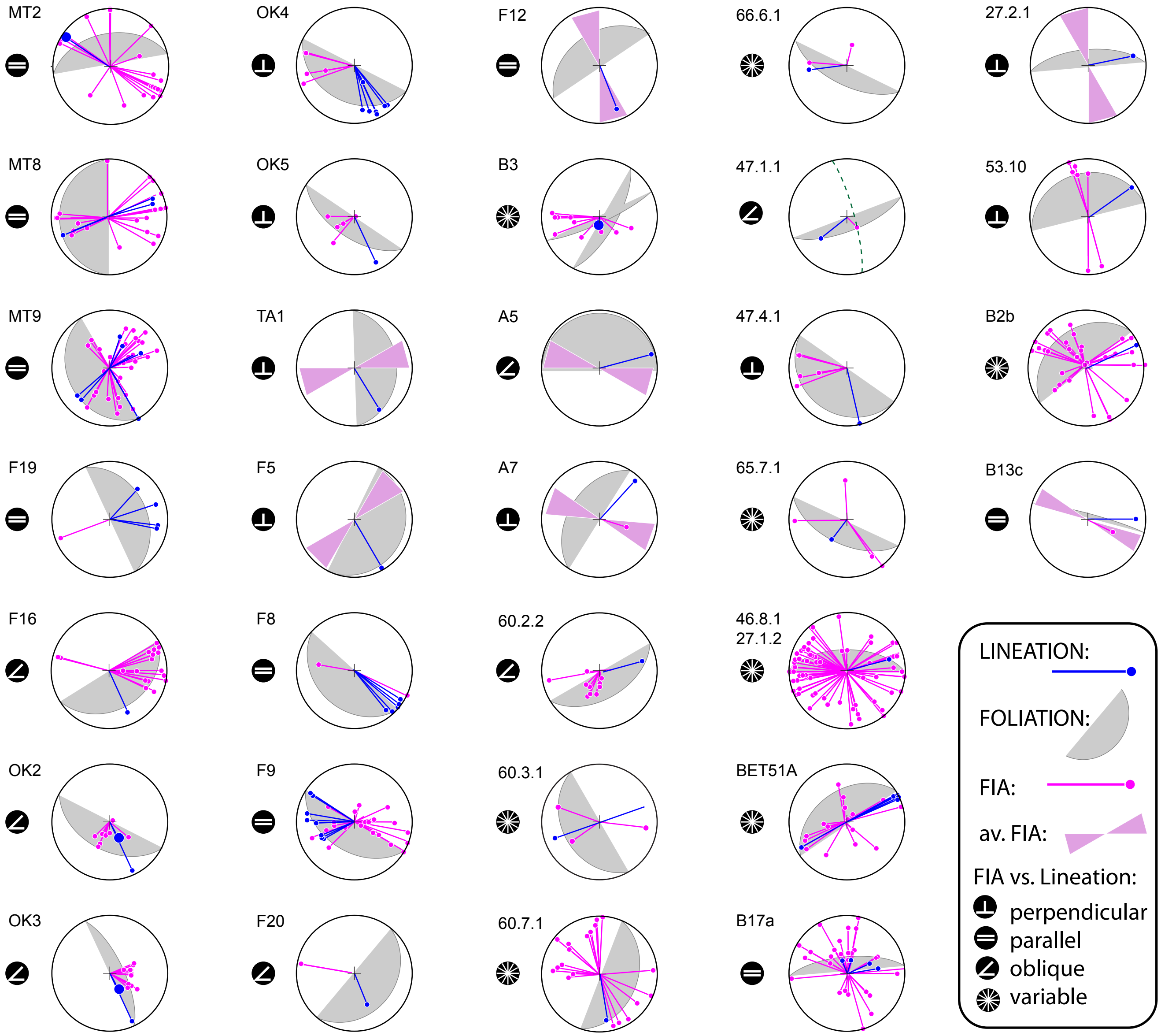
MT2
OK4
F12
66.6.1
27.2.1
MT8
OK5
B3
47.1.1
53.10
MT9
TA1
A5
47.4.1
B2b
F19
F5
A7
65.7.1
B13c
F16
F8
60.2.2
46.8.1
27.1.2
OK2
F9
60.3.1
BET51A
OK3
F20
60.7.1
B17a
LINEATION:
FOLIATION:
FIA:
av. FIA:
FIA vs. Lineation:
perpendicular
parallel
oblique
variable

FIGURE 10

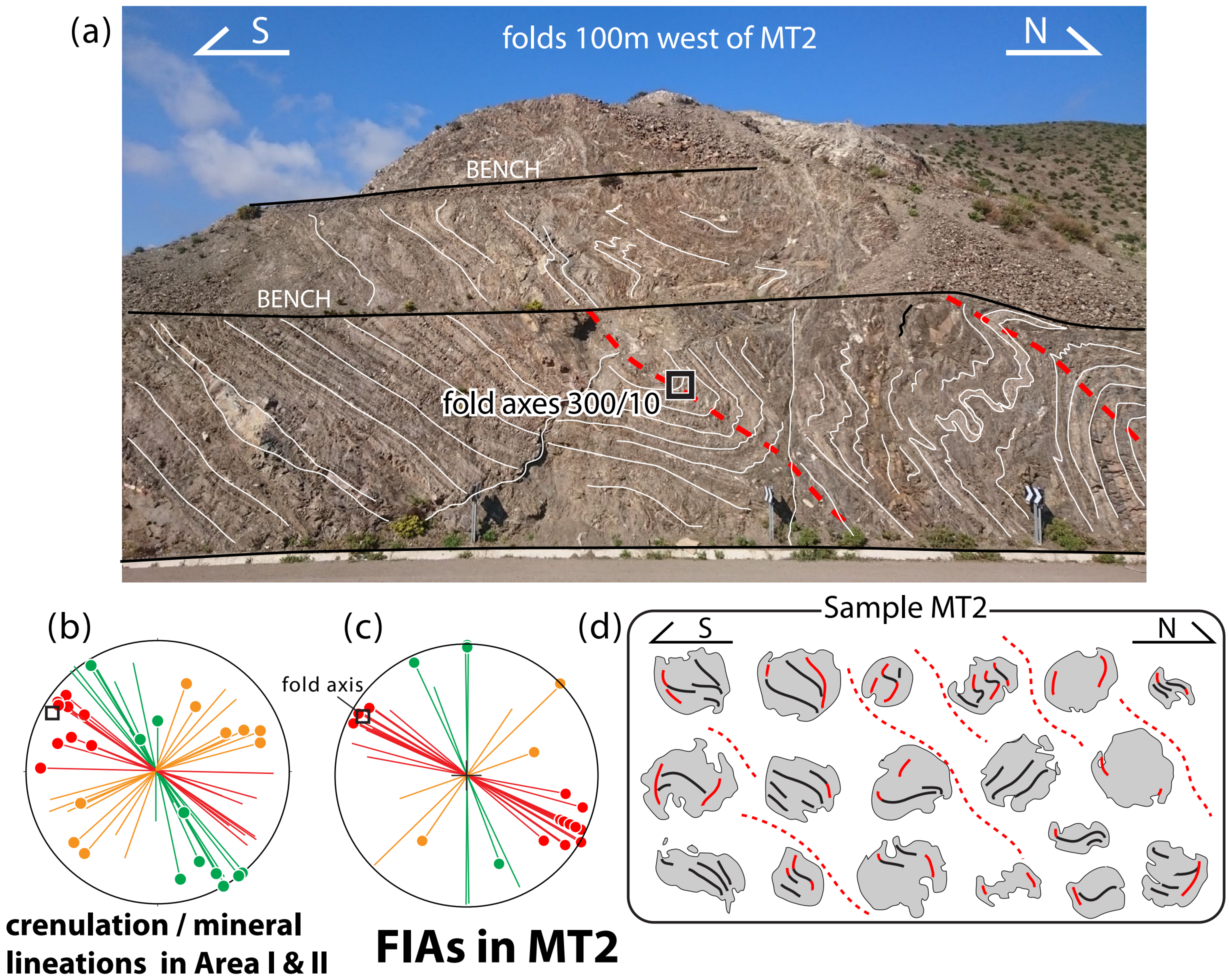

(a)
S
folds 100m west of MT2
N
BENCH
BENCH
fold axes 300/10
(b)
crenulation / mineral
lineations in Area I & II
(c)
fold axis
FIAs in MT2
(d)
Sample MT2
S
N

Fig. 11

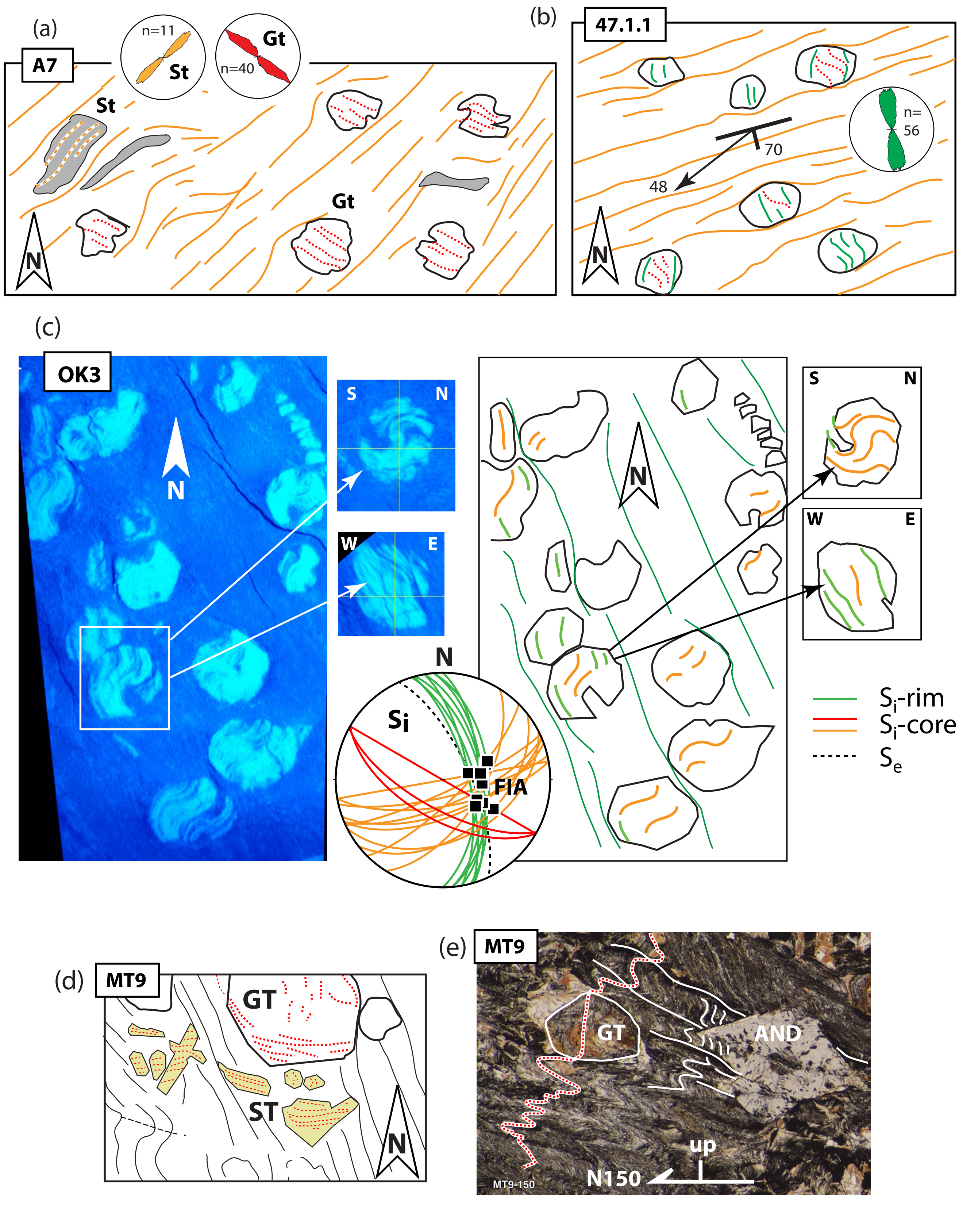

(a)
A7
n=11
St
Gt
n=40
St
Gt
N
(b)
47.1.1
70
48
n=
56
N
(c)
OK3
N
S
N
W
E
N
Si
FIA
N
S
N
W
E
Si-rim
Si-core
Se
(d)
MT9
GT
ST
N
(e)
MT9
GT
AND
up
N150
MT9-150

Figure 12

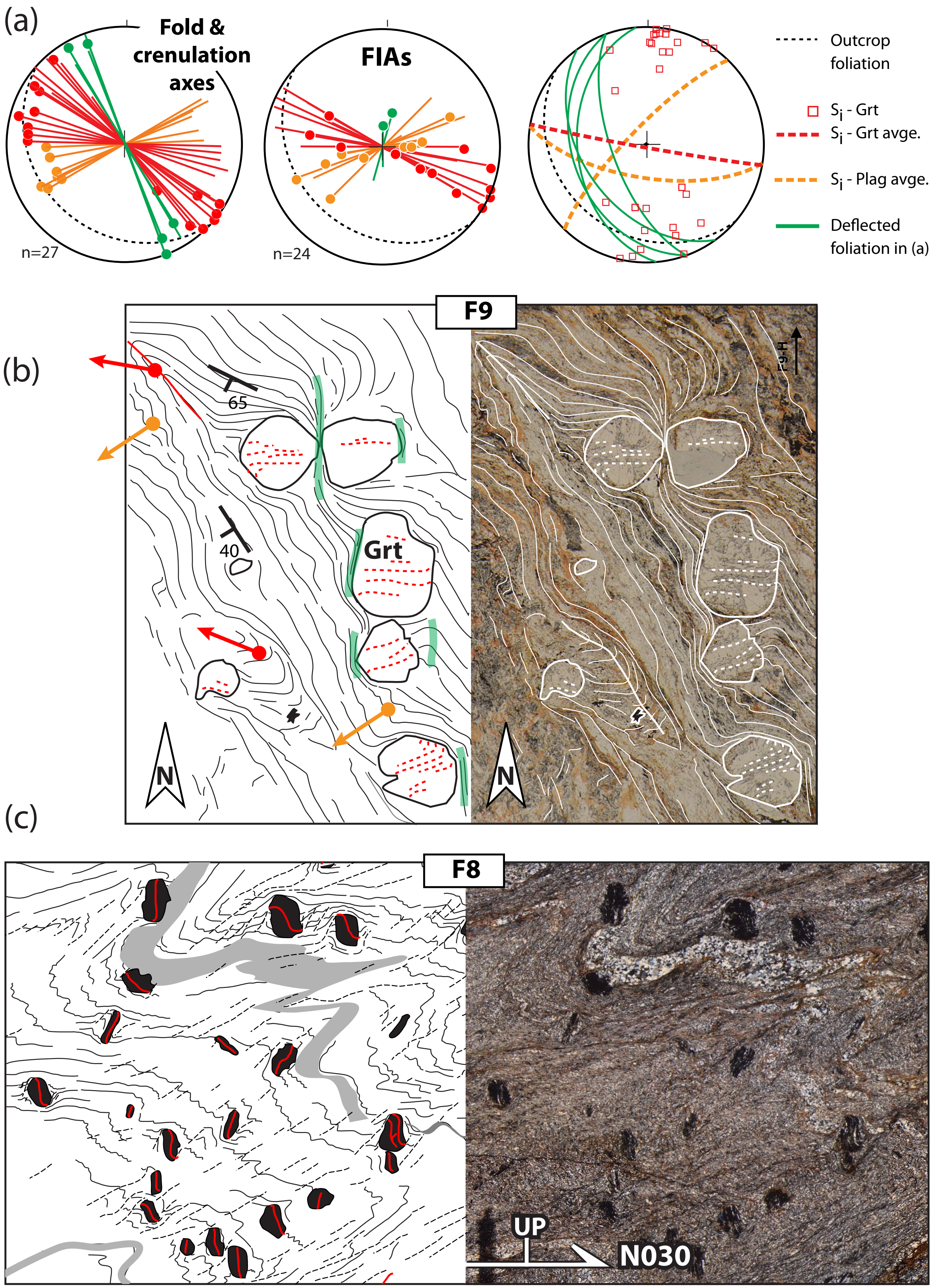

(a)
Fold & crenulation axes
n=27
FIAs
n=24
Outcrop foliation
S_i - Grt
S_i - Grt avge.
S_i - Plag avge.
Deflected foliation in (a)
(b)
F9
65
40
Grt
N
F9-H
(c)
F8
UP
N030

Figure 13

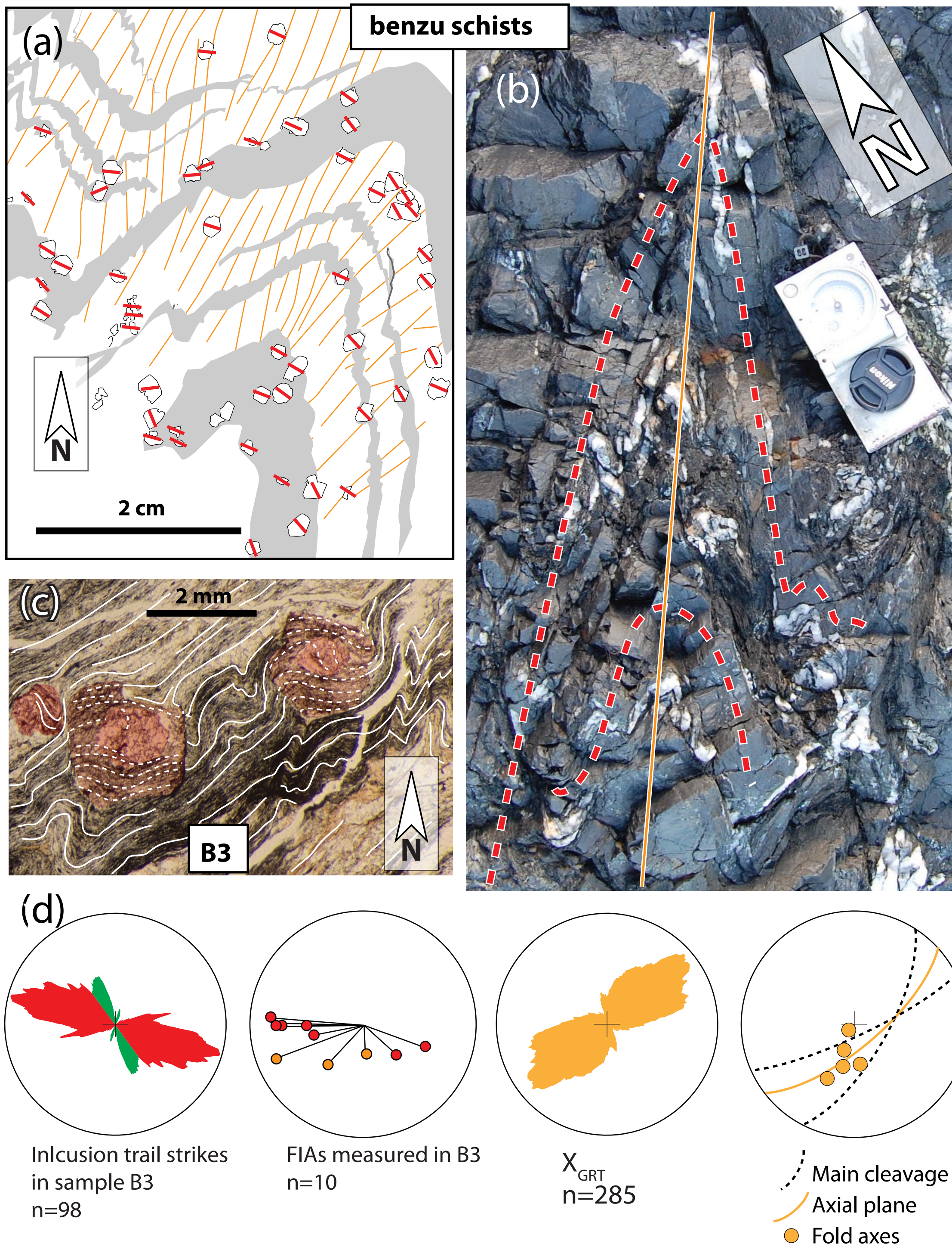

benzu schists
(a)
N
2 cm
(b)
N
(c)
2 mm
B3
N
(d)
Inlcusion trail strikes
in sample B3
n=98
FIAs measured in B3
n=10
X GRT
n=285
Main cleavage
Axial plane
Fold axes

Fig. 14

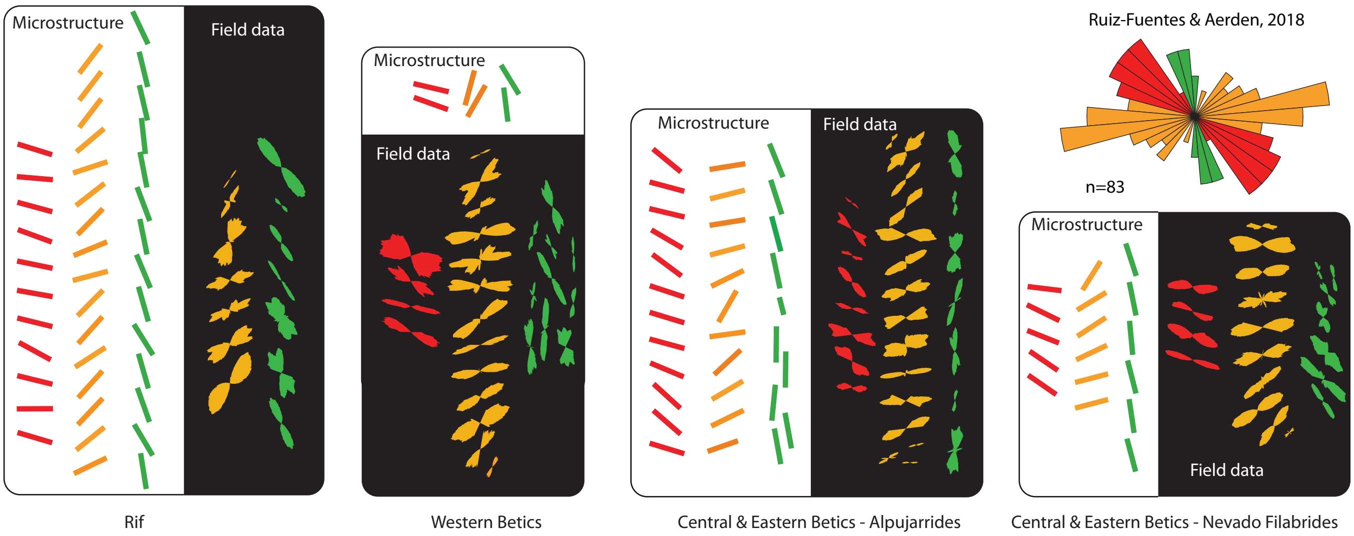
Microstructure
Field data
Microstructure
Field data
Microstructure
Field data
Ruiz-Fuentes & Aerden, 2018
n=83
Microstructure
Field data
Rif
Western Betics
Central & Eastern Betics - Alpujarrides
Central & Eastern Betics - Nevado Filabrides

Figure 15

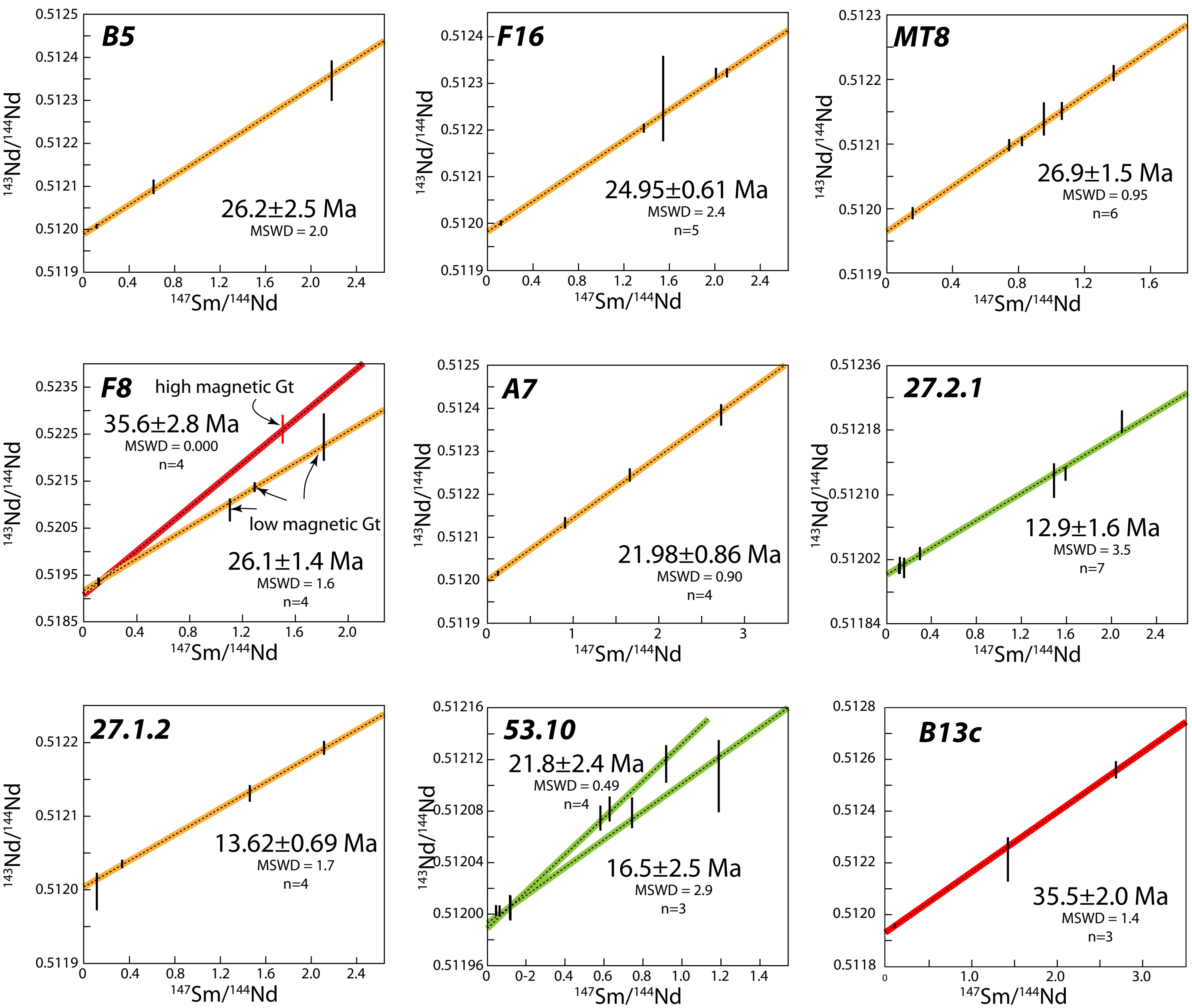

B5
26.2±2.5 Ma
MSWD = 2.0
F16
24.95±0.61 Ma
MSWD = 2.4
n=5
MT8
26.9±1.5 Ma
MSWD = 0.95
n=6
F8
high magnetic Gt
35.6±2.8 Ma
MSWD = 0.000
n=4
low magnetic Gt
26.1±1.4 Ma
MSWD = 1.6
n=4
A7
21.98±0.86 Ma
MSWD = 0.90
n=4
27.2.1
12.9±1.6 Ma
MSWD = 3.5
n=7
27.1.2
13.62±0.69 Ma
MSWD = 1.7
n=4
53.10
21.8±2.4 Ma
MSWD = 0.49
n=4
16.5±2.5 Ma
MSWD = 2.9
n=3
B13c
35.5±2.0 Ma
MSWD = 1.4
n=3
143Nd/144Nd
147Sm/144Nd

Figure 16

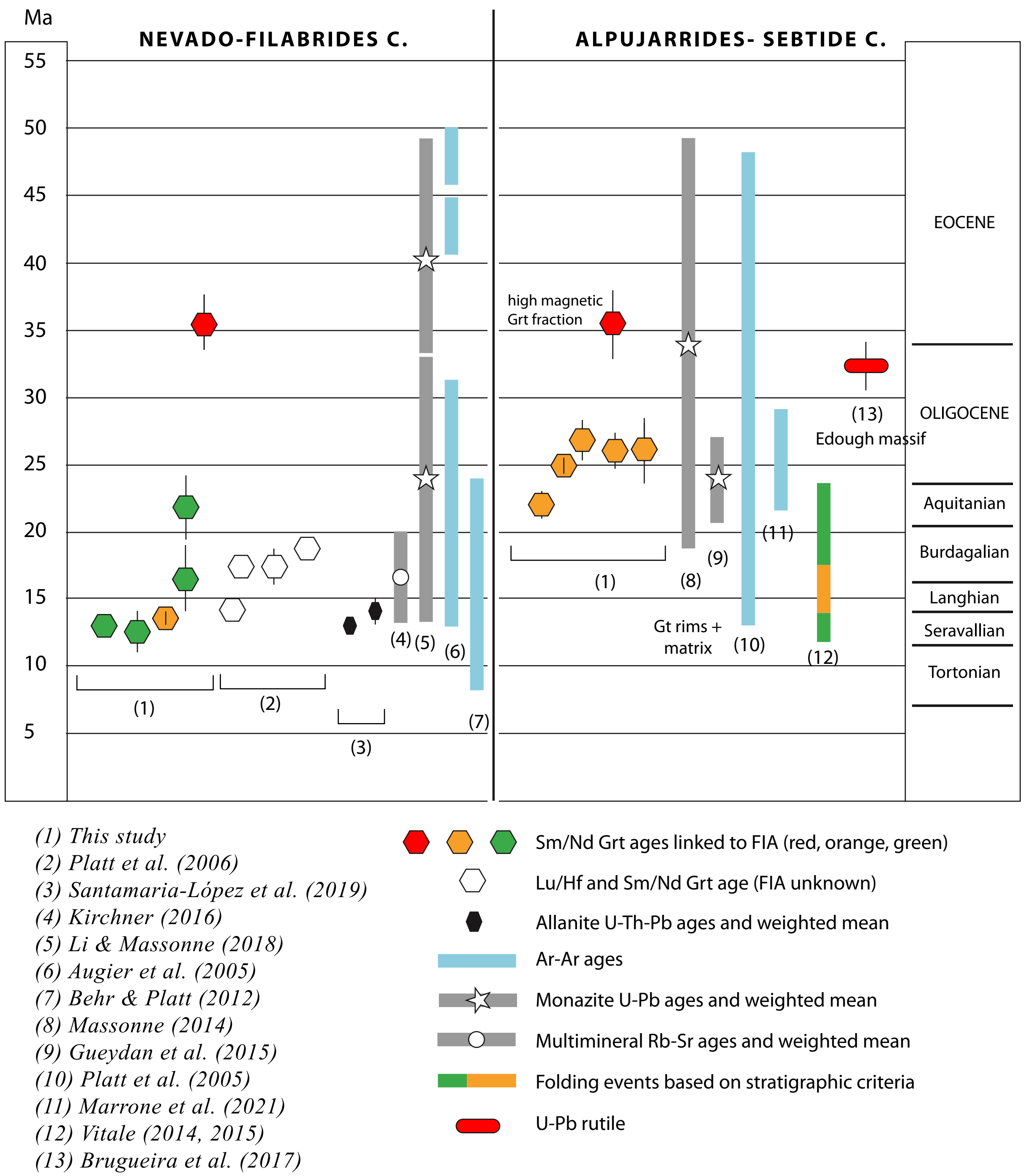

Ma
NEVADO-FILABRIDES C.
ALPUJARRIDES- SEBTIDE C.
55
50
45
40
35
30
25
20
15
10
5
EOCENE
OLIGOCENE
Aquitanian
Burdagalian
Langhian
Seravallian
Tortonian
high magnetic Grt fraction
Gt rims + matrix
Edough massif
(1)
(2)
(3)
(4)
(5)
(6)
(7)
(8)
(9)
(10)
(11)
(12)
(13)
(1) This study
(2) Platt et al. (2006)
(3) Santamaria-López et al. (2019)
(4) Kirchner (2016)
(5) Li & Massonne (2018)
(6) Augier et al. (2005)
(7) Behr & Platt (2012)
(8) Massonne (2014)
(9) Gueydan et al. (2015)
(10) Platt et al. (2005)
(11) Marrone et al. (2021)
(12) Vitale (2014, 2015)
(13) Brugueira et al. (2017)
Sm/Nd Grt ages linked to FIA (red, orange, green)
Lu/Hf and Sm/Nd Grt age (FIA unknown)
Allanite U-Th-Pb ages and weighted mean
Ar-Ar ages
Monazite U-Pb ages and weighted mean
Multimineral Rb-Sr ages and weighted mean
Folding events based on stratigraphic criteria
U-Pb rutile

Figure 17

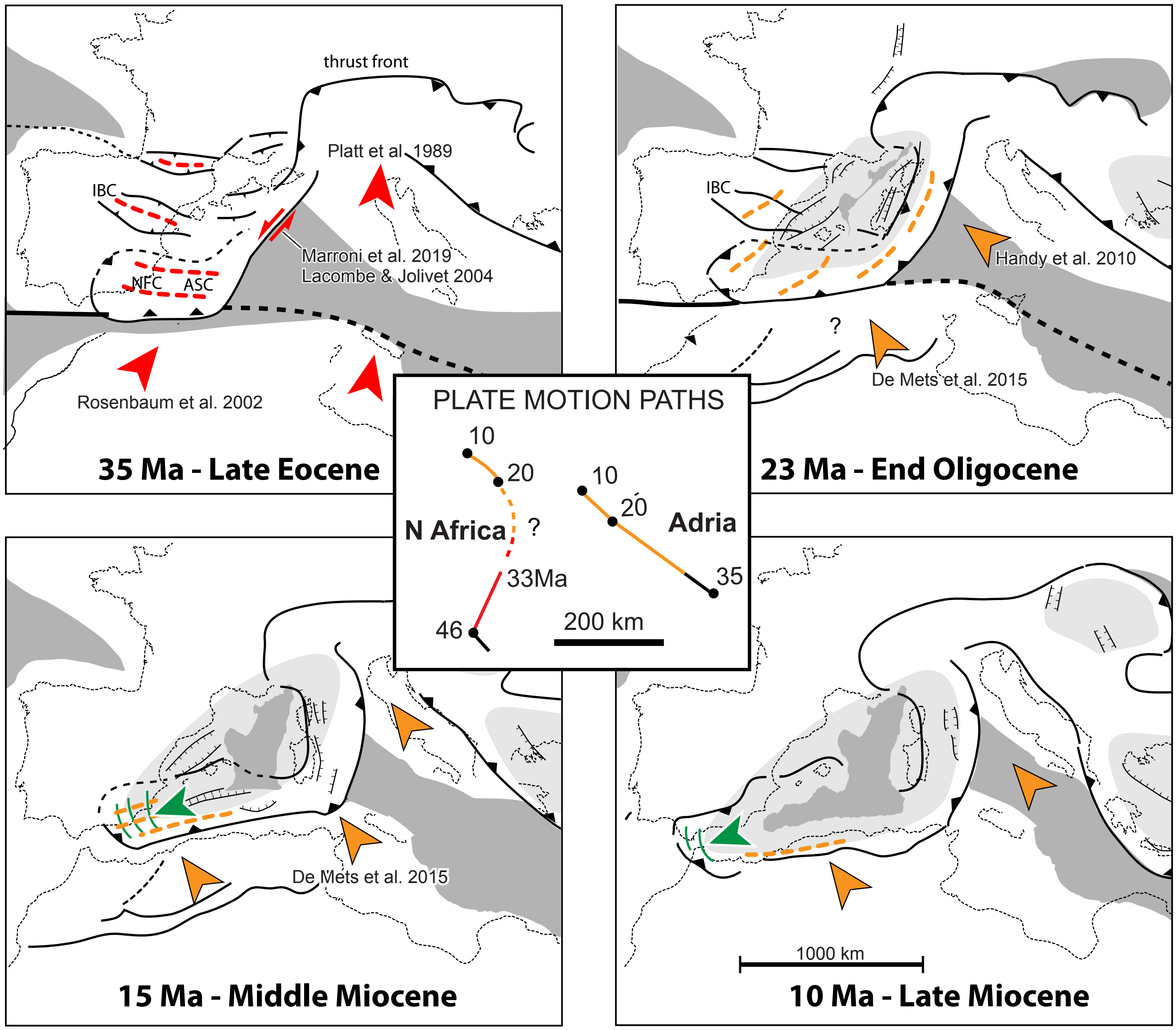

ALPUJARRIDE-SEBTIDE C.

B13c	35.5 ± 2.0 Ma
F8	35.6 ± 2.8 Ma
MT8	26.9 ± 1.5 Ma
B5	26.2 ± 2.5 Ma
F8	26.1 ± 1.4 Ma
F16	25.0 ± 0.6 Ma
A7	22.0 ± 0.9 Ma

NEVADO-FILABRIDE C.

53.10	21.8 ± 2.4 Ma
53.10	16.5 ± 2.5 Ma
27.1.2	13.6 ± 0.7 Ma
27.2.1	12.9 ± 1.6 Ma

Figure 18

Field Areas	*number of data*
1. Kornprobst (1974)	*98*
1. Afiri et al. (2011)	*106*
1. this study	*122*
2. Vitale et al. (2015)	*551*
3. Vitale et al. (2014)	*394*
4. Chalouan & Michard (1990)	*197*
5. Kornprobst (1974)	*29*
5. Romagny (2016)	*18*
5. this study (Cabo Negro)	*12*
6. Kornprobst (1974)	*31*
7. Kornprobst (1974)	*16*
7. Romagny (2016)	*11*
7. Homonnay et al. (201()	*27*
7. this study	*31*
8. Kornprobst (1971, 1974)	*51*
9. Précigout et al. (2013)	*66*
10. Balanya (1997) + Loomis 1972	*124*
11. Mazolli et al. (2013)	*92*
12. Tubía et al. (2013)	*130*
13. Tubía et al. (2013)	*41*
14a. Orozco & Alonso-Chaves (2012)	*122*
14b. Sanz de Galdeano & Andreo (1995)	*49*
15. Tubía et al. (1997)	*75*
16. Tubía et al. (1993, 1994)	*30*
17. Williams & Platt (2018 – Fig8L)	*30*
18. Argles (1999)	*1014*
19. Tubía (2004)	*67*
20. Cuevas et al. (2001)	*33*
21. Alonso-Chaves & Orozco (2012)	*468*
22. Rossetti et al. (2005)	*607*
23. Williams & Platt (2017)	*429*
24. Simancas (2018, Fig. 1d)	*521*
25. Orozco et al. (2004, Fig. 5-1)	*117*
26. Azañon et al. (1997)	*273*
27. Tubía et al. (1992, Fig. 4)	*53*
28. Orozco et al. (1998)	*153*
29. Orozco (1972)	*624*
30. Williams & Platt (2018, Fig. 8r)	*32*
31. Platt et al. (1983)/Williams & Platt (	*343*
32. Williams & Platt (2018, Fig. 8s)	*102*
33. Tubía et al. (1992, Fig. 3)	*23*
34. Ruiz-Fuentes & Aerden (2018)	*236*
35. Galindo-Zaldivar (1993)	*4203*
36. this study	*47*
37. Jabaloy (1993)	*581*
38. Aerden et al. (2013)	*123*
39. Martínez-Martínez (1986)	*705*
40. Vissers (1991)	*394*
41. De Jong (1991)	*718*
42. Langenberg (1972)	*509*
43. Soto (1991)	*407*
44. Platt & Behrman (1986)	*445*
total	15680

Table II Summary of Sm and Nd Concentrations and Isotopic Ratios

Sample name	Material	ng Nd loaded	Nd ppm	Sm ppm	$^{147}Sm/^{144}Nd$	± 2 S.E.	$^{143}Nd/^{144}Nd$	± 2 S.E.
A7	Whole rock	9.6	31.39	5.882	0.113362	0.000010	0.5120169	0.0000026
	Garnet powder	2.5	0.510	2.297	2.72516	0.00044	0.512414	0.000022
	Garnet powder leachate	2.6	0.819	2.251	1.66311	0.00021	0.512246	0.000013
	Garnet	5.3	1.026	3.209	1.89252	0.00073	0.512237	0.000013
	Garnet leachate	12	1.749	2.621	0.90628	0.00025	0.512141	0.000028
B5	Whole rock	63	45.13	8.636	0.115771	0.000015	0.5120061	0.0000043
	Garnet	0.7	0.215	0.771	2.17416	0.00049	0.512344	0.000039
	Garnet powder	1.9	0.731	0.741	0.612982	0.000064	0.512100	0.000014
B13c	Whole rock	67	27.40	5.350	0.117679	0.000036	0.5119587	0.0000086
	Garnet	1.9	0.120	0.520	2.68096	0.00062	0.512558	0.000035
	Garnet	3.1	0.170	0.390	1.42211	0.00060	0.512212	0.000086
F8	Whole rock	50	35.59	6.800	0.116307	0.000014	0.5119347	0.0000053
	Garnet	1.3	0.151	0.377	1.5128	0.0049	0.512260	0.000025
	Garnet	0.4	0.132	0.398	1.82300	0.00019	0.512243	0.000042
	Garnet	3.5	0.199	0.427	1.29620	0.00022	0.512137	0.000009
	Garnet leachate	0.8	0.197	0.362	1.11068	0.00019	0.512088	0.000021
F16	Whole rock	9.6	37.40	7.387	0.119471	0.000013	0.5120028	0.0000054
	Garnet	0.8	1.103	2.812	1.54368	0.00078	0.512269	0.000071
	Garnet leachate	2.1	0.529	1.752	2.00517	0.00023	0.512322	0.000011
	Garnet powder	2.7	0.590	2.049	2.1019	0.0030	0.5123224	0.0000079
	Garnet powder leachate	5.2	0.893	2.035	1.37893	0.00017	0.512204	0.000010
MT8	whole rock	16	3.123	0.802	0.155420	0.000018	0.5119930	0.0000047
	Garnet powder	2.0	0.177	0.402	1.37712	0.00024	0.512210	0.000010
	Garnet	1.8	0.341	0.539	0.95548	0.00015	0.512139	0.000021
	Garnet	11	0.439	0.770	1.06126	0.00051	0.512151	0.000012
	Garnet powder	8.3	0.526	0.713	0.82038	0.00028	0.512104	0.000006
	Garnet leachate	5.6	0.799	0.984	0.74450	0.00013	0.5120981	0.0000078
27.1.2	Whole rock	10	34.17	6.570	0.116316	0.000088	0.511997	0.000021
	Garnet	6.7	1.267	4.430	2.11480	0.00056	0.5121930	0.0000066
	Garnet	11	1.089	2.631	1.4616	0.0018	0.512131	0.000009
	Garnet powder	2.2	0.419	0.232	0.335620	0.000049	0.512035	0.000005
27.2.1	whole rock	61	42.09	8.197	0.117807	0.000015	0.5120168	0.0000032
	whole rock	59	45.47	8.828	0.117443	0.000017	0.5120086	0.0000044
	Garnet	6.5	1.032	2.559	1.49932	0.00053	0.512118	0.000017
	Garnet	6.3	0.854	2.261	1.60073	0.00070	0.512127	0.000008
	Garnet leachate	2.5	0.462	1.599	2.10295	0.00033	0.512191	0.000012
	Garnet powder	37	5.758	2.854	0.299869	0.000065	0.512027	0.000007
	Garnet leachate	166	21.64	5.595	0.15639	0.00010	0.512009	0.000011
53.10.1	Whole rock	57	41.02	8.152	0.120213	0.000014	0.5120053	0.0000078
	Garnet	10	1.220	1.181	0.58554	0.00014	0.5120741	0.0000059
	Garnet	11	1.109	1.160	0.632932	0.000059	0.5120807	0.0000052
	Garnet	5.1	1.256	1.550	0.74641	0.00014	0.512079	0.000010
	Garnet powder	2.5	0.631	1.245	1.19346	0.00043	0.512107	0.000023
	Garnet powder	2.3	0.738	1.125	0.92255	0.00014	0.512116	0.000012